

The Complete Spectral Catalog of Bright BATSE Gamma-Ray Bursts

Yuki Kaneko¹, Robert D. Preece², Michael S. Briggs², William S. Paciesas²,
Charles A. Meegan³, David L. Band⁴

ABSTRACT

We present a systematic spectral analysis of 350 bright Gamma-Ray Bursts (GRBs) observed with the Burst and Transient Source Experiment (BATSE; ~ 30 keV – 2 MeV) with high temporal and spectral resolution. Our sample was selected from the complete set of 2704 BATSE GRBs based on their energy fluence or peak photon flux values to assure good statistics, and included 17 short GRBs. To obtain well-constrained spectral parameters, several photon models were used to fit each spectrum. We compared spectral parameters resulting from the fits using different models, and the spectral parameters that best represent each spectrum were statistically determined, taking into account the parameterization differences among the models. A thorough analysis was performed on 350 time-integrated and 8459 time-resolved burst spectra, and the effects of integration times in determining the spectral parameters were explored. Using the results, we studied correlations among spectral parameters and their evolution pattern within each burst. The resulting spectral catalog is the most comprehensive study of spectral properties of GRB prompt emission to date, and is available electronically from the High-Energy Astrophysics Science Archive Research Center (HEASARC). The catalog provides reliable constraints on particle acceleration and emission mechanisms in GRBs.

Subject headings: Catalog – gamma-rays: bursts

¹Universities Space Research Association, NSSTC, XD-12, 320 Sparkman Drive, Huntsville, AL 35805, Yuki.Kaneko@nsstc.nasa.gov

²Department of Physics, University of Alabama in Huntsville, NSSTC, XD-12, 320 Sparkman Drive, Huntsville, AL 35805, Rob.Preece@nsstc.nasa.gov, Michael.Briggs@nsstc.nasa.gov, Bill.Paciesas@nsstc.nasa.gov

³NASA/Marshall Space Flight Center, NSSTC, XD-12, 320 Sparkman Drive, Huntsville, AL 35805, Chip.Meegan@nasa.gov

⁴NASA/Goddard Space Flight Center, Greenbelt, MD 20771 & JCA/University of Maryland, Baltimore County, Baltimore, MD 21250, dband@milkyway.gsfc.nasa.gov

1. Introduction

In recent years, multi-wavelength observations of afterglow emission of Gamma-Ray Bursts (GRBs) have provided great advancement in our knowledge of GRB progenitor, afterglow emission mechanism, and their environment. Nonetheless, the physical mechanism that creates the prompt gamma-ray emission with extremely short variability is still not resolved, thus understanding GRB prompt emission spectra remains crucial to revealing their true nature. GRB spectral analysis attempts to empirically characterize the spectra, which are generally well described, in the energy range of ~ 10 keV to a few MeV, by two power laws joined smoothly at certain energies (Band et al. 1993). The spectral parameters (the power-law indices and the peak energy in the power density spectrum) are then used to infer the GRB emission and particle acceleration mechanisms.

Currently, the most favored GRB emission mechanism is the simple emission scenario of optically-thin synchrotron radiation by shock-accelerated electrons (“synchrotron shock model”; Tavani 1996). This simple theoretical model, however, has previously been challenged by the observations in the context of GRB prompt emission (Preece et al. 1998a,b, 2000; Ghirlanda et al. 2002; Lloyd-Ronning & Petrosian 2002). While the synchrotron shock model can account for many of the observed spectra, a considerable number of spectra exhibit behavior inconsistent with this theoretical model. Meanwhile, it is also true that many observed spectra could be fitted with various photon models statistically as well as each other, due to the limited spectral resolution of available data and detector sensitivity. Since the photon models usually used in GRB spectral analysis are parameterized differently, the resulting spectral parameters are found to be highly dependent on photon model choices (Preece et al. 2002; Ghirlanda et al. 2002). Additionally, to deduce the emission mechanism from observations, spectra with fine time resolution are necessary because of the short timescales involved in typical emission processes (i.e., the radiative cooling time, dynamical time, or acceleration time). This is also indicated by the extremely short variability observed in GRB lightcurves (e.g., Bhat et al. 1992), although the detectors’ finest time resolution is still longer than the shortest physical timescales involved to produce GRBs. The integration times of spectra certainly depend on the capabilities of the detector systems as well as the brightness of events and photon flux evolution. GRB spectral analyses, therefore, have been performed on various timescales, yet a comprehensive study of the relations between time-averaged and time-resolved spectra, and the effects of various integration times on spectral properties has not been done. Thus, in order for the spectral parameters to meaningfully constrain the physical mechanisms, a comprehensive spectral study with finest possible spectral and temporal resolution, using various photon models, should be carried out with a sufficiently large database.

Among all the gamma-ray experiments that have detected GRBs, the Burst and Transient Source Experiment (BATSE; Fishman et al. 1989), aboard the *Compton Gamma-Ray Observatory* (*CGRO*; Gehrels, Chipman, & Kniffen 1994), provided the largest GRB database from a single experiment, consisting of observational data for 2704 GRBs (M.S. Briggs in preparation). For many of the BATSE GRBs, high time and energy resolution data are available. BATSE also provided wider energy coverage than current GRB missions such as *HETE-2* and *Swift*. The BATSE data, therefore, are the most suitable for detailed spectral studies of GRB prompt emission, both in quantity and quality. The previous BATSE GRB spectral catalog (Preece et al. 2000, SP1 hereafter) consisted of 5500 time-resolved spectra from 156 bright GRBs that occurred before October 1998. The SP1 burst sample was selected from a set of 1771 GRBs (from the BATSE 4B catalog (Paciesas et al. 1999) and the “current” catalog available online¹), nearly 1000 bursts less than what is currently available in the complete database. The sample was also limited to the bursts that provided more than eight spectra and therefore, excluded relatively shorter and weaker bursts. In addition, a combination of the Large Area Detector (LAD) and Spectroscopy Detector (SD) data was used, no time-integrated spectral fit (i.e., spectrum with integration time of the burst duration) results were presented, and only one photon model was fitted to each spectrum. Finally, the mathematical differences in parameterization of each model were not taken into account to obtain corrected overall statistics of the analysis results.

We present in this paper the high-energy resolution spectral analysis of 350 bright BATSE GRBs with fine time resolution. The main objective of this work is to obtain consistent spectral properties of GRB prompt emission with sufficiently good statistics. This is done by a systematic analysis of the large sample of GRB spectra, using a set of photon models, all fitted to each spectrum. Our spectral sample includes both time-resolved and time-integrated spectra for each burst: the time-resolved spectra within each burst has the best possible time resolution for the high-energy resolution data types used, and the time-integrated spectra are the sum of the resolved spectra within the bursts, covering entire duration of the bursts. We obtain well-constrained spectral properties by studying characteristics of each photon model, taking into account the parameterization differences, and statistically determining the best-fit model for each spectrum. The analysis performed here is much more comprehensive and consistent than that of SP1 in the sense that (i) only LAD data are used, (ii) the burst sample selections are more objective, (iii) five different photon models are fitted to each spectrum, both time-integrated and time-resolved, and (iv) the best-fit parameters of each spectrum are statistically determined. The use of various models allows us to compare the behavior of different models as well as to obtain unbiased

¹<http://gammaray.nsstc.nasa.gov/batse/grb/catalog/current/>

statistics for the spectral parameters. We also note that the BATSE data and the Detector Response Matrices (DRMs) used here have been regenerated since the publication of SP1, with a refined detector calibration database. This provided more precise LAD energy edges, thus assuring the improved accuracy of the spectral analysis.

Since our sample only includes bright bursts, there may be some bias in our analysis results. As reported previously in literature, there is a tendency of bright bursts being spectrally harder than dimmer bursts (e.g., Nemiroff et al. 1994; Mallozzi et al. 1995; Dezalay et al. 1997). Therefore, it is likely that our sample of bright bursts belongs to the harder side of the overall BATSE GRB sample, on average (e.g., Lloyd, Petrosian & Mallozzi 2000). It is particularly important to keep this in mind when studying global correlations with our spectral analysis results. Our selection criteria also excludes many bright short bursts with duration much less than a second. As a result, only $\sim 5\%$ of our sample are short bursts (duration < 2 s) while short bursts comprises $\sim 19\%$ of the entire BATSE GRB sample.

The paper is organized in the following manner. We first describe the burst sample and analysis interval selection methodology in §2. The details of the spectral analysis methods are then discussed in §3, including descriptions of the photon models used. We also discuss our simulation results in §4, which were performed to assist us in interpreting the analysis results correctly. Finally, the analysis results are presented in §5 and summarized in §6. We note that there are two ways of identifying a BATSE burst; by the GRB name (“GRB *yymmdd*”) and by the BATSE trigger number. We use both the names and trigger numbers to refer to individual GRBs throughout this paper².

2. Selection Methodology

During its nine-year lifetime that ended in June 2000, BATSE triggered on a total of 8021 gamma-ray transient events, of which 2704 events were identified as GRBs. The BATSE detectors were sensitive enough to detect relatively weak GRBs down to a peak photon flux in 256 ms of $\sim 0.3 \text{ s}^{-1} \text{ cm}^{-2}$ (50 – 300 keV) and a total energy fluence in 25 – 2000 keV of $\sim 10^{-8} \text{ ergs cm}^{-2}$. Unfortunately, many dim bursts do not provide enough signal above background for high energy resolution spectral analysis, particularly for time-resolved spectroscopy. Therefore, we need to select and limit our analysis to GRBs with

²Tables 1 and 9 list both the GRB names and the BATSE trigger numbers for the GRBs in our sample. For other BATSE-triggered events, a lookup table to convert between them is available at http://gammaray.nsstc.nasa.gov/batse/data/trigger_lookup.html

sufficient signal. In addition, the available data types and data ranges vary for each burst. In this section, we describe the methodology employed for the burst selection, the data type selection, and time and energy interval selections.

2.1. Burst Sample Selection

The primary selection was made based on the peak photon flux and the total energy fluence in the BATSE 4B catalog (Paciesas et al. 1999), as well as the current BATSE GRB catalog¹ for the post-4B bursts. The catalogs list a total of 2702 GRBs, of which two were later identified as non-GRBs (trigger numbers 5458 and 7523). Additionally, there are four triggered events that were later identified as GRBs (trigger numbers 1505, 2580, 3452, and 3934), bringing the total number of BATSE GRBs to 2704. The number is consistent with the final BATSE 5B catalog (M.S. Briggs et al. in preparation). Our sample was selected from these 2704 bursts. The burst selection criteria are a peak photon flux in 256 ms (50 – 300 keV) greater than $10 \text{ photons s}^{-1} \text{ cm}^{-2}$ or a total energy fluence in the summed energy range ($\sim 20 - 2000 \text{ keV}$) larger than $2.0 \times 10^{-5} \text{ ergs s}^{-1}$. Having the criteria in either the peak photon flux or total energy fluence allows inclusion of short bright bursts as well as long bursts with low peak flux. The peak photon flux criterion remains the same as SP1, although it was misstated in SP1 as a 1024-ms integration time. The energy fluence criterion has been lowered from the value used in SP1 so as to include more bursts, while still securing sufficiently good statistics. A total of 298 GRBs satisfied these criteria.

In addition, 573 GRBs out of 2704 do not have flux/fluence values published in any BATSE GRB catalog, mainly due to gaps in the four-channel discriminator data that were used to obtain the flux/fluence values. Nonetheless, for many of these bursts, finer energy-resolution data are still available for spectral analysis, and some are bright enough to be included in this work. Therefore, we estimated the photon flux and the energy fluence values for the bursts with no published flux/fluence values, using available data. To estimate the peak photon flux and energy fluence for such bursts, we used 16-channel MER data (see §2.3 below for the description of the data type) binned to a 256-ms integration time and fitted with a smoothly-broken power-law model (described later in §3.2.5). The peak photon flux values (in 256 ms, $\sim 50 - 300 \text{ keV}$) and the total energy fluence values (in $\sim 30 - 1900 \text{ keV}$) were calculated from the fitted spectra. We note that using other photon models barely changed the outcome. There were some cases where MER data were not available but either HERB or CONT data existed. Most of these cases, however, turned out to be noticeably very weak, or else all of the available data were not complete, and therefore did not qualify for inclusion. In this way, 55 GRBs yielded peak photon flux or total energy fluence values

well above our threshold criteria, and were therefore included in this work.

Out of these selected bright bursts, we found two cases (trigger numbers 3366 and 7835) in which the published flux/fluence values were incorrect and the actual flux/fluence values were much lower than the criteria used here. Consequently, these two bursts were excluded. We also found one case (trigger number 5614, peak photon flux = $182 \text{ photons s}^{-1} \text{ cm}^{-2}$) in which the burst was so bright that the indication of possible pulse pile-up was seen in the energy spectra of all available detectors and the data were not usable. Thus, this burst was also excluded from this work. The resulting total number of GRBs included in this spectral analysis was 350. The GRBs are listed in Table 1, along with the data types, time and energy intervals, and numbers of time-resolved spectra contained.

2.2. Detector Selection

BATSE was specifically designed to detect GRBs and to study their temporal and spectral characteristics in great resolution. In order to increase the GRB detection probability, BATSE consisted of eight modules that were located at the corners of the *CGRO* spacecraft, so as to cover the entire 4π steradian of sky. Each module comprised two types of detectors; LAD and SD. They were both NaI(Tl) scintillation detectors of different dimensions designed to achieve different scientific goals. The LADs were 50.8 cm in diameter and 1.27 cm in thickness, and provided burst triggering and burst localizations with high sensitivity. They were gain-stabilized to cover the energy range of $\sim 30 \text{ keV} - 2 \text{ MeV}$. The SDs were 12.7 cm in diameter and 7.62 cm in thickness, and provided a higher energy resolution in $\sim 10 \text{ keV} - 10 \text{ MeV}$, depending on the gain of each detector at the time of a burst trigger.

In this spectral analysis, only the LAD data are used, mainly to take advantage of its larger effective area (Fishman et al. 1989). Another reason that only the LAD data are used is due to a problem recently identified in the SD DRMs at energies above $\sim 3 \text{ MeV}$ (Kaneko 2005). These problems could give rise to uncertainties in the SD DRMs and make SD data unreliable for spectral analysis at high energies. Moreover, limiting to one type of detector eliminates systematic uncertainties arising from different detector characteristics, and thus keeps the analysis more uniform. For each burst, the data from the LAD with the highest counts are used.

2.3. Data Type Selection

The LADs provided various types of data products to be used for various purposes. The data were collected in either burst mode or non-burst mode. The burst mode data accumulation started when a burst was triggered, whereas the non-burst mode data were usually continuous, except for possible telemetry gaps. The burst mode data generally provided higher resolution either in energy or in time than the non-burst mode data. The three LAD data types used in this work, in order of priority, are High Energy Resolution Burst data (HERB), Medium Energy Resolution data (MER), and Continuous data (CONT). The characteristics of each data type are listed in Table 2 (see SP1 for more complete list of BATSE burst data types). The HERB and MER data are burst-mode data, for which the acquisition began at the time of a burst trigger, whereas CONT was continuous, non-burst mode data. The accumulation time of the HERB data is rate dependent, with minimum time-to-spill of 128 ms with a 64-ms increment. HERB provides the highest energy resolution consisting of ~ 120 usable energy channels in energy range of $\sim 30 - 2000$ keV with modest sub-second time resolution, and thus is used as the primary data type. For each burst, the HERB data for the brightest LAD provides the finest time resolution, and was always selected for the analysis. The coarser-time resolution (~ 300 s) High Energy Resolution data (HER) are used as background data for the HERB, covering several thousand seconds before the trigger and after the HERB accumulation is finished. However, especially for long, bright bursts, the HERB data can often be incomplete since HERB had a fixed memory space that could fill up before the burst was over. In this work, we consider the HERB data incomplete when the data do not cover the burst duration (T_{90}) or when the data do not include the main peak episodes (this could occur if a burst data accumulation was triggered by weak precursor). In such cases, or if HERB was not available, 16-energy-channel MER data were used instead. Although MER provides medium energy resolution, it has much finer time resolution (16 and 64 ms) than HERB, making it possible to re-create the time resolution of the missing HERB. In the MER data, the CONT data are used as background; therefore, the spectra accumulated before the trigger time and after 163.8 seconds (the MER accumulation time) are identical to those of CONT, with 2.048-s integration times. The downside of using MER is that the data are summed over multiple sets of detectors (usually two to four), and therefore, systematic errors tend to dominate over statistic errors, especially for bright bursts. Systematic errors cannot be modeled into the analysis and can contribute to large χ^2 especially at lower energies due to the high counts. This systematic effects can also be visible in the single-detector data (HERB and CONT) but are much more often found in the MER data of bright bursts. Examples of HERB and MER spectra of the same bright burst (GRB 910503, trigger number 143) that show such systematic deviations are seen in Figure 1. Possible contributions to the systematics include the uncertainties from the LAD

calibration (Preece et al. 1998a) and the DRM (Pendleton et al. 1995; Harmon et al. 2002).

Lastly, in the cases where neither HERB nor MER were available for the analysis, 16-energy-channel CONT data with 2.048-s time resolution from the brightest LAD were used. Despite the lack of sub-second time resolution, the advantage of CONT is that the data are from a single detector and continuous. Thus, significant precursor activities may be included in the analysis using the CONT data. This was not possible for HERB, because the data accumulations always started at triggers, and the background data (HER) did not provide a sufficient time resolution for pre-trigger data. For each of 350 bursts, the data type used is listed in column 4 of Table 1, and the total number of bursts using each data type is 270 (HERB), 52 (MER), and 28 (CONT).

2.4. Time Interval Selection

We binned the data in time until each spectrum has a large enough signal-to-noise ratio (S/N) in the entire LAD energy band to ensure acceptable statistics for the time-resolved spectral analysis. The S/N is calculated based upon the background model of each burst. The background model is determined by fitting (each energy channel separately) a low-order (≤ 4) polynomial function to spectra that cover time intervals before and after each burst, for at least a few hundred seconds. In cases where the background data are not available for a sufficiently long period, the longest available time intervals were used, and the background model was checked against those determined using other LAD data available for the same burst. The burst start time is usually the trigger time. In the cases where CONT or MER were used, bright pre-trigger activity (containing significant amount of emission) was also included in the analysis, and thus the start time can be negative relative to the trigger time.

In SP1, a minimum S/N of 45 was used for the time binning of spectra regardless of the data types used. The S/N level was chosen so that each spectral resolution element (non-overlapping full-width at half-maximum resolution elements, of which there are about 16 – 20 in the LAD energy range) has approximately 10σ of the signal on average, assuming a flat spectrum. The noise (or σ) defined here is the Poisson error of the observed total counts, including the background counts. Binning by a constant S/N, however, usually yields on average a few times larger number of time-resolved spectra when MER data are used, than the HERB and CONT cases. This is because the MER data are summed over two to four detectors, while HERB and CONT are single-detector data, and thus the MER data have higher S/N to begin with, on top of having a finer time resolution. As a result, bursts with MER data were overrepresented in the time-resolved spectral sample of SP1 due to the choice of data type, which in turn slightly biased the spectral parameter and model statistics

presented there. The MER bursts do provide more time-resolved spectra on average since we use the MER data for long, bright GRBs; however, this is caused by the nature of the bursts and should not be caused by the choice of data type. To minimize the over-representation caused by the data type selection, we investigated which S/N value for MER would yield comparable numbers of time-resolved spectra compared with HERB binned by $S/N \geq 45$, for the same bursts. Since the MER data are mainly used for bright, long bursts, and also the oversampling problems are more likely to occur when the photon flux is high, we selected 15 bursts with high peak photon flux ($\gtrsim 50$ photons $\text{s}^{-1} \text{cm}^{-2}$ in 128 ms, $\sim 30 - 2000$ keV, determined using HERB data), for which both MER and HERB data were available. We re-binned the HERB data with minimum S/N of 45, and reproduced the same number of spectra for the same time intervals with MER data, by increasing the minimum S/N in steps. We found that a minimum S/N of 45 *per detector* could roughly accomplish this, regardless of the brightness, as shown in Figure 2. Therefore, the minimum S/N used for the time binning is $45 \times \text{number of detectors}$, with the exception of 10 MER bursts. These 10 bursts were mostly with three or four detectors and the minimum S/N was found to be too high, for various reasons, when compared with the available portion of single-detector data (i.e., HERB or CONT) for the same burst. Consequently, for these bursts, the minimum S/N was reduced by steps of 45 until the binning comparable to that of HERB was achieved.

After time-binning by the minimum S/N, the last time interval, with a S/N less than the minimum value, was dropped. Although the last time bin may constitute a significant tail portion of the burst, we found that this exclusion of the last time bin does not greatly affect the time-integrated spectral fits. This is true even when the resulting time interval that is fitted is much shorter than the T_{90} of the burst (e.g., a burst with a very long tail). Unlike for SP1 where bursts with less than eight spectra were dropped, no bursts that satisfy the burst selection criteria described above are excluded, regardless of the resulting number of spectra after binning in each burst. This allowed the inclusion of 17 short GRBs ($T_{90} < 2.0$ s) as well as several dimmer bursts in this work. Note that a set of time-resolved spectra comprises the time-integrated spectrum of each burst; therefore, the time interval of the integrated spectrum is the sum of the intervals of all the resolved spectra within the burst. Most integrated spectra cover the T_{90} duration. Columns 6 and 7 of Table 1 list the time intervals used for each burst. There are 11 bursts (BATSE trigger numbers 298, 444, 1525, 2514, 2679, 3087, 3736, 6240, 6293, 7457, 7610) that provided only one spectrum as a result of the time binning. In addition, there are six weak bursts (2112, 3044, 3410, 3412, 3917, and 6668) for which the detection of the entire event was $< 45\sigma$: they provided only one spectrum of 28σ , 15σ , 26σ , 28σ , 40σ , and 28σ , respectively. These six spectra were still included in the sample for completeness. Four of these six bursts are short GRBs. For these bursts that provided only one spectrum, the same spectra are considered as both the time-

integrated and time-resolved spectra, and they are indicated by the prefix “W” in column 1 of Table 1. It must also be noted that there are eight bursts (indicated by the prefix “C” in column 1 of Table 1) whose time-integrated spectra were used for calibration of the eight LADs (Preece et al. 1998a). Since the fits to a two-component empirical GRB model (§3.2, Equation 2) was used for the calibration, the time-integrated spectra of these calibration bursts are, by default, expected to give small χ^2 values when fitted with a two-component model (Equations 2 & 4), although the time intervals used for the calibration and for this work are different.

2.5. Energy Interval Selection

All LADs were gain-stabilized; therefore, the usable energy range for spectral analyses is ~ 30 keV – 2 MeV for all bursts. The lowest seven channels of HERB and two channels of MER and CONT are usually below the electronic lower-energy cutoff and were excluded. Likewise, the highest few channels of HERB and normally the very highest channel of MER and CONT are unbounded energy overflow channels and also not usable. The actual energy range used in the analysis for each burst is shown in columns 8 and 9 of Table 1.

3. Spectral Analysis

Our sample consisted of 350 GRBs, providing 350 time-integrated spectra and 8459 time-resolved spectra. We analyzed both time-integrated and time-resolved spectra, each fitted by a set of photon models that are commonly used to fit GRB spectra. Each of the photon models used consists of a different number of free parameters and thus, provides different degrees-of-freedom (dof) for each fit. This allows statistical comparisons among the model fits. The fitting procedures and the photon models are discussed in this section.

3.1. Spectral Fitting Software

For the spectral analysis presented herein, we used the spectral analysis software RM-FIT, which was specifically developed for burst data analysis by the BATSE team (Mallozzi, Preece & Briggs 2005). It incorporates a fitting algorithm MFIT that employs the forward-folding method (Briggs 1996), and the goodness of fit is determined by χ^2 minimization. One advantage of MFIT is that it utilizes model variances instead of data variances, which enables

more accurate fitting even for low-count data (Ford et al. 1995). We analyzed both time-integrated and time-resolved spectra for each burst, using a set of photon models described below.

3.2. Photon Models

We have selected five spectral models of interest to fit the BATSE GRB spectra, three of which (BAND, COMP, and SBPL) were also employed in SP1. Having a variety of models in fitting each spectrum eliminates the need for manipulating one model, such as the “constrained” Band function introduced by Sakamoto et al. (2004), which requires some presumptions of the form for the original photon spectrum. GRB spectra are usually well-represented by a broken power law in the BATSE energy band. However, it is possible that the break energy lies outside the energy range, or that the spectrum is very soft or dim and the high-energy component is not detected. Therefore, we use a single power-law and a power-law with exponential cutoff model that may accommodate such spectra, in addition to the more commonly-fit broken power-law models. We review each model used in the analysis below. All models are functions of energy E , measured in keV.

3.2.1. Power Law Model (PWRL)

The first model is a single power law with two free parameters,

$$f_{\text{PWRL}}(E) = A \left(\frac{E}{E_{\text{piv}}} \right)^{\lambda}, \quad (1)$$

where A is the amplitude in photons $\text{s}^{-1} \text{ cm}^{-2} \text{ keV}^{-1}$, λ is a spectral index, and the pivot energy E_{piv} was kept constant at 100 keV for this work. The use of this model was motivated by the fact that the break energy of a broken power law spectrum could lie well outside the LAD passband. There may also be a case where the signal is weak and the break energy cannot be adequately determined. In such cases, the two-parameter single power law should be able to fit the spectra better than the other models with more parameters.

3.2.2. The GRB Model (BAND)

The next model is the empirical model most widely used to fit GRB spectra (Band et al. 1993):

$$\begin{aligned} f_{\text{BAND}}(E) &= A \left(\frac{E}{100} \right)^\alpha \exp \left(-\frac{E(2+\alpha)}{E_{\text{peak}}} \right) \quad \text{if } E < E_c \\ f_{\text{BAND}}(E) &= A \left[\frac{(\alpha - \beta)E_{\text{peak}}}{100(2+\alpha)} \right]^{\alpha-\beta} \exp(\beta - \alpha) \left(\frac{E}{100} \right)^\beta \quad \text{if } E \geq E_c, \end{aligned} \quad (2)$$

where

$$E_c = (\alpha - \beta) \frac{E_{\text{peak}}}{2 + \alpha} \equiv (\alpha - \beta) E_0.$$

The model consists of four parameters: the amplitude A in photons $\text{s}^{-1} \text{cm}^{-2} \text{keV}^{-1}$, a low-energy spectral index α , a high-energy spectral index β , and a νF_ν peak energy E_{peak} in keV, which is related to the e -folding energy, E_0 . νF_ν spectrum represents the total energy flux per energy band (i.e., power density spectrum, $E^2 f(E)$). We stress that the α index characterizes an asymptotic power-law (i.e., the tangential slope determined at $E = 0$ in a logarithmic scale). This may not characterize the actual logarithmic tangential slope determined within the data energy range, when the e -folding energy E_0 approaches the lower energy bound. It has now become common practice to use this empirical model to fit both time-integrated and -resolved GRB spectra. Very frequently, however, we find some time-resolved spectra cannot be adequately fitted with this model. By fitting this model to both time-integrated and time-resolved spectra, we test the validity of the scope of this model.

3.2.3. The GRB Model with fixed β (BETA)

The BETA model is a variation of the BAND, with a fixed high-energy index β , and is only used to fit the time-resolved spectral fits. The fixed value of β is determined from the time-integrated spectral fit using the regular BAND model. Since β is fixed in the fit, this is essentially a 3-parameter model with A , α , and E_{peak} . Our motivation for using this model is to test the hypothesis that the energy distribution of the shock-accelerated electron remains constant throughout a burst. The post-shock electron distribution should be thermal at low energies and non-thermal (power law) at high energies (Tavani 1996; Baring & Braby 2004). The synchrotron spectrum emitted by electrons in a power-law distribution, $N(\gamma)d\gamma = \gamma^{-p}d\gamma$, is a power-law of index $-(p+1)/2$ (Rybicki & Lightman 1979), which should correspond to the high-energy index, β . It has been found that for Fermi-type acceleration, the accelerated particles have a power-law distribution with index

$p \sim 2.2 - 2.3$ that is constant in time (Gallant 2002). Therefore, if p remains constant throughout a burst, β should also remain constant in the context of the synchrotron shock model. In fact, it has been found with a smaller sample that the majority of GRBs do not exhibit strong evolution in β (Preece et al. 1998a), so we examine this here with a larger sample.

3.2.4. Comptonized Model (COMP)

The next model considered is a low-energy power law with an exponential high-energy cutoff. It is equivalent to the BAND model without a high energy power law, namely $\beta \rightarrow -\infty$, and has the form

$$f_{\text{COMP}}(E) = A \left(\frac{E}{E_{\text{piv}}} \right)^{\alpha} \exp \left(-\frac{E(2 + \alpha)}{E_{\text{peak}}} \right). \quad (3)$$

Like the PWRL case, E_{piv} was always fixed at 100 keV in this work; therefore, the model consists of three parameters: A , α , and E_{peak} . There are many BATSE GRB spectra that lack high-energy photons (Pendleton et al. 1997), and these no-high-energy spectra are usually fitted well with this model. Another case where this model would be a good fit is when the e -folding energy ($E_0 \equiv E_{\text{peak}}/(2 + \alpha)$) approaches ~ 1 MeV, and the high-energy index of the BAND model cannot be determined by the data. The model is so named because in the special case of $\alpha = -1$, it represents the Comptonized spectrum from a thermal medium; however, α is kept as a free parameter here. Note that when $\alpha < -2$, the exponential term in the model diverges (i.e., $E_0 < 0$), and the resulting spectrum has a concave-up shape.

3.2.5. Smoothly-Broken Power Law (SBPL)

The last model we have selected is a broken power law with flexible curvature at the break energy, and thus the model can accommodate spectra with very sharp breaks, as well as ones with very smooth curvature. This SBPL model is expressed by

$$f_{\text{SBPL}}(E) = A \left(\frac{E}{E_{\text{piv}}} \right)^b 10^{(a - a_{\text{piv}})}, \quad (4)$$

where

$$a = m\Lambda \ln \left(\frac{e^q + e^{-q}}{2} \right), \quad a_{\text{piv}} = m\Lambda \ln \left(\frac{e^{q_{\text{piv}}} + e^{-q_{\text{piv}}}}{2} \right),$$

$$q = \frac{\log(E/E_{\text{b}})}{\Lambda}, \quad q_{\text{piv}} = \frac{\log(E_{\text{piv}}/E_{\text{b}})}{\Lambda},$$

$$m = \frac{\lambda_2 - \lambda_1}{2}, \text{ and } b = \frac{\lambda_1 + \lambda_2}{2}.$$

The parameters are the amplitude A in photons $\text{s}^{-1} \text{ cm}^{-2} \text{ keV}^{-1}$, a lower power-law index λ_1 , a break energy E_b in keV, a break scale Λ , in decades of energy, and an upper power-law index λ_2 . The amplitude A represents the photon flux at E_{piv} . The model introduces a break scale Λ as the fifth parameter; this is thus a five-parameter model. Like the PWRL and COMP models above, the pivot energy E_{piv} is always fixed at 100 keV here. The amplitude A is determined at this E_{piv} , and it represents a convenient overall energy scale. This model was originally created to be implemented into MFIT, and the full derivation is found in Appendix A. The basic idea in deriving this model was to have the derivative of the photon flux (in logarithmic scale) to be a continuous function of the hyperbolic tangent (Preece et al. 1994; Ryde 1999, SP1). The main difference between this model and the BAND model is that the break scale is not coupled to the power laws, and it approaches the asymptotic low-energy power law much quicker than the BAND model case. Therefore, the low-energy spectral index λ_1 could characterize values that are closer to the *true* power law indices indicated by the actual data points, than is possible with α of the BAND model. Note also that as $\Lambda \rightarrow 0$, the model reduces to a sharply-broken power law.

However, introducing a fifth parameter can be a problem in fitting the LAD spectra. Although the HERB data provides 126 energy channels, the energy range encompasses only about 20 energy resolution elements, as mentioned earlier. Fitting a four-parameter model to the HERB data can already cause the covariance matrix between parameters $[C]$ to be ill-determined, resulting in unconstrained parameters. This is indicated by a condition number for $[C]^{-1}$ that is of the order of the reciprocal of the machine precision, meaning that the matrix is nearly singular (e.g., Press et al. 1992). Consequently, having an additional free parameter usually results in highly cross-correlated, unconstrained parameter determinations, and is not favored. For this reason, in SP1, Λ was fixed for each time-resolved spectral fit to the value determined by the time-integrated fit for the corresponding burst; however, there is no reason to presume that Λ remains constant throughout a burst, and also it could be problematic if the initial time-integrated break scale is unconstrained. On the other hand, we may not be able to constrain Λ any better than a particular value, due to the finite energy resolution of the LADs, even if the five-parameter model fit can be done. To resolve this issue, we have simulated SBPL spectra with various parameters and fitted these spectra with the SBPL model for various values of Λ . The simulation results are discussed in §4.2.

We emphasize that the break energy E_b of the SBPL model should not be confused with E_{peak} of the BAND and COMP models. The break energy is simply the energy at which the spectrum changes from the low-energy to high-energy power law, whereas E_{peak}

is the energy at which the νF_ν spectrum peaks. The break energy E_b is also different from the characteristic energy E_c in the BAND model (Equation 2), which is the energy where the low-energy power law with exponential cutoff ends and the pure high-energy power law starts. However, the νF_ν peak energy of the SBPL spectra, as well as the spectral break energy of BAND, can be easily derived (see the Appendices B and C) for comparison among the various models, which we have done here for the first time.

4. Spectral Simulations

In order to interpret the quantitative analysis results correctly, we first need to understand the general characteristics and behavior of each photon model when applied to the BATSE LAD GRB spectra. Therefore, we have generated a large set of simulated burst spectra with various spectral shapes and signal strengths, and subjected them to our analysis regime. To create a set of simulated count spectra, a source photon model with specific parameters and a background count model of an actual (typical) LAD burst are folded through the corresponding LAD DRM, and Poisson noise is added. It should be noted that the simulated spectra do not include any sources of systematic effects that are present in the real spectra. There are two main objectives in simulating data for this study. One is to investigate the behavior of the BAND and COMP models in the limit of low S/N and the other is to explore the break scale determination of SBPL.

4.1. BAND vs. COMP

The broken-power law nature of the GRB spectra indicates that there typically are considerably lower photon fluxes at higher energies. Because of this, there is a good chance that the LADs are not sensitive enough to detect the non-thermal high-energy power law component of spectra in fainter bursts. In such cases, even if the original source spectra have high-energy components, our data may not be able to identify this component and therefore, the no-high-energy COMP model may statistically fit as well as the BAND model. As an example, we show in Figure 3 a comparison between the BAND and the COMP photon spectra with the same A , α , and E_{peak} values. In fact, Band et al. (1993) found that the simulated four-parameter BAND spectra with low S/N could be adequately fitted with the three-parameter COMP model, although there were some shifts in the COMP-fit parameters. In order to validate this for our dataset and using our analysis tool (RMFIT, §3.1), we have further explored these two models by creating sets of simulated burst spectra, based on the

actual fit parameters of some of the observed GRB spectra that clearly have high-energy components.

To start with, we selected a sample of six bright GRB spectra (three each with HERB and CONT) to which the BAND model fits substantially better than the COMP model, with well-constrained parameters, resulting in large χ^2 improvements ($\Delta\chi^2 > 20$) for the additional 1 dof. This assures that the observed spectra have a high-energy power law component that is statistically significant. Based on the spectral parameters provided with the BAND fits to the sample spectra (i.e., spectra with high-energy component), sets of 100 simulated spectra with various S/N were created. For the S/N variation, we used the actual fitted amplitude value and the values decreased by a step of a factor of 10 until the S/N was a few. As a result, a total of 19 sets provided $2 \lesssim \langle \text{S/N} \rangle \lesssim 200$ in the entire LAD energy range, based on the typical LAD background count model that was taken as input for the simulation.

The sets of simulated spectra were then fitted with the BAND and the COMP models. Some example results are presented in Table 3 (upper two tables), where $\langle x \rangle$ indicates a median value of the parameter x and the standard deviation is $\sigma_x = \sqrt{\langle x^2 \rangle - \bar{x}^2}$. The fit results indicated that $\text{S/N} \gtrsim 80$ is needed for the BAND fits to be better than the COMP fits, at $\gtrsim 99.9\%$ confidence level ($\Delta\chi^2 > 10$ for $\Delta\text{dof} = 1$). For spectra with $\text{S/N} \sim 40$, the confidence level of improvements in BAND over COMP were $< 70\%$. Given that the minimum S/N of our time-resolved spectra in this work was set to 45, for many dimmer spectra we should only be able to determine a better fit between the BAND and COMP by only about 1σ (68.3%), although this may depend on the spectral parameters in each fit.

In accord with the Band et al. (1993) results, the COMP model resulted in higher E_{peak} values and steeper values of α , due to compensating for the lack of high-energy spectral component in the model. Consequently, the difference in the COMP E_{peak} and the actual E_{peak} value tends to be correlated with β . In addition, a strong anti-correlation was always found between E_{peak} and α in both BAND and COMP fits, regardless of S/N or values of other parameters. As a result, the amplitude A is also highly anti-correlated to E_{peak} because the parameter A of BAND and COMP is the photon flux at 100 keV of the low-energy power-law *without* the exponential cutoff. This is different from A of the SBPL model. We also fitted the five-parameter SBPL model to the same sets of simulated BAND spectra, to investigate the possible parameterization differences in the indices. We found that the SBPL λ_1 tends to be smaller than α while λ_2 seems to be consistent with β , as we expected.

Similarly, we have also simulated sets of COMP spectra with low and high E_{peak} values (300 and 760 keV, respectively) with different S/N ($80 \lesssim \langle \text{S/N} \rangle \lesssim 500$), and fitted them

with the BAND model. The results are summarized in Table 3 (lower two tables). In the high E_{peak} case, we found that the BAND fits did not converge about a third of the time, regardless of the S/N. The fitting failure is caused by a very poorly-constrained parameter (β in this case). On the other hand, in the low E_{peak} case, the number of failed fits was significantly smaller for the spectra with lower S/N. In both cases, the $\langle E_{\text{peak}} \rangle$ and $\langle \alpha \rangle$ values fitted by the BAND model were consistent with the simulated COMP parameters, while $\langle \beta \rangle$ only gave upper limits in a range of ~ -2.5 to ~ -4 . The simulation results suggest that the BAND model fails to converge when a spectrum has sufficient high-energy photon flux but lacks the high-energy power-law component with finite spectral index. The spectrum in such a case essentially is the COMP model, which is the BAND model with $\beta \rightarrow -\infty$ (see §3.2.4). As an example, Figure 4 shows two COMP models that produced simulated spectra with S/N ~ 80 but with different E_{peak} values. As mentioned above, the BAND model fails to fit the high- E_{peak} spectrum much more frequently than the low- E_{peak} one. From Figure 4, it is evident that the high- E_{peak} spectrum has much larger photon flux at about 1 MeV although the overall signal strengths are similar. Therefore, it is very likely that the spectra that the BAND model fails to fit lack a high-energy power law component, yet this does not mean that these are the no-high-energy (NHE) spectra identified by Pendleton et al. (1997), which show no counts above 300 keV.

4.2. SBPL Break Scales

Another topic that needs to be addressed is the break scale (Λ) of the SBPL model, as mentioned in §3.2.5. The purpose of this simulation is to test the feasibility of performing the 5-parameter SBPL model fits with Λ as a free parameter, as well as to examine the capability of the determination of Λ by alternatively using a set of 4-parameter SBPL models with fixed Λ . First, we created sets of 100 simulated SBPL spectra with Λ values 0.01 and between 0.1 and 1.0 with an increment of 0.1 (11 total, in decades of energy), while keeping the other parameters fixed at typical fit values of $E_b = 300$ keV, $\lambda_1 = -1.0$, and $\lambda_2 = -2.5$. Figure 5 shows the 11 simulated spectra in νF_ν , with $A = 0.05$. The upper limit of $\Lambda = 1.0$ (in decades of energy) is reasonable, considering that the LAD spectra span less than two decades of energy. The spectrum with $\Lambda = 0.01$ represents a sharply-broken power law. To provide variations in the signal strength, the amplitude A was set to a typical value of 0.05 in one group, and was 0.01 in the other group, corresponding to the median S/N of ~ 100 and ~ 30 per spectrum, respectively. Each of the simulated spectra was then fitted with the full 5-parameter SBPL model allowing Λ to vary, with a set of 4-parameter SBPL models, each with Λ fixed to the 11 values mentioned above, as well as with the BAND and the COMP models for comparison.

4.2.1. Finding the Break Scale

In Figure 6, we show the Λ values found by the 5-parameter SBPL model fits, with Λ as a free parameter. For the high S/N case, the correct Λ values were found up to $\Lambda \sim 0.6$, with relatively small dispersions. For the low S/N case, only the very sharp break ($\Lambda = 0.01$) was constrained by the 5-parameter fits. As for the other parameters associated with the fits, we found that even for the bright cases, the 5-parameter fits resulted in relatively large uncertainties in all parameters, which worsened as Λ became larger. This was also indicated by the large cross-correlation coefficients among all parameters, resulting from the fits. This confirms that fitting five free parameters at once does not determine the parameter with a good confidence, regardless of the S/N of spectrum, and therefore, the full 5-parameter fit is not favored. It is, however, worth noting that despite the large errors, Λ found by the 5-parameter fits may still provide a rough estimate of the break scale even for faint spectra, as a last resort.

Alternatively, we could employ the grid-search method (Bevington & Robinson 2003) using a subset of 4-parameter SBPL fits with various fixed values of Λ to determine the real Λ . Having such a set of 4-parameter model fits to each spectrum enables us to construct a one-dimensional χ^2 map for Λ , showing χ^2 as a function of Λ . From the χ^2 map, we can determine the most likely value of Λ (where the χ^2 is minimum) as well as the confidence interval, while having the other parameters still constrained.

The $\langle \chi^2 \rangle$ map obtained from a 4-parameter model fitting of the bright (S/N ~ 100) simulated spectra is shown in Figure 7. We find from the χ^2 map that for $\Lambda \leq 0.4$ the set of 4-parameter fits yields a minimum for χ^2 at the correct Λ values with 1σ uncertainties less than 0.01. However, for $\Lambda \geq 0.5$, the Λ value could not be sufficiently constrained, especially at the upper ends, and the BAND model starts to give satisfactory fits that are statistically comparable to the SBPL model fits. This suggests that in the case of $\Lambda \geq 0.5$ we can only determine the lower limit of $\Lambda = 0.5$ with confidence. Furthermore, for $\Lambda > 0.6$, the uncertainties associated with other spectral parameters become large although they are still in agreement within the uncertainties with the simulated values. As for the faint spectra (S/N ~ 30), we found that the total change in χ^2 for the entire set of Λ values was only about 4, which is within the 2σ confidence interval for $\Delta\text{dof} = 1$; therefore, the correct value of Λ cannot be determined even with the use of 4-parameter fits, due to the low S/N. In such cases, however, we also found that the Λ determined from the 5-parameter SBPL fit can be used as an estimate. In other words, the fit using a 4-parameter model with Λ closest to the Λ found from the 5-parameter fit could yield parameters that are adequately constrained and still consistent with the actual simulated parameters. The simulation was done both with 128-energy channel data and 16-energy channel data, in order to investigate the possible

effects that might arise from the energy resolution issues. We found no differences between the 128-channel data and the 16-channel data in determining the break scales.

Based on these simulation results, we concluded that the 4-parameter SBPL models with $\Lambda > 0.5$ do not contribute much additionally to our analysis; therefore, we decided to use a set of 4-parameter SBPL models with $\Lambda = 0.01, 0.1, 0.2, 0.3, 0.4$, and 0.5 , as well as 5-parameter SBPL model with Λ varied, and Λ fixed to the time-integrated fit value (for comparison with SP1). With regard to cross-correlations among the spectral parameters, E_b and λ_2 are found to be always strongly anti-correlated in both 4-parameter and 5-parameter fits. Moreover, the 4-parameter fits where Λ is fixed tend to produce higher anti-correlation between E_b and λ_1 than the 5-parameter cases, which is expected for the fixed break scale cases. Not surprisingly, in the 5-parameter fits, the λ_1 (λ_2) is more strongly correlated (anti-correlated) with Λ , as Λ becomes larger. There was no explicit difference found in these cross-correlations according to S/N, although in the faint case, the parameters were more difficult to be constrained.

4.2.2. Comparison with BAND & COMP

The simulated SBPL spectra were also fitted with the BAND and COMP models. The results of the BAND and COMP fits to the bright simulated SBPL spectra (i.e., S/N ~ 100) are summarized in Table 4. As seen in the table (also in Figure 7), the BAND model is not able to adequately fit the SBPL spectra with relatively sharp break scale ($\Lambda \lesssim 0.3$) because of its rather inflexible, smooth curvature. The COMP model did not provide statistically acceptable fits, regardless of the Λ values, for this particular set of simulated spectra. Generally, for sharply broken spectra with small Λ , the E_{peak} and α of BAND (also COMP) are larger than the SBPL “ E_{peak} ” and λ_1 , while the BAND β is smaller than λ_2 . The opposite is true for smooth break spectra with large Λ . The tendencies are clearly seen in the example νF_ν spectra in Figure 8, in which the BAND and COMP fits to the simulated SBPL spectra with $\Lambda = 0.01$ and 0.5 are shown. The BAND model seems to fit the SBPL spectra with $\Lambda \sim 0.4$ the best, at least for these given values of E_b and $\lambda_{1,2}$. The BAND fit to this spectrum, in fact, resulted in E_{peak} consistent with the SBPL “ E_{peak} ” and α larger than λ_1 , which agrees with what was found from the SBPL fits to the simulated BAND spectra in an earlier section (§4.1). We also observe in Table 4 that the BAND fits yielded much smaller E_{peak} range ($\sim 390 - 460$ keV) than the simulated “ E_{peak} ” ($\sim 300 - 670$ keV). Although the COMP fits were significantly worse, the COMP E_{peak} was always higher and α was always softer than the BAND case, consistent with what we found in §4.1.

In terms of χ^2 statistics, for the bright spectra with $S/N \sim 100$, we find that the SBPL model can fit substantially better than the BAND model (at confidence level $> 99.9\%$) to the simulated SBPL spectra with $\Lambda \leq 0.3$; however, for the higher values of Λ , BAND begins to fit statistically as well as SBPL fits. Also in the bright spectrum case, the COMP model gave worse fits for all values of Λ , due to the lack of a high-energy component, and thus the SBPL fits were always better for this given set of the simulated spectral parameters. In the case of dim spectra with $S/N \sim 30$, on the other hand, the SBPL fitted better than the BAND or the COMP model for $\Lambda = 0.01$ and 0.1 , but only at confidence level of $\sim 90\%$. Also for the dim spectra with $\Lambda > 0.1$, we found that the BAND and the COMP fits are statistically as good as the SBPL fit.

5. Spectral Catalog and Analysis Results

We fitted the five photon models (PWRL, BAND, BETA, COMP, SBPL; see §3.2) as well as SBPL with fixed break scales ($\Lambda = 0.01, 0.2, 0.3, 0.4, 0.5$, & time-integrated value) to each of the 350 time-integrated spectra and 8459 time-resolved spectra. The spectral catalog containing all fit results is available electronically as a part of the public data archive at the High-Energy Astrophysics Science Archive Research Center (HEASARC)³. All the fit results are archived in the standard Flexible Image Transport System (FITS) format⁴. The results of the comprehensive spectral analysis performed herein constitute the richest resource of GRB prompt emission spectral properties. Therefore, careful examination of these results enables us to better constrain physical mechanisms for GRB prompt emission process. These results also allows us to explore systematics that are internal to the spectral models employed.

The overall performance of each model in fitting all spectra is summarized in Table 5, in which the percentages of acceptable fits yielded by each model are shown. The BETA model is excluded here because it is a special case of the BAND model and was used only to investigate the constant- β hypothesis in each burst. The BETA model fits are explored in §5.5. Also, the SBPL used here is the set of 4-parameter model fits, with the break scale Λ determined according to minimum χ^2 as described in §4.2. Therefore, we used the dof for 5-parameter fits to determine goodness of fits, since we are indeed allowing the break scale (the fifth parameter) to vary. From Table 5, it is clear that many spectra are adequately

³<http://heasarc.gsfc.nasa.gov/docs/archive.html>

⁴<http://fits.gsfc.nasa.gov>

fitted with various photon models. As determined solely by the χ^2 of the fits, the SBPL model seems to be able to fit the data better than the other models, as seen in the Table 5, although the values are only slightly better than those obtained by the BAND model. The time-resolved spectra provide better χ^2 values, partially due to the lower S/N compared with the time-integrated spectra. This is especially evident in the results for the COMP cases, possibly indicating the existence of NHE spectra within high-energy bursts (Pendleton et al. 1997). As expected, the PWRL model resulted in poor fits for most of the spectra. In the following sections, we look at the results of our spectral analysis in terms of the parameter distributions, the model statistics, the comparison between time-integrated and time-resolved spectra, correlations among the spectral parameters, evolution of high-energy power law index (β), and the comparison between short and long bursts.

5.1. Spectral Parameter Distributions

The spectral parameters can be compared by two different aspects; namely, a comparison among parameters yielded by different models, and a comparison between time-integrated and time-resolved parameters. The comparison among the models reveals the internal characteristics of each model, whereas the comparison between the time-integrated and time-resolved parameters uncovers the differences internal to the spectra.

Before comparing the fitted parameters of various models, there are some issues to be discussed. As mentioned in §3.2, the parameterizations are different in each model. For clarity, the free parameters in each model are summarized in Table 6. The main concern here is the difference in the low-energy spectral indices: α of BAND and COMP and λ_1 of SBPL, where α is the asymptotic power-law index, while λ_1 is the index of the actual power law fit to the data. The natural consequence of this is that α tends to be harder than λ_1 (i.e., $\alpha > \lambda_1$), when fitted to the same data, which was confirmed in the simulation study presented in §4 (we note, however, $\alpha \sim \lambda_1$ if Λ is large and/or E_b is low). They are, therefore, not directly comparable. In order to minimize the discrepancies, an “effective” α (α_{eff}) was introduced by Preece et al. (1998b). This is the tangential slope at 25 keV in a logarithmic scale, and is found to describe the data more accurately than the fitted asymptotic α value. The 25 keV is the lower energy bound of LAD and therefore, α_{eff} is the index of the low-energy power law within the data energy range. Therefore, we employ the α_{eff} instead of the fitted α values for BAND and COMP fits in the following parameter distribution comparisons. A detailed discussion of α_{eff} can be found in Appendix D.

Another issue in comparing and presenting the spectral parameter distributions is the uncertainty associated with each parameter. The parameter distribution in a large sample

can be effectively shown in a binned, histogram plot (e.g., Figure 9); however, such a plot does not include the uncertainties associated with each value. Consequently, the reliability of the distribution is not evident. One way of treating this problem is to only include well-constrained parameters in the distribution. Here, we will refer to these parameters as *good* parameters. This certainly results in providing a reliable probability distribution of a given parameter, although it could also introduce some biases depending on how the *good* class of parameters are determined. To interpret such distributions correctly, the criteria used to determine the *good* parameters are reviewed here. We first applied a χ^2 goodness-of-fit criteria of $> 3\sigma$ (99.7%) for a given dof for each fit, to assure that the resulting parameters are meaningful, before they can be considered *good*.

Low-Energy Indices. Since each model handles spectral curvature differently, the condition under which the spectral indices can be determined with good confidence differs for each model. The PWRL indices were found to be almost always constrained extremely well due to the simplicity of the model, so they can all be considered *good*. On the other hand, α (BAND and COMP) is constrained only if the e -folding energy E_0 is sufficiently above the lower energy threshold of the data. In our case, E_0 above 30 keV was considered acceptable. For SBPL λ_1 to be constrained, the lowest energy that determines the break scale must be above 30 keV. Determined from the error distributions of all low-energy indices, we allow a maximum 1σ uncertainty value of 0.4 in order for the parameters to be *good*. The value was selected so as to adequately constrain the parameters and still preserve more than 90% of all low-energy index values regardless of models.

High-Energy Indices. In order for the BAND β to be well determined, E_0 needs to be less than the upper energy limit of 1.5 MeV. For SBPL λ_2 , similar to the low-energy index case above, the maximum break scale energy has to be less than 1.5 MeV. In addition, we allow a maximum uncertainty of 1.0 for the high-energy indices, again determined from the error distributions. More than 80% of all β and λ_2 provided uncertainties smaller than this value.

E_{peak} . For BAND and COMP, E_{peak} is the fitted value, whereas for SBPL, it is the calculated value (see Appendix B for calculation). By definition, the parameter needs to represent the actual peak energy of the νF_ν spectrum. In the cases where the high-energy power-law index ≥ -2 or the low-energy power-law index ≤ -2 , the fitted E_{peak} value is just a break and not the peak of $\nu F_\nu = E^2 f(E)$. Another case in which the fitted E_{peak} value is not the νF_ν peak is when the spectrum has a shape that is concave up. This could occur in two cases; (i) the COMP fits when $\alpha < -2$ (see §3.2.4) and (ii) the SBPL fits when $\lambda_1 < \lambda_2$. The BAND model presumes $\alpha > \beta$. Therefore, to obtain final E_{peak} distributions, BAND

model fits with $\beta \geq -2$ and COMP fits with $\alpha \leq -2$ are excluded (for SBPL with $\lambda_1 \leq -2$ and $\lambda_1 < \lambda_2$, the E_{peak} was not calculated). The maximum uncertainty allowed was 40% of the parameter value for BAND and COMP, and 60% for SBPL.

Break Energy. Break energy includes the calculated E_b of BAND (Appendix C) and the fitted E_b value of SBPL. Unlike the case for the E_{peak} , the break energy does not need to be the peak of the spectrum. Therefore, the only requirement is that the parameter is within the data energy range, namely, between 30 keV and 2 MeV. This is justified by the fact that all BAND and SBPL fits with E_b values below 30 keV and above 2 MeV are associated with very large uncertainties in low-energy and high-energy indices, respectively, as well as in E_b . The maximum allowed uncertainty of 70% of the parameter value was set in order to include 85 – 90% of all break energies.

With these in mind, we can now examine the spectral parameter distributions for each model. We first compare the spectral parameters obtained by fitting all spectra with all models, in order to explore the internal characteristics of the models. In Figures 9 – 13, we present distributions of the time-integrated spectral parameters, followed by the distributions of the time-resolved spectral parameters in Figures 14 – 18, comparing all parameters and the *good* parameters obtained with each model. In addition, the median values and the dispersion (quartile values) of each distribution are listed in Table 7. The PWRL indices are included in both low-energy and high-energy index distributions because we cannot judge which power law the model represents. They are found to cluster around ~ -1.7 by themselves, which is in between the typical low-energy and high-energy indices. We note the index value agrees with the median power-law index ($\sim -1.6 \pm 0.2$; index values taken from GCN circulars⁵ and the Swift GRB table⁶) of time-integrated GRB spectra observed with the Burst Alert Telescope on board *Swift*, in the energy range of 15 – 150 keV.

As seen in these plots and the table, the corresponding parameters of different models are mostly consistent with each other within the dispersion. With the use of α_{eff} , the low-energy index distributions (Figures 9 and 14) determined by the BAND, COMP and SBPL models all seem to agree. As for the high-energy indices (Figures 10 and 15), the SBPL fits and the BAND fits also yielded consistent distributions. In the E_{peak} distributions (Figures 11 and 16), we find that the COMP fits result in higher E_{peak} values and broader distribution than the BAND and SBPL ones. Finally, the break energy distributions seen in Figures 12 and 17 indicate that the typical break energies found by the BAND fits are softer than the E_{peak}

⁵Gamma-ray burst Coordinate Network (http://gcn.gsfc.nasa.gov/gcn_main.html)

⁶http://heasarc.gsfc.nasa.gov/docs/swift/archive/grb_table.html

of the same model, due to the curvature in the spectra. The high-energy tail populations in the break energy distributions are more noticeable than the E_{peak} cases, although they are not constrained. We also present in Figures 13 and 18, the change in the spectral indices; $\Delta S \equiv \alpha_{\text{eff}} - \beta$ (BAND), $\lambda_1 - \lambda_2$ (SBPL). This parameter has been previously examined by Preece et al. (2002) using the results of SP1, in order to probe the GRB emission process in the context of the synchrotron shock model. We show this here for the comparison with the SP1 results. The distributions of ΔS of the BAND and SBPL agree well, and are also consistent with the distribution obtained by Preece et al. (2002).

In terms of comparisons between the time-integrated and time-resolved spectral parameters, the most obvious difference is seen in the low-energy index distributions. The indices of time-integrated spectra are found to be softer than the time-resolved ones, except the PWRL case. Peak energies, E_{peak} , also tend to be slightly softer in the time-integrated spectra, especially when fitted with the COMP model. The differences are due to the fact that α and E_{peak} are very often observed to strongly evolve during a burst (e.g., Ford et al. 1995; Liang & Kargatis 1996; Band 1997; Crider et al. 1997; Ryde 1999; Crider et al. 1999). No significant difference in high-energy index distributions is seen.

5.2. Model Comparison within Each Spectrum

Since we have fitted the four models to all spectra, it is possible to statistically compare the models and determine the best-fit model to each individual spectrum. The comparison is, however, not straightforward because each model provides a different dof. A model that consists of a lower number of parameters is always preferred statistically over more complex models for the same χ^2 . However, the data may require an extra parameter for a better fit, in which case it should result in a significant improvement in χ^2 when the extra parameter is fitted. Therefore, we look at the χ^2 improvements in adding N parameters ($\Delta\text{dof} = N$), starting from the simplest model (i.e., PWRL) to determine the best-fit models.

The four models employed, namely PWRL, COMP, BAND, and SBPL, consist of 2, 3, 4, and 5 parameters, respectively. For each spectrum, we take the χ^2 of the PWRL fit as a reference. We first compare the PWRL fit χ^2 to the COMP fit χ^2 for $\Delta\text{dof} = 1$, and find the confidence level in χ^2 improvement. If the confidence level is greater than 99.9%, the COMP fit is significantly better than the PWRL fit; whereas, for confidence levels between 80.0 – 99.9%, we cannot statistically determine the better model between the two. The best-fit model in such a case is classified as PWRL/COMP. A confidence level lower than 80.0% suggests that the PWRL is preferred. Likewise, comparisons were made for all possible combinations of four models, with corresponding Δdof . The confidence intervals of 99.9%

and 80.0% were used for all comparisons involving PWRL, while 99.9% and 68.3% were used for the comparisons among the other models. These threshold values for the confidence intervals were decided based upon the simulation results described in full detail in §4. In the simulation, we fitted a simulated spectrum of a particular model by the other models and examined the degree of improvement in each fitting.

In most cases, the χ^2 probability was an adequate measure of the best fit determination; however, we found some cases where the best-fit model found by χ^2 probability was actually not better than the other models in terms of parameter constraints. Therefore, in addition to the χ^2 probabilities, the spectral parameters were also checked, requiring reasonable constraints on the additional parameter(s). If the best-fit model parameters are not constrained, the next statistically best-fit model with more constrained parameters was preferred. Finally, in case a preferred model could not be determined solely by changes in χ^2 , such as the PWRL/COMP case above, again their parameters were compared and a model with more constrained parameter set was designated as the best-fit model. The results of the best-fit model determination are shown in Table 8. It is seen that for many spectra, the COMP, BAND, and SBPL models all resulted in comparably good fits (C/B/S case in the Table 8). In most of these cases, the additional parameters were still well constrained, and the more complex models were meaningful. Consequently, the SBPL fits were selected as the best-fit models, despite the complexity of the model, in many of the C/B/S case. To illustrate the goodness of fits of each model, a count spectrum of one C/B/S burst with all four model counts is plotted in Figure 19. Moreover, for the time-resolved spectra, in almost 30% of the cases, the COMP and BAND fits were both found to be acceptable (i.e., C/B). For these spectra, the more complex BAND model was able to provide adequate parameter constraints, similar to the SBPL model in the C/B/S case above. In these cases, low-energy indices from all models were usually found in agreement within 1σ uncertainties (if α_{eff} is used). We also find that COMP tends to be preferable in fitting time-resolved spectra, because of the existence of more spectra without high-energy component, as well as the lower S/N in each spectrum compared with the time-integrated spectra. In addition, those best-fit by PWRL ($\sim 5\%$ of all spectra) were indeed among the dimmer, low S/N spectra. In the case of SBPL fit spectra, many spectra provided smaller break scales (i.e., sharper breaks).

Henceforth, we refer to this set of models as the “BEST” models, consisting of PWRL, COMP, BAND, and SBPL, each with numbers presented in the **TOTAL** row of Table 8. A collection of parameters obtained with the BEST models, with the use of α_{eff} and calculated E_{peak} and E_{b} , can be thought as a well-constrained, model-unbiased set of parameters best describing each spectrum in our sample. The time-integrated spectral fit results obtained with the BEST models are presented in Table 9, for each burst. Additionally, we show

the spectral parameter distributions of the BEST models in Figures 20 – 23, for both the time-integrated and time-resolved cases. In these figures, the distributions of each parameter of the BEST model and the contribution of each model that consists the BEST model are shown. Also, the median values and the dispersion of these distributions are summarized in Table 10.

We find the BAND model tends to fit spectra with harder low-energy indices, and especially in the time-resolved case, the COMP model seems to fit those with much softer indices. The spectra with positive low-energy indices are dominated by the BAND model fits. Most of the time-resolved COMP spectra with low-energy indices less than -1.5 were found to have low $E_{\text{peak}} \lesssim 300$ keV. The value of low-energy index -1.5 corresponds to the fast-cooling case of the synchrotron emission spectrum (Ghisellini & Celotti 1999). Out of the 8459 time-resolved spectra, 407 spectra resulted in the low-energy indices above the synchrotron limit of $-2/3$ (Katz 1994; Preece et al. 1998b) by more than 3σ . Meanwhile, for the high-energy spectral index distribution of time-resolved spectra, it seems those with harder high-energy indices are better fit by the SBPL model, while those with softer indices are better fit by the BAND model. We also find that the majority of SBPL with high-energy indices larger than -2.0 have small differences in low-energy and high-energy spectral indices ($\Delta S < 1$).

In the distributions of E_{peak} and break energy, we observe no secondary populations at energy below 100 keV, which was previously indicated by the break energy distribution of time-resolved spectra in SP1. The distributions of E_{peak} and break energy are different mainly due to the contribution of $E_{\text{peak}} \gtrsim 1$ MeV that is dominated by COMP spectra. These represent very hard spectra with the actual E_{peak} values lying very close to or higher than the upper energy bound of our datasets ($\gtrsim 1$ MeV). For such spectra, BAND or SBPL do not provide well-constrained high-energy spectral indices, and PWRL does not accommodate well the curvature of the spectra; therefore, the COMP fits were preferred. The ΔS distributions in Figures 22 and 23 (left panels) show that the SBPL spectra generally have much smaller changes in the indices. Most of those spectra with small differences in indices ΔS , have sharp breaks ($\Lambda \leq 0.1$), and more than a half of them have high-energy indices > -2.0 , indicating the existence of another break energy at higher energy. Finally, from the photon flux plots (right panels in Figures 22 and 23), it is also found that the simpler models (PWRL and COMP) are best fitted to weaker spectra, compared with more complex models (BAND and SBPL), as expected.

Using the set of BEST models determined for each time-resolved spectrum, we can also examine which parts of the burst are well fit by which models. This in turn reveals the evolution of spectral shapes within bursts. In Figures 24 and 25, we present the BEST models

as a function of time for two example bursts that exhibit the hard-to-soft and the “tracking” behaviors. Both behaviors are defined by E_{peak} and/or low-energy index evolution, which are commonly observed in GRBs (Ford et al. 1995; Crider et al. 1997). The evolution of the low-energy index and E_{peak} are also shown along with the BEST model histories. In the hard-to-soft burst (Figure 24), the first two-thirds is best fit by BAND, SBPL, or the COMP with high E_{peak} . The softer tail spectra of the burst are well fit by either PWRL with index less than -2 (indicating $E_{\text{peak}} \lesssim 30$ keV) or COMP with low E_{peak} . The last time interval of this burst was best fit by SBPL with $E_b = 177 \pm 55$ keV, but with $\lambda_1 > \lambda_2$ (i.e., concave-up shape), due to a few sigma excess counts in one energy channel at ~ 440 keV. On the other hand, in the tracking burst (Figure 25), the rise and fall of each peak are well fit by the low- E_{peak} COMP or PWRL.

5.3. Time-Integrated and Time-Resolved Spectra

For the comparison between the time-integrated and the time-resolved spectral parameters of the BEST models, we plot the total distributions of time-integrated and resolved parameters in Figure 26. These are the total distributions presented in Figures 20 and 21, but are now plotted on top of each other. Also the median values of each parameter are summarized in Table 11, along with the dispersion of the distributions. In order to determine if the distributions of the time-integrated and time-resolved spectral parameters are consistent, we employed the Kolmogorov-Smirnov (K-S) test (Press et al. 1992). The K-S test determines the parameter D_{KS} , which measures the maximum difference in the cumulative probability distributions over parameter space, and the significance probability P_{KS} for the value of D_{KS} . The null hypothesis is that the two datasets are drawn from the same parent distributions; therefore, a small P_{KS} rejects the hypothesis and indicates that the datasets are likely to be different. Determined by the K-S statistics, we find a significant difference in the low-energy spectral index distributions of time-integrated and time-resolved spectra, with P_{KS} of 10^{-16} ($D_{\text{KS}} = 0.23$). Also, a less significant difference was found between the E_{peak} distributions with P_{KS} of 8×10^{-3} ($D_{\text{KS}} = 0.10$). The distributions of the high-energy index and the break energy were consistent. This is in agreement with what we observed in the parameter distributions of individual model fits earlier (§5.1; Figures 9 – 17 and Table 7), and is, again, due to the spectral evolution within each burst.

We also compare the time-integrated and time-resolved distributions of SBPL break scales Λ and ΔS in Figure 27. It can be seen from the break scale comparison that the time-integrated SBPL spectra are smoother (larger break scales) than the time-resolved ones. This is naturally expected because the integrated spectra are summations of resolved spectra

with possibly various E_b values, and therefore, any sharp break features may be smeared over. For the same reason, the tendency of smaller ΔS observed in integrated spectra is expected as well.

It has been a common practice to fit the same broken-power law model (BAND in particular) to both time-integrated and time-resolved spectra. The model usually yields sufficiently good fits to both types of spectra; however, if the time-integrated spectrum consists of a set of broken-power law spectra with evolving break energy and indices, it is possible that the time-integrated spectra deviates from a broken-power law shape. Often, we do observe some indication of such deviations in the residual patterns obtained from time-integrated spectral fits to broken-power law models. To probe this, we explored how each time-resolved spectrum contributes to the time-integrated spectrum. The time-integrated spectra are usually considered as “average” spectra; however, averaging (whether error/intensity-weighted or not) the best-fit spectral parameters from each time-resolved spectrum does not yield the best-fit time-integrated spectral parameters. This is because the time-integrated spectra are averaged over count space rather than parameter space. Consequently, if each of the fitted time-resolved spectral models are indeed accurately representing the observed spectral data, summing over the model photon counts should reveal more accurate time-integrated photon spectrum.

Therefore, for each of 333 bursts (excluding 17 GRBs with single spectra), we obtained the time-integrated photon flux by summing the BEST model photon counts in the time-resolved spectra and dividing by their total durations;

$$\bar{\mathcal{F}}_{fluence}(E) = \frac{\sum_i f_i(E) \Delta t_i}{\sum_i \Delta t_i}. \quad (5)$$

Here, $f_i(E)$ is the BEST model photon flux of each time-resolved spectrum as a function of photon energy, and Δt_i is the accumulation time of each spectrum. The initial visual comparisons of $\bar{\mathcal{F}}_{fluence}$ plotted over the best-fit time-integrated spectral models suggested that they agree remarkably well for most of the GRBs in our sample. For quantitative comparisons of $\bar{\mathcal{F}}_{fluence}$ to the actual BEST model photon flux, we employed the χ^2 statistic (Press et al. 1992):

$$\chi_f^2 = \sum_{j=1}^N \frac{(\bar{\mathcal{F}}_j - \mathcal{F}_j)^2}{\sigma_j^2}, \quad (6)$$

where N is a number of energy bins, $\bar{\mathcal{F}}_j$ denotes $\bar{\mathcal{F}}_{fluence}$ per energy bin, \mathcal{F}_j is the actual time-integrated BEST model photon flux per energy bin, and σ_j^2 is the variance associated with \mathcal{F}_j obtained from the fits. For each burst, the χ_f^2 statistics and the corresponding significance probability, $P_{\chi_f^2}$, were determined (for N dof). Based on the statistic, 29% of 333 bursts

were rejected at 99% confidence level (i.e., $P_{\chi_f^2} < 1\%$) due to large χ^2 , and therefore, $\bar{\mathcal{F}}$ was different from \mathcal{F} . An example of such bursts is shown in Figure 28. We found that these bursts with very small $P_{\chi_f^2}$ values were of the brightest of the burst sample in terms of peak photon flux (Figure 29). Many of these bursts resulted in large χ_f^2 because the brightest spectrum within the burst tends to dominate in the summation process. This caused $\bar{\mathcal{F}}$ to consistently have much larger flux than the BEST model photon flux, as seen in Figure 28. The time-integrated spectral fits for most of these bursts also resulted in statistically poor spectral fits, with χ^2 goodness of fit worse than 3σ , even with the BEST models. In very bright bursts, the contribution of systematic uncertainties in the data is generally expected to be more evident (see Figure 1). As a result, the best-fit photon models may not represent the actual spectral shapes for these bursts. We also found that the majority of the bursts for which MER data were used fall into the group of small $P_{\chi_f^2}$. This is likely because there are more systematic uncertainties present in the multiple-detector MER data than the single-detector HERB or CONT data. In addition, the MER bursts in this group tend to consist of a larger number of spectra. This is because the MER data type was used when the corresponding HERB data were incomplete, which occurs frequently in the case of very bright bursts.

Furthermore, among the small- $P_{\chi_f^2}$ group, there are some bursts where the constructed photon flux $\bar{\mathcal{F}}$ seems to follow the actual time-integrated photon data points (deconvolved with BEST models) very well. One such example is shown in the Figure 30, for GRB 980306 (BATSE Trigger number 6630). Although there seems to be a slight offset in amplitude, it is remarkable that the shape of constructed photon flux ($\bar{\mathcal{F}}$; dashed line) traces the actual deconvolved data points of the time-integrated spectrum. The time-integrated spectral fit for this burst is still acceptable ($\chi^2/\text{dof} = 159.6/110$; see Table 9); however, the deviations of the real spectral shape from a smoothly-broken power-law model are evident.

From these, we infer that the time-integrated spectrum can be constructed by summing over the photon model counts of each time-resolved spectra within the burst (Equation 5), provided that the BEST model in each time-resolved spectrum is an accurate representation of the observed spectral shape. The actual time-integrated spectrum may not be as simple as the BEST models fit to the spectrum, due to spectral evolution. The bursts with peak photon flux larger than $\sim 30 \text{ photons s}^{-1} \text{ cm}^{-2}$ will likely suffer from large systematic uncertainties, with the results that the constructed spectrum does not represent the actual spectral shape, or has a shape that differs greatly from the best-fit model. Therefore, the fitted spectral parameters of the time-integrated spectra may only represent the best parameter possibly fit by our simple models that are limited in their spectral shapes. The spectral parameter distributions should be interpreted with this in mind. This may also be applicable to the time-resolved spectra given that the cooling timescales (both radiative and dynamical) can

be much shorter than the integration times of each spectrum.

5.4. Correlations Among Spectral Parameters

Some empirical correlations among GRB spectral parameters, such as between E_{peak} and low-energy index, have previously been reported with smaller samples (e.g., Crider et al. 1997; Lloyd-Ronning & Petrosian 2002). The correlations were found either within individual bursts or for a collection of time-resolved parameters. From inspection of scatter plots of the BEST parameters, we found no indication of strong global correlations among the time-integrated spectral parameters. On the other hand, among the time-resolved spectral parameters, broad positive trends between E_{peak} –low-energy index, E_{b} –low-energy index, and E_{peak} –high-energy index, were visible in the scatter plots. To probe the existence of correlations among the spectral parameters derived from our sample, we calculated the Spearman rank-order correlation coefficients, r_s , and the associated significance probabilities, P_{rs} (Press et al. 1992), for several combinations of spectral parameters of the BEST models. The null hypothesis is that no correlation exists; therefore, a small P_{rs} indicates a significant correlation.

To eliminate the possible effects of a dispersion of E_{peak} and E_{b} due to the cosmological redshift (z) that varies from burst to burst, it is best to look for parameter correlations within individual bursts. For each burst with a sufficient number of data points ($N \geq 10$) in our sample, we examined the correlations between combinations of low-energy and high-energy indices, E_{peak} , and E_{b} , by determining r_s and P_{rs} . We use the BEST model parameters of each time-resolved spectrum within bursts, and also, for simplicity, we denote the low-energy and high-energy indices of the BEST model as α and β respectively, in this section. The number of parameter pairs (N) in each burst was less than or equal to the number of time-resolved spectra; however, this varied according to which parameter pair was considered since we used the BEST model parameters and certain parameters are not obtainable for certain resolved spectra. For example, within the same burst, it is possible that for an $E_{\text{peak}} - \alpha$ correlation, $N = 20$ pairs were available, but for $E_{\text{peak}} - \beta$ only $N = 15$ were available. For most of the cases, N was $\gtrsim 80\%$ of the number of spectra and was always more than 10. We note that the P_{rs} values take into account the actual N in the calculation that determines each correlation significance. The resulting numbers of bursts considered for each correlation were summarized in Table 12 along with percentages of bursts with significant correlations between each pair of parameters. We considered the correlation significant if $P_{rs} < 10^{-3}$ ($> 3\sigma$). The coefficient r_s and the associated P_{rs} of the bursts that showed significant correlations in at least one of the parameter pairs are listed in Table 13.

To illustrate some of the strong correlations, we show example scatter plots of each type of parameter pairs in Figure 31. The strongest positive correlation is found between E_{peak} and α , in 26% of the bursts. In many cases, the chance probabilities of these correlations are extremely low. Positive correlations between $E_b - \alpha$ are also evident, although only in half of the fraction of the E_{peak} cases. We note that the results were not significantly altered when unadjusted low-energy index (regular α for BAND and COMP) were used, instead of α_{eff} that we use here for the BEST model parameters. The E_b value is equal to the E_{peak} value only when a spectrum has a sharp break. Otherwise, a break scale or curvature determines the relation between them. Therefore, the same degree of correlation is not expected for E_b and E_{peak} . On the contrary, the $E_{\text{peak}} - \beta$, $E_b - \beta$ and $\alpha - \beta$ correlations are found in a much lower fraction of the bursts than the E_b/E_{peak} and α cases, and are mostly negative. It must be noted, however, that the uncertainty associated with each parameter is not taken into account in determining the rank-order correlation, and β is usually associated with relatively larger uncertainties than the other parameters. This can be seen in the scatter plots in Figure 31. The measurement uncertainties may have masked an actual correlation. We have also found significant positive correlations between E_{peak} and the time-resolved photon flux in 28% of GRBs, and between α and the photon flux (42%), indicating the tracking behavior. About 18% of GRBs with the E_{peak} –flux correlation also belong to the group with the α –flux correlation, and therefore show strong tracking behavior in both E_{peak} and α . Some of these also display overall hard-to-soft behavior, indicated by strong correlations of the parameters with time.

These correlations among the spectral parameters should be accounted for within an emission model. The observed correlations between fitted model parameters indicate possible correlations between physical parameters at the GRB emitting region. For example, according to the synchrotron shock model, E_{peak} should be related to the magnetic field strength and the minimum energy of accelerated electrons (Tavani 1996), whereas low-energy index may depend on the electron pitch-angle distribution or density of the absorbing medium (Lloyd-Ronning & Petrosian 2002). On the other hand, in the jitter radiation model, E_{peak} varies with the ratio between deflection and beaming angles of an emitting electron, and low-energy index depends on the ratio of strengths of large-scale and small-scale magnetic fields existing at the shock (Medvedev 2000).

Finally, global correlations between the time-integrated E_{peak} , α , β , and energy or photon flux/fluence values (including peak photon flux) were also investigated. We found only one relatively significant correlation, between E_{peak} and total energy fluence, with $r_s = 0.20$ and $P_{rs} = 2.5 \times 10^{-4}$. One of the most highly cited empirical correlations is the $E_{\text{peak}} - E_{\text{iso}}$ correlation found by Amati et al. (2002). The Amati relation is $E_{\text{p},0} \propto E_{\text{iso}}^{0.5}$, where $E_{\text{p},0}$ is the peak energy in the source rest frame, namely, $(1+z)E_{\text{peak}}$, and E_{iso} is an isotropic equivalent

total emitted energy for a given distance. The relation was found by using a dozen GRBs observed with *BeppoSAX* with known redshift values z . If true, such a correlation can provide strong constraints on the GRB emission mechanism and the fundamental nature of GRBs. It has recently been shown, however, that the Amati relation suffers from a strong selection effect and is greatly inconsistent with a larger set of GRB data obtained with BATSE (Nakar & Piran 2005a; Band & Preece 2005). This was indicated by a limit in observed E_{peak} and energy fluence values (and therefore independent of redshift) that is implied by the Amati relation. Responding to the results, Ghirlanda et al. (2005) argued that taking into account the intrinsic scatter of the relation, the BATSE bursts may still be consistent. This claim, however, has also been challenged (Nakar & Piran 2005b). To show how E_{peak} and energy fluence values in our sample are correlated, we plot E_{peak} vs. total energy fluence in Figure 32. On the scatter plot, we also show the limit on the Amati relation and the maximum 3σ limit derived by Ghirlanda et al. (2005). The bursts below these lines are inconsistent with the relation. Note that the GRB sample used to test the consistency in Band & Preece (2005) includes many more dimmer bursts than bursts in our sample. Despite the fact that our sample only consists of bright GRBs, we confirm that most of our bursts are significantly inconsistent with the Amati limit. Even for the 3σ Ghirlanda limit, we observe more outliers than they found in their work. Our well-constrained parameters strongly indicate that the Amati relation is only valid for a small sample of selected bursts.

5.5. BETA Model Fit Results

Since the BETA model is a variation of the BAND model, we did not include the BETA model in obtaining the overall model statistics above. The purpose of this model is to test whether the high-energy power-law index, β , stays constant for the entire duration of a burst, which is expected in the simplest shock acceleration and the GRB emission scenario. Earlier work by Preece et al. (1998a) found that 34% of 122 GRBs investigated were inconsistent with the constant- β hypothesis. Note that most GRBs in their sample overlaps with the sample presented herein. In Preece et al. (1998a), the β values that were used as the constant values were the error-weighted average of β obtained from fits to each of time-resolved spectra within bursts. These values are different from those obtained by the time-integrated fits, due to the following reasons. Spectra with higher S/N usually have smaller error associated with their fits. Therefore, they have more weight in determining the error-weighted average of β . These spectra, however, may have much shorter integration times, because of the binning by S/N as well as the characteristics of HERB data (also used in Preece et al. (1998a)). Despite their large photon flux values, they may not provide large photon fluence counts due to the short time intervals. As discussed in the earlier section

(§5.3), the time-integrated spectrum can be obtained by summing over the photon counts (not count rate) rather than error-weighted averaging of parameters. This resulted in the values used to test the constancy of the index in Preece et al. (1998a) to be higher than those obtained from fits to the time-integrated spectra, which are used in this work.

In order to have sufficient time samples to study the time evolution of β , as well as to be consistent with the Preece et al. (1998a) analysis, our sample was limited to bursts that consist of at least eight spectra. Additionally, there were some cases in which the time-integrated β values were less than -5 by more than 1σ , and thus lacking the high-energy power-law component (i.e., COMP-like spectra). In these cases, fitting the time-resolved spectra with these small values is not meaningful for our purpose here, and therefore, those bursts were also excluded. The remaining total number of bursts in the sample was 210.

To determine whether β is consistent with being constant throughout a burst, we checked the resulting χ^2 of the BETA model fit to each time-resolved spectrum and calculated the corresponding goodness of fit. The maximum goodness of fit allowed was set to an equivalent chance probability of one per number-of-spectra in each burst in order to take into account the number of trials in each case: in other words, one spectrum in each burst was statistically expected not to give an acceptable BETA fit. Consequently, the goodness-of-fit allowed was always at least 87.5% (corresponding to a minimum number of spectra of eight). Then, if all but one spectrum within a burst resulted in χ^2 probabilities less than the given maximum goodness-of-fit level, the burst was considered to be consistent with having a constant β . We call these bursts “constant- β GRBs” and the others “varying- β GRBs” hereafter.

We found that nearly a half of the sample (108 out of 210 GRBs) are varying- β GRBs. The result differs from the result of 34% that was obtained by Preece et al. (1998a), who searched for a correlation between β and time. The time-integrated spectra of the varying- β GRBs are more likely to be best fit with the COMP model, which has a high-energy cutoff. In Figure 33, the distributions of the BAND fit β values (i.e., fit with β as a free parameter) for the time-resolved spectra within the varying- β and constant- β GRBs are compared. We also show the BAND β evolution of an example varying- β GRB in Figure 34. A larger fraction of the varying- β spectra are fitted by smaller β values than the constant- β spectra. It may be the case that the varying- β GRBs contain high-energy cutoff spectra where β is essentially less than -5 , which in turn fails the BETA fits with $\beta > -5$. The median value of the time-resolved BAND β for the varying- β and constant- β spectra are $-2.51^{+0.32}_{-0.52}$ and $-2.37^{+0.30}_{-0.49}$, respectively. No differences in the E_{peak} and the α distributions are evident between the constant and varying β bursts. For the constant- β GRBs, the median value for the BETA high-energy index (the value that were used as the constant value) was $-2.39^{+0.19}_{-0.34}$.

5.6. Short GRBs

Our sample includes 17 short bursts ($T_{90} \lesssim 2$ s), which are listed in Table 14. Short GRBs were previously shown to be spectrally harder than long bursts in terms of the spectral hardness ratio (Dezalay et al. 1992; Kouveliotou et al. 1993) and spectral parameters (Paciesas et al. 2003). The parameter comparison of short GRBs and long GRBs in our sample is summarized in Table 15. There is no significant difference between the spectral parameters of the short bursts and the rest (long bursts), in both time-integrated and time-resolved spectra. This may be expected since our sample is limited to the brightest bursts, whereas the sample used in Paciesas et al. (2003) did not have such selection effects. Mallozzi et al. (1995) found that brighter bursts tend to be harder, and our sample here belongs to the brightest of the five groups defined by Mallozzi et al. (1995). Besides, we used mostly HERB data for the short bursts, which may be missing a substantial portion of the emission of the short bursts due to the accumulation start time of the HERB data (≥ 64 ms after burst onset time). Three short bursts, GRBs 920414, 980228, and 000326 (BATSE trigger numbers 1553, 6617, and 8053), were bright enough to provide three to five time-resolved spectra, and they all clearly exhibited spectral evolution. As an example, the spectral evolution of GRB 000326 is shown in Figure 35. In two cases (GRBs 920414 and 980228), the spectra evolved hard to soft in all low-energy & high-energy indices and E_{peak} , whereas in the other case (GRB 000326; Figure 35) we observed tracking behavior in E_{peak} while both indices monotonically decayed. If short GRBs generally evolve hard to soft, the HERB data of short bursts will lack a coverage of the hardest portions of the bursts, biasing the spectral parameters of the short GRBs in our sample to softer values.

6. Summary and Discussion

We have analyzed the large sample of bright BATSE GRBs with high-energy resolution and high-time resolution, using five different photon models. For both time-integrated and time-resolved spectra, we have presented the distributions of each spectral parameter; low-energy and high-energy power law indices, E_{peak} , and break energy, determined with the best-fit model to each spectrum, with good statistics.

We confirmed, using a much larger sample, that the most common value for the low-energy index is ~ -1 (SP1; Ghirlanda et al. 2002). The overall distribution of this parameter shows no clustering or distinct features at the values expected from various emission models, such as $-2/3$ for synchrotron (Katz 1994; Tavani 1996), 0 for jitter radiation (Medvedev 2000), or $-3/2$ for cooling synchrotron (Ghisellini & Celotti 1999). About 5% of the time-

resolved spectra are found to have the low-energy indices significantly above the synchrotron limit of $-2/3$. The median value for the high-energy indices is found to be ~ -2.3 and the parameter can be constrained only if the value is larger than ~ -5 with the BATSE LAD data. The dispersions in the low-energy and high-energy index distributions were found to be comparable, $\sigma \sim 0.25$. For the first time, E_{peak} and break energy, at which the two power laws are joined, have been made distinct. We presented the E_{peak} and break energy distributions separately, and found that E_{peak} tends to be harder than the break energy. This is due to the existence of curvature in spectra. E_{peak} becomes break energy only in a sharply-broken power-law spectrum. The E_{peak} distribution peaks at ~ 300 keV while that of the break energy peaks at ~ 200 keV, both with very narrow width of $\lesssim 100$ keV. We now know that there exist fainter, softer GRBs with lower E_{peak} that BATSE would not have detected (e.g., Sakamoto et al. 2005); therefore, the actual observed E_{peak} distribution of GRBs should extend to a lower energy. The narrowness of the distributions, if real, implies an extremely narrow intrinsic distribution of these parameters, and poses a challenge for the internal shock model of GRB prompt emission (Zhang & Mészáros 2002). There are small populations of GRBs (7% of time-resolved spectra) that have high-energy indices above -2 by more than 3σ . This indicates that there may be a small tail population of spectra with $E_{\text{peak}} \gtrsim 2$ MeV.

It must be noted that the time-resolved spectral analysis results obtained here may be biased by the brighter (higher photon flux) portions of each burst because the HERB data type was designed to sample more frequently during the intense episodes. Since the E_{peak} values tend to be correlated with the photon flux in general (Mallozzi et al. 1995), the spectra with higher E_{peak} might be over-sampled whereas those with lower E_{peak} are likely to be under-sampled. This may partially explain the differences observed in the E_{peak} distributions of time-integrated and resolved spectra. Similarly, the low-energy indices also tend to correlate with E_{peak} ; therefore, the same type of bias may exist in the low-energy index distribution as well.

We have also explored time-integrated spectra by reconstructing them from the time-resolved spectra, and identified cases where the actual integrated spectra deviate from the simple broken power-law model, due to spectral evolution within the integration time. Therefore, fine time resolution data are crucial to more accurately represent the spectral shape using a relatively simple model. Significant correlations among parameters are also observed in some GRBs. The most evident positive correlation is found between E_{peak} and the low-energy index, in 26% of GRBs considered. Since our parameter sets are well constrained and unbiased by photon models, the correlations found are more likely to reflect intrinsic properties of GRBs, rather than the instrumental or other systematic effects, as has been pointed out (e.g., Lloyd-Ronning & Petrosian 2002). In addition, a mild global correlation

between E_{peak} and energy fluence in our sample was found. The significance of the correlation is much lower than what was found previously by Lloyd, Petrosian & Mallozzi (2000), with a larger sample including many more dimmer bursts.

In its simplest picture, the synchrotron shock model assumes that the electrons are accelerated by the first-order Fermi mechanism to a power-law distribution ($N(\gamma) \propto \gamma^{-p}$), which does not evolve in time. The electron index p is then related to β either as $\beta = -(p + 2)/2$ in case of the fast-cooling synchrotron spectrum, or as $\beta = -(p + 1)/2$ in case of non-cooling synchrotron (Sari et al. 1998). Our constant $\beta \sim -2.4$ then indicates $p \sim 2.8$ or ~ 3.8 , respectively. The ultra-relativistic Fermi-type acceleration results in $p = 2.2 - 2.3$ (Gallant 2002); therefore, if indeed the electron distribution remain unchanged within a GRB, the fast radiative cooling of the electrons are more likely to be in effect at the source, as has been suggested (Preece et al. 2002; Lloyd-Ronning & Petrosian 2002). However, we found, using the BETA model, that 51% of 210 GRBs considered are inconsistent with the constant- β hypothesis. Finally, we found no significant difference between the spectral parameters of 17 short bursts and long bursts in our sample, which is possibly due to the instrumental effects. In addition, spectral evolutions, hard-to-soft or tracking, were found in three of the short bursts with enough number of time-resolved spectra. These evolution patterns are often observed in individual peaks of long GRBs.

It is important to note that the analysis presented here only includes bright GRBs, which tend to be spectrally harder in general than dim GRBs. The global correlations we studied here between the spectral hardness and the burst intensity (flux and fluence), would probably change somewhat, if dimmer bursts were included. Another sample selection bias exists against very short GRBs, due to the fact that we used the peak photon flux in 256 ms to determine the brightness of the bursts. Many bright short GRBs have duration much shorter than 256 ms, in which case the photon flux with 256-ms integration time may smear out the brightness. The short GRBs included in our analysis, therefore, have duration $\gtrsim 256$ ms, and only comprises less than 5% of our sample of 350 bursts. This is much less than the fraction of short GRBs in the entire BATSE GRB sample ($\sim 19\%$).

The GRB spectral database obtained in this work is derived from the most sensitive and largest database to date. Therefore, these results set a standard for spectral properties of GRB prompt emission with exceptional statistics. Our analysis results can provide reliable constraints for existing and future theoretical models of the particle acceleration and GRB emission mechanisms. The spectral database also allows for the spectral evolutions within each burst to be taken into consideration when constraining such models.

A. Derivation of the Smoothly Broken Power Law

The basic concept is that the power-law index changes smoothly from the low-energy index (λ_1) to high-energy index (λ_2). Since $\lambda_1 > \lambda_2$ in general, we assume the index change is described by a negative hyperbolic tangent function, namely $y = -C_1 \tanh(x) + C_2$, as plotted in Figure 36. C_1 and C_2 are positive constant.

Here, $y = d(\log f(E))/d(\log E)$, and it is evident from Figure 36 that $C_1 = \frac{\lambda_1 - \lambda_2}{2}$ and $C_2 = \frac{\lambda_1 + \lambda_2}{2}$. So we have

$$\frac{d(\log f)}{d(\log E)} = -\frac{\lambda_1 - \lambda_2}{2} \tanh(x) + \frac{\lambda_1 + \lambda_2}{2}, \quad (\text{A1})$$

where

$$x \equiv \frac{\log(E/E_b)}{\Lambda}.$$

x is defined so that $x = 0$ at a break energy E_b , and also the break scale, Λ , determines the width of the transition region from λ_1 to λ_2 .

To obtain the photon flux, $f(E)$, first integrate Equation A1 with respect to $\log E$, and we get

$$\begin{aligned} \log f(E) &= \int \left[\frac{\lambda_2 - \lambda_1}{2} \tanh(x) + \frac{\lambda_1 + \lambda_2}{2} \right] d(\log E) \\ &= \frac{\lambda_2 - \lambda_1}{2} \ln(\cosh(x)) \frac{d(\log E)}{dx} + \frac{\lambda_1 + \lambda_2}{2} \log E + \mathbb{C} \\ &= \frac{\lambda_2 - \lambda_1}{2} \ln \left[\cosh \frac{\log(E/E_b)}{\Lambda} \right] \Lambda + \frac{\lambda_1 + \lambda_2}{2} \log E + \mathbb{C}, \end{aligned}$$

where \mathbb{C} is the integration constant.

Therefore, the photon flux is

$$f(E) = 10^{\frac{\lambda_2 - \lambda_1}{2} \Lambda \ln \left[\cosh \frac{\log(E/E_b)}{\Lambda} \right]} E^{\frac{\lambda_1 + \lambda_2}{2}} \mathbb{C}'. \quad (\text{A2})$$

A boundary condition is that $f(E) = A$ when $E = E_{\text{piv}}$, where A is an amplitude of the photon flux determined at the pivot energy E_{piv} , so we find

$$\begin{aligned} f(E = E_{\text{piv}}) &= 10^{\frac{\lambda_2 - \lambda_1}{2} \Lambda \ln \left[\cosh \frac{\log(E_{\text{piv}}/E_b)}{\Lambda} \right]} E_{\text{piv}}^{\frac{\lambda_1 + \lambda_2}{2}} \mathbb{C}' = A \\ \rightarrow \mathbb{C}' &= A 10^{-\frac{\lambda_2 - \lambda_1}{2} \Lambda \ln \left[\cosh \frac{\log(E_{\text{piv}}/E_b)}{\Lambda} \right]} E_{\text{piv}}^{-\frac{\lambda_1 + \lambda_2}{2}}. \end{aligned}$$

Then the Equation A2 becomes

$$f(E) = A 10^{\frac{\lambda_2 - \lambda_1}{2} \Lambda} \left[\ln \left(\cosh \frac{\log(E/E_b)}{\Lambda} \right) - \ln \left(\cosh \frac{\log(E_{\text{piv}}/E_b)}{\Lambda} \right) \right] \left(\frac{E}{E_{\text{piv}}} \right)^{\frac{\lambda_1 + \lambda_2}{2}} \quad (\text{A3})$$

Rewriting this, we obtain the smoothly broken power law model:

$$f_{\text{SBPL}}(E) = A \left(\frac{E}{E_{\text{piv}}} \right)^b 10^{(a - a_{\text{piv}})}, \quad (\text{A4})$$

where

$$\begin{aligned} a &= m\Lambda \ln \left(\frac{e^q + e^{-q}}{2} \right), & a_{\text{piv}} &= m\Lambda \ln \left(\frac{e^{q_{\text{piv}}} + e^{-q_{\text{piv}}}}{2} \right), \\ q &= \frac{\log(E/E_b)}{\Lambda}, & q_{\text{piv}} &= \frac{\log(E_{\text{piv}}/E_b)}{\Lambda}, \\ m &= \frac{\lambda_2 - \lambda_1}{2}, \text{ and } & b &= \frac{\lambda_1 + \lambda_2}{2}. \end{aligned}$$

B. SBPL Model E_{peak}

The SBPL model is parameterized with E_b , which is the energy at which the low-energy power law joins with the high-energy power law; this is clearly different from the E_{peak} parameters of the BAND and COMP models. Therefore, E_b and E_{peak} are not directly comparable with each other. However, it is easy to derive “ E_{peak} ” (i.e., the peak in νF_ν spectrum) for a spectrum fitted with SBPL, which, in turn, can be compared to the E_{peak} of the other models directly.

B.1. Finding E_{peak}

Starting from Equation 4, the νF_ν flux can be written as

$$\nu F_\nu \equiv E^2 f(E) = \frac{A}{E_{\text{piv}}^b} E^{(b+2)} 10^{(a - a_{\text{piv}})},$$

where

$$\begin{aligned} a &= m\Lambda \ln \left(\frac{e^q + e^{-q}}{2} \right), & a_{\text{piv}} &= m\Lambda \ln \left(\frac{e^{q_{\text{piv}}} + e^{-q_{\text{piv}}}}{2} \right), \\ q &= \frac{\log(E/E_b)}{\Lambda}, & q_{\text{piv}} &= \frac{\log(E_{\text{piv}}/E_b)}{\Lambda}, \\ m &= \frac{\lambda_2 - \lambda_1}{2}, \text{ and } & b &= \frac{\lambda_1 + \lambda_2}{2}. \end{aligned}$$

To find the peak in the νF_ν spectrum, we need

$$\left. \frac{d}{dE}(\nu F_\nu) \right|_{E_{\text{peak}}} = 0,$$

and we find

$$\frac{d}{dE}(\nu F_\nu) = \frac{A}{E_{\text{piv}}^b} E^{(b+1)} 10^{(a-a_{\text{piv}})} (b+2 + m \tanh(q)). \quad (\text{B1})$$

Set this equation to 0 at $E = E_{\text{peak}}$, and we obtain

$$\tanh(q) = \frac{-(b+2)}{m}. \quad (\text{B2})$$

But $q(E_{\text{peak}}) = \frac{\log(E_{\text{peak}}/E_b)}{\Lambda}$ so the equation becomes

$$\tanh\left(\frac{\log(E_{\text{peak}}/E_b)}{\Lambda}\right) = \frac{-(b+2)}{m}, \quad (\text{B3})$$

and solving this for E_{peak} , we obtain

$$E_{\text{peak}} = E_b \, 10^{\left[\Lambda \tanh^{-1}\left(\frac{\lambda_1 + \lambda_2 + 4}{\lambda_1 - \lambda_2}\right) \right]}. \quad (\text{B4})$$

We note here that since we must have $\left| \frac{\lambda_1 + \lambda_2 + 4}{\lambda_1 - \lambda_2} \right| < 1$, this is only valid for $\lambda_1 > -2$ and $\lambda_2 < -2$ in order for the νF_ν spectrum to have a peak within the spectral energy range.

B.2. Error Propagation ($\sigma_{E_{\text{peak}}}$)

In order to calculate the uncertainties associated with the derived E_{peak} values, the errors associated with each parameter involved have to be propagated correctly.

Generally, the variance of a function, y , of N parameters (x_1, x_2, \dots, x_N) can be found by:

$$\text{Var}(y) = \sum_{i=1}^N \left[\left(\frac{\partial y}{\partial x_i} \right)^2 \text{Var}(x_i) \right] + 2 \frac{\partial y}{\partial x_1} \frac{\partial y}{\partial x_2} \text{Cov}(x_1, x_2) + 2 \frac{\partial y}{\partial x_2} \frac{\partial y}{\partial x_3} \text{Cov}(x_2, x_3) + \dots, \quad (\text{B5})$$

where $\text{Cov}(x_j, x_k) = R_{jk} \sigma_{x_j} \sigma_{x_k}$ and R_{jk} is the correlation coefficient between x_j and x_k . Unfortunately, the covariance matrices for individual fits were not stored in the parameter files in our database here, and therefore, we could only estimate the uncertainties of the

derived E_{peak} by neglecting the cross terms in Equation B5. The general effect of excluding the terms may be tested by examining cross-correlations between each parameter involved.

For the SBPL E_{peak} , we have Equation B4 as a function of three fitted parameters, E_b , λ_1 , and λ_2 , with the uncertainties associated with each parameter, $\sigma_{E_b}, \sigma_{\lambda_1}, \sigma_{\lambda_2}$. First, to make the equation simpler, define

$$s \equiv \Lambda \tanh^{-1} u \quad \text{and} \quad u \equiv \frac{\lambda_1 + \lambda_2 + 4}{\lambda_1 - \lambda_2}, \quad (\text{B6})$$

and rewrite Equation B4 as

$$f(E_b, \lambda_1, \lambda_2) = E_{\text{peak}} = E_b 10^s.$$

Then, the variance of E_{peak} is

$$\sigma_{E_{\text{peak}}}^2 = \sigma_{E_b}^2 \left(\frac{\partial f}{\partial E_b} \right)^2 + \sigma_{\lambda_1}^2 \left(\frac{\partial f}{\partial \lambda_1} \right)^2 + \sigma_{\lambda_2}^2 \left(\frac{\partial f}{\partial \lambda_2} \right)^2, \quad (\text{B7})$$

considering only the uncorrelated terms of Equation B5.

Now, the derivatives are

$$\begin{aligned} \frac{\partial f}{\partial E_b} &= 10^s \\ \frac{\partial f}{\partial \lambda_1} &= E_b 10^s \ln 10 \frac{\Lambda}{(1+u)(\lambda_1 - \lambda_2)} \\ \frac{\partial f}{\partial \lambda_2} &= E_b 10^s \ln 10 \frac{\Lambda}{(1-u)(\lambda_1 - \lambda_2)}. \end{aligned}$$

Therefore, Equation B7 becomes

$$\sigma_{E_{\text{peak}}}^2 = \sigma_{E_b}^2 (10^s)^2 + \left(E_b 10^s \ln 10 \frac{\Lambda}{\lambda_1 - \lambda_2} \right)^2 \left(\frac{\sigma_{\lambda_1}^2}{(1+u)^2} + \frac{\sigma_{\lambda_2}^2}{(1-u)^2} \right),$$

and finally, the E_{peak} uncertainty is

$$\sigma_{E_{\text{peak}}} = 10^s \sqrt{\sigma_{E_b}^2 + \left(E_b \ln 10 \frac{\Lambda}{\lambda_1 - \lambda_2} \right)^2 \left(\frac{\sigma_{\lambda_1}^2}{(1+u)^2} + \frac{\sigma_{\lambda_2}^2}{(1-u)^2} \right)}, \quad (\text{B8})$$

where

$$s = \Lambda \tanh^{-1} u \quad \text{and} \quad u = \frac{\lambda_1 + \lambda_2 + 4}{\lambda_1 - \lambda_2}.$$

The covariance terms that were excluded are

$$2 \left[\text{Cov}(E_b, \lambda_1) \frac{\partial f}{\partial E_b} \frac{\partial f}{\partial \lambda_1} + \text{Cov}(E_b, \lambda_2) \frac{\partial f}{\partial E_b} \frac{\partial f}{\partial \lambda_2} + \text{Cov}(\lambda_1, \lambda_2) \frac{\partial f}{\partial \lambda_1} \frac{\partial f}{\partial \lambda_2} \right] \quad (\text{B9})$$

$$= \frac{2(10^{2x})E_b \ln 10\Lambda}{\lambda_1 - \lambda_2} \left[\frac{R_{E_b, \lambda_1} \sigma_{E_b} \sigma_{\lambda_1}}{1 + u} + \frac{R_{E_b, \lambda_2} \sigma_{E_b} \sigma_{\lambda_2}}{1 - u} + R_{\lambda_1, \lambda_2} \sigma_{\lambda_1} \sigma_{\lambda_2} \frac{E_b \ln 10\Lambda(2 + \lambda_2)}{(1 - u^2)(\lambda_1 - \lambda_2)} \right],$$

where s and u are defined above. To understand the overall consequence of disregarding the covariance terms, we investigated the cross-correlations between the parameters (i.e., E_b , λ_1 , and λ_2 , with $\Lambda = \text{fixed}$). This was done by using the results of 4-parameter SBPL fits to a set of simulated SBPL spectra with several different break scales described in §4.2. Although the correlation coefficients change slightly as a function of fixed Λ values, we found $E_b - \lambda_1$ and $E_b - \lambda_2$ are always strongly anti-correlated. The corresponding average correlation coefficients were $\langle R_{E_b, \lambda_1} \rangle \sim -0.8$ and $\langle R_{E_b, \lambda_2} \rangle \sim -0.9$. On the other hand, $\lambda_1 - \lambda_2$ was always positively correlated with $\langle R_{\lambda_1, \lambda_2} \rangle \sim 0.5$.

Using the real set of parameters in our analysis, along with the average correlation coefficients found from the simulation above, we found that the correlated terms (Equation B9) are almost always negative, as long as two of the correlation coefficients are negative. Therefore, it is likely that the errors calculated using Equation B7 is overestimated for many spectra.

C. BAND Model E_b

Although a break energy is not parameterized in the BAND model, the model has a broken power-law shape, and therefore, we could find a spectral break energy equivalent to the E_b of SBPL for a direct comparison. We stress again, as we did in §3.2.5, that this E_b is not the characteristic energy in Equation 2; $E_c = (\alpha - \beta)E_{\text{peak}}/(2 + \alpha)$, which is often called the *break energy* (e.g., SP1; Sakamoto et al. 2004) but is not the energy where the power law changes. Rather, the energy E_c corresponds to where the low-energy power law with an exponential cutoff ends and the pure high-energy power law starts; therefore, it is always greater than the E_b we are trying to find here.

C.1. Finding E_b

Since $E_b < E_c$ always, we only use the $E < E_c$ case in Equation 2. To find E_b , we consider the change in slope of logarithmic tangential lines from α to β , which is smooth

and continuous. We start by writing Equation 2 in logarithmic scale;

$$\log f(E) = \log A - 2\alpha + \alpha \log E - \frac{(2 + \alpha)E}{E_{\text{peak}}} \log e. \quad (\text{C1})$$

Then, the derivative with respect to $\log E$ is

$$\frac{d \log f(E)}{d \log E} = \alpha - \frac{(2 + \alpha)E}{E_{\text{peak}}}, \quad (\text{C2})$$

which is the equation for the slope as a function of E .

A break region can be defined as the energy range where the slope is between α and β . By definition of the model, the slope is equal to α when $E = 0$ and β when $E = E_c$, then the break region is from 0 to E_c in keV. However, since the fitted α value is the tangential slope at $E = 0$ and does not exactly represent the low-energy spectral shape, the actual slopes at energies $E > 0$ is always less than α due to the exponential term in the model. In order to take this into account, we use “effective” low-energy power law index, α_{eff} , described in Appendix D. This is essentially the slope (Equation C2) at a fixed energy of 25 keV. Accordingly, we use the α_{eff} in calculating the E_b , and the break region is from 25 keV to E_c .

The E_b then should be at the center of the break region, namely, the energy at which the slope value differs from both α_{eff} and β by the same amount, $(\alpha_{\text{eff}} - \beta)/2$. In other words, the slope at E_b must equal $(\alpha_{\text{eff}} + \beta)/2$. Since the slope is a linear function, this is just the center energy between 25 keV and E_c , and is

$$E_b = \frac{E_c - 25}{2} + 25 = \frac{\alpha - \beta}{2} \frac{E_{\text{peak}}}{2 + \alpha} + 12.5. \quad (\text{C3})$$

C.2. Error Propagation (σ_{E_b})

The general error propagation methodology was discussed in §B.2. For the same reason, we do not include the cross terms of Equation B5 in the error calculation here. The BAND E_b (Equation C3) is a function of three fitted parameters, E_{peak} , α , and β , with uncertainties, $\sigma_{E_{\text{peak}}}$, σ_α , and σ_β , respectively. The E_{peak} is noted as E_p in the following equations for simplicity. Let $f(E_p, \alpha, \beta) = E_b$, then the variance of E_b can be written as

$$\sigma_{E_b}^2 = \sigma_{E_p}^2 \left(\frac{\partial f}{\partial E_p} \right)^2 + \sigma_\alpha^2 \left(\frac{\partial f}{\partial \alpha} \right)^2 + \sigma_\beta^2 \left(\frac{\partial f}{\partial \beta} \right)^2, \quad (\text{C4})$$

without the covariance terms. The derivatives are

$$\begin{aligned}\frac{\partial f}{\partial E_p} &= \frac{\alpha - \beta}{2(2 + \alpha)} \\ \frac{\partial f}{\partial \alpha} &= \frac{E_p(2 + \beta)}{2(2 + \alpha)^2} \\ \frac{\partial f}{\partial \beta} &= -\frac{E_p}{2(2 + \alpha)}.\end{aligned}$$

Therefore, Equation C4 becomes

$$\sigma_{E_b}^2 = \sigma_{E_p}^2 \left(\frac{\alpha - \beta}{2(2 + \alpha)} \right)^2 + \sigma_\alpha^2 \left(\frac{E_p(2 + \beta)}{2(2 + \alpha)^2} \right)^2 + \sigma_\beta^2 \left(-\frac{E_p}{2(2 + \alpha)} \right)^2, \quad (C5)$$

and we find the uncertainty

$$\sigma_{E_b} = \frac{1}{2(2 + \alpha)} \sqrt{(\alpha - \beta)^2 \sigma_{E_p}^2 + E_p^2 \left(\left(\frac{2 + \beta}{2 + \alpha} \right)^2 \sigma_\alpha^2 + \sigma_\beta^2 \right)}. \quad (C6)$$

Similar to the SBPL E_{peak} case, the correlations between the parameters involved in Equation C3 (i.e., E_{peak} , α , and β) were investigated using the fits to the same set of the simulated SBPL spectra that was used to explore the SBPL parameter correlations in §B.2 for consistency, as well as the simulated BAND spectra. We found that both $E_{\text{peak}} - \alpha$ and $E_{\text{peak}} - \beta$ are always highly anti-correlated regardless of the E_{peak} values or the SBPL break scale, with correlation coefficients of $\langle R_{E_p, \alpha} \rangle \sim -0.9$ and $\langle R_{E_p, \beta} \rangle \sim -0.7$. The correlation between α and β tends to be weaker, though always positively correlated, with a correlation coefficient of $\langle R_{\alpha, \beta} \rangle \sim 0.5$.

The cross terms of $\sigma_{E_b}^2$ are

$$\begin{aligned}& 2 \left[\text{Cov}(E_p, \alpha) \frac{\partial f}{\partial E_p} \frac{\partial f}{\partial \alpha} + \text{Cov}(E_p, \beta) \frac{\partial f}{\partial E_p} \frac{\partial f}{\partial \beta} + \text{Cov}(\alpha, \beta) \frac{\partial f}{\partial \alpha} \frac{\partial f}{\partial \beta} \right] \quad (C7) \\ &= \frac{2E_p}{4(2 + \alpha)^2} \left[R_{E_p, \alpha} \sigma_{E_p} \sigma_\alpha \frac{(2 + \beta)(\alpha - \beta)}{2 + \alpha} + R_{E_p, \beta} \sigma_{E_p} \sigma_\beta (\alpha - \beta) + R_{\alpha, \beta} \sigma_\alpha \sigma_\beta \frac{E_p(2 + \beta)}{2 + \alpha} \right].\end{aligned}$$

Using the actual spectral parameters in our sample, with the average correlation coefficients found above, most of the time the cross term was found to be negative, as long as the parameters are more strongly anti-correlated. Therefore, we believe the uncertainties found in Equation C4 without the covariance terms tend to be overestimated.

D. Effective α

The discrepancy between the BAND (or COMP) α and the SBPL λ_1 can be especially severe when the e -folding energy, $E_0 = E_{\text{peak}}/(2 + \alpha)$, is close to the lower energy threshold and the actual low-energy power law component of the BAND or COMP is assumed to lie far below the lower energy bound of the data. As an example, we plot in Figure 37, the BAND and the SBPL model with the same E_{peak} , high-energy index, and $\alpha = \lambda_1 = -1$. The difference between the -1 power law and the actual BAND model behavior is obvious, whereas the SBPL low-energy component does follow the -1 power law.

To resolve this issue and to more accurately represent the low-energy behavior of the LAD data, we calculate the “effective” α of the BAND and COMP models, introduced by Preece et al. (1998b). The effective α is simply the spectral slope in $\log f - \log E$ (Equations 2 and 3) determined at some fiducial energy, chosen to be 25 keV, and is given by

$$\alpha_{\text{eff}} = \alpha - \frac{25 \text{ keV}}{E_{\text{peak}}}(2 + \alpha) = \alpha - \frac{25 \text{ keV}}{E_0}. \quad (\text{D1})$$

By defining α_{eff} , we assume that at 25 keV the low-energy power law has already been reached. The energy of 25 keV was chosen because it is the lower energy bound of LADs (Preece et al. 1998b) and also the tangential slope at this energy seems to represent the data better than at other energies we tested, such as 10 keV, 50 keV, or certain fraction of E_{peak} , E_b , or E_0 . The correction term is larger for lower E_0 values. In Figure 38, we compare the BAND α and α_{eff} of the time-resolved spectra in our sample. As seen in Figure 38, α_{eff} correction lowers the index values, making them more consistent with λ_1 of SBPL (Figure 14, bottom right panel).

D.1. Error Propagation ($\sigma_{\alpha_{\text{eff}}}$)

The variance of α_{eff} , without the correlated terms, can be written as

$$\sigma_{\alpha_{\text{eff}}}^2 = \sigma_{E_{\text{peak}}}^2 \left(\frac{\partial f}{\partial E_{\text{peak}}} \right)^2 + \sigma_{\alpha}^2 \left(\frac{\partial f}{\partial \alpha} \right)^2, \quad (\text{D2})$$

where

$$\begin{aligned} \frac{\partial f}{\partial E_{\text{peak}}} &= \frac{25(2 + \alpha)}{E_{\text{peak}}^2} \\ \frac{\partial f}{\partial \alpha} &= 1 - \frac{25}{E_{\text{peak}}}. \end{aligned}$$

Therefore, the α_{eff} uncertainty is

$$\sigma_{\alpha_{\text{eff}}} = \sqrt{\sigma_{E_{\text{peak}}}^2 \left(\frac{25(2+\alpha)}{E_{\text{peak}}^2} \right)^2 + \sigma_{\alpha}^2 \left(1 - \frac{25}{E_{\text{peak}}} \right)^2}. \quad (\text{D3})$$

The correlation term neglected above is

$$2 \left[R_{E_{\text{peak}},\alpha} \sigma_{E_{\text{peak}}} \sigma_{\alpha} \frac{\partial f}{\partial E_{\text{peak}}} \frac{\partial f}{\partial \alpha} \right] = 2 \left[R_{E_{\text{peak}},\alpha} \sigma_{E_{\text{peak}}} \sigma_{\alpha} \frac{25(2+\alpha)}{E_{\text{peak}}^2} \left(1 - \frac{25}{E_{\text{peak}}} \right) \right], \quad (\text{D4})$$

where $R_{E_{\text{peak}},\alpha}$ was found to be negative (see §C.2). Consequently, the error estimated from Equation D3 may also be larger than the actual values.

REFERENCES

- Amati, L., et al. 2002, *A&A*, 390, 81
- Band, D.L., 1997, *ApJ*, 486, 928
- Band, D.L. & Preece, R.D., 2005, *ApJ*, 627, 319
- Band, D.L., et al. 1993, *ApJ*, 413, 281
- Baring, M.G. & Braby, M.L., 2004, *ApJ*, 613, 460
- Bevington, P.R. & Robinson, D.K., 2003, *Data Reduction and Error Analysis for the Physical Sciences*, 3rd Edition (New York: McGraw-Hill)
- Bhat, P.N., et al. 1992, *Nature*, 359, 217
- Briggs, M.S., 1996, in *Gamma-Ray Bursts*, 3rd Huntsville Symposium, ed. C. Kouveliotou, M. Briggs & G. Fishman, AIP, 384, 133
- Crider, A., et al. 1997, *ApJ*, 479, L39
- Crider, A., et al. 1999, *A&AS*, 138, 401
- Dezalay, J.-P., et al. 1992, in *Gamma-Ray Bursts*, 1st Huntsville Symposium, ed. W. Paciesas & G. Fishman, AIP, 265, 304
- Dezalay, J.-P., et al. 1997, *ApJ*, 490, L17
- Fishman, G.J., et al. 1989, in *Proc. GRO Science Workshop*, GSFC, 2-39

- Ford, L.A., et al. 1995, ApJ, 439, 307
- Gallant, Y.A., 2002, in *Relativistic Flows in Astrophysics*, ed. A. Guthmann et al., Lecture Notes in Physics (Heidelberg:Springer-Verlag), 589, 24
- Gehrels, N., Chipman, E., & Kniffen, D., 1994, ApJS, 92, 351
- Ghirlanda, G., et al. 2002, A&A, 393, 409
- Ghirlanda, G., et al. 2005, MNRAS, 361, L10
- Ghisellini, G. & Celotti, A., ApJ, 511, L93
- Harmon, B.A., et al. 2002, ApJS, 138, 149
- Kaneko, Y., 2005, Ph.D. Dissertation, University of Alabama in Huntsville
- Katz, J.I., 1994, ApJ, 432, L107
- Kouveliotou, C., et al. 1993, ApJ, 413, L101
- Liang, E.P. & Kargatis, V.E., 1996, Nature, 381, 49
- Lloyd, N.M., et al. 2000, ApJ, 534, 227
- Lloyd-Ronning, N.M. & Petrosian, V., ApJ, 565, 182
- Mallozzi, R.S., et al. 1995, ApJ, 454, 597
- Mallozzi, R.S., Preece, R.D. & Briggs, M.S., 2005, “RMFIT, A Lightcurve and Spectral Analysis Tool”, ©2005 Robert D. Preece, University of Alabama in Huntsville
- Medvedev, M.V., 2000, ApJ, 540, 704
- Nemiroff, R.J., et al. 1994, ApJ, 435, L133
- Nakar, E. & Piran, T., 2005b, MNRAS, 360, L73
- Nakar, E. & Piran, T., 2005c, astro-ph/0503517
- Paciesas, W.S., et al. 1999, ApJS, 122, 465
- Paciesas, W.S., et al. 2003, in *Gamma-Ray Bursts and Afterglow Astronomy*, ed. G. Ricker & R. Vanderspek, AIP, 662, 248
- Pendleton, G.N., et al. 1995, Nuc. Inst. & Met. A, 364, 567

- Pendleton, G.N., et al. 1997, ApJ, 489, 175
- Preece, R.D., Briggs, M.S., Mallozzi, R.S., & Brock, M.N., 1994, “WINdows Gamma SPectral ANALysis (WINGSPAN)”
- Preece, R.D., et al. 1998a, ApJ, 496, 849
- Preece, R.D., et al. 1998b, ApJ, 506, L23
- Preece, R.D., et al. 2000, ApJS, 126, 19 (SP1)
- Preece, R.D., et al. 2002, ApJ, 581, 1248
- Press et al., 1992, *Numerical Recipes in FORTRAN*, 2nd Edition (New York: Cambridge University Press)
- Rybicki, G.B. & Lightman, A.P., 1979, *Radiative Processes in Astrophysics* (New York: John Wiley & Sons)
- Ryde, F., 1999, Astrophys. Lett., 39, 281
- Sakamoto, T., et al. 2004, ApJ, 602, 875
- Sakamoto, T., et al. 2005, ApJ, 629, 311
- Sari, R., et al. 1998, ApJ, 497, L17
- Tavani, M., 1996, ApJ, 466, 768
- Zhang, B. & Mészáros, P., 2002, ApJ, 581, 1236

Table 1: Basic properties of 350 GRBs included in the catalog.

GRB Name ^a	BATSE Trig #	Trigger Time ^b (UT,s)	Data Type	LAD #	Time Interval ^c		Energy Interval		# of Spectra
					Start (s)	End (s)	Start (keV)	End (MeV)	
(1)	(2)	(3)	(4)	(5)	(6)	(7)	(8)	(9)	(10)
910421	105	33243	HERB	7	0.064	5.184	27.109	1948.42	12
910425	109	2265	MER	0,4	-14.336	86.815	32.506	1813.54	26
910430	130	61719	CONT	6	-17.408	64.512	36.383	1799.34	22
910503	143	25452	HERB	6	0.000	18.560	32.275	1900.93	46
910522	219	43929	MER	4,5,6	105.947	133.147	33.638	1821.76	13
910525	226	69987	CONT	5	-3.072	171.010	32.678	1853.06	19
910601	249	69734	MER	0,2,4,6	0.107	45.019	34.665	1814.08	68
910602	257	82501	HERB	0	0.000	17.664	33.151	2039.36	7
W910609	298	2907	CONT	4	-1.408	0.640	31.936	1817.69	1

^a Prefix C – Calibration burst; W – Weak burst with a single spectrum.

^b In seconds of day.

^c Time since trigger.

Note. — The complete version of this table is in the electronic edition of the Journal. The printed edition contains only a sample.

Table 2: BATSE LAD burst data types used in this work.

Data Type	Number of Energy Chan	Number of Spectra	Time Resolution (s)	Detector Subset	Time Coverage
HERB	128	128	0.128 ^a	DSELH ^b	$\lesssim 500$ s
HER	128	—	~ 300	All	Background
MER	16	4096	0.016 & 0.064 ^c	DSELB ^d	163.84 s
CONT	16	—	2.048	All	Continuous ^e

^a Minimum for time-to-spill, increases by 64 ms increments.

^b DSELH: 4 detectors with highest count rates, determined at trigger.

^c The change to 64 ms resolution is after the first 32.768 s.

^d DSELB: The 2–4 detectors with highest count rates, as determined at the time of the trigger (MER is summed over these detectors).

^e Can serve as background data.

Table 3: Example fit results to simulated BAND spectra (upper two tables) and to simulated COMP spectra (lower two tables). The parameters are median values and the standard deviations are shown in parentheses.

Simulated BAND Parameters: $E_{\text{peak}} = 559.5 \text{ keV}$, $\alpha = -0.52$, $\beta = -2.24$								
BAND Fit Parameters					COMP Fit Parameters			
$\langle S/N \rangle$	$\langle E_{\text{peak}} \rangle$	$\langle \alpha \rangle$	$\langle \beta \rangle$	$\langle \chi^2 \rangle / \text{dof}$	$\langle E_{\text{peak}} \rangle$	$\langle \alpha \rangle$	$\langle \chi^2 \rangle / \text{dof}$	$\Delta \chi^2$
285.1	559 (14)	-0.52 (0.02)	-2.23 (0.05)	111.2/112	746 (14)	-0.66 (0.01)	252.3/113	141.1
75.9	585 (60)	-0.53 (0.07)	-2.21 (0.32)	109.4/112	740 (55)	-0.65 (0.05)	118.4/113	9.0
12.3	549 (427)	-0.45 (0.72)	-1.77 (1.78)	108.6/112	1083 (1E4)	-0.74 (0.29)	109.2/113	0.6

Simulated BAND Parameters: $E_{\text{peak}} = 493.5 \text{ keV}$, $\alpha = -0.97$, $\beta = -2.36$								
BAND Fit Parameters					COMP Fit Parameters			
$\langle S/N \rangle$	$\langle E_{\text{peak}} \rangle$	$\langle \alpha \rangle$	$\langle \beta \rangle$	$\langle \chi^2 \rangle / \text{dof}$	$\langle E_{\text{peak}} \rangle$	$\langle \alpha \rangle$	$\langle \chi^2 \rangle / \text{dof}$	$\Delta \chi^2$
143.6	494 (38)	-0.97 (0.04)	-2.28 (0.34)	110.1/111	593 (36)	-1.03 (0.03)	122.1/112	12.0
27.5	467 (288)	-0.91 (0.25)	-1.97 (1.56)	105.3/111	679 (386)	-1.03 (0.13)	106.2/112	0.9
3.3	299 (517)	-0.53 (2.05)	-1.46 (1.97)	111.4/111	1388 (5E6)	-0.85 (3.19)	111.0/112	-0.4

Simulated COMP Parameters: $E_{\text{peak}} = 760 \text{ keV}$, $\alpha = -0.70$								
BAND Fit Parameters					COMP Fit Parameters			
$\langle S/N \rangle$	Failed ^a	$\langle E_{\text{peak}} \rangle$	$\langle \alpha \rangle$	$\langle \beta \rangle$	$\langle \chi^2 \rangle / \text{dof}$	$\langle E_{\text{peak}} \rangle$	$\langle \alpha \rangle$	$\langle \chi^2 \rangle / \text{dof}$
76.9	32	753 (73)	-0.66 (0.05)	-2.84 (1.89)	113.8/112	797 (63)	-0.69 (0.05)	114.5/113
286.3	26	747 (15)	-0.67 (0.01)	-3.65 (1.18)	110.8/112	760 (12)	-0.68 (0.01)	112.0/113
533.9	36	752 (8)	-0.67 (0.01)	-3.99 (1.02)	114.1/112	759 (6)	-0.68 (0.01)	114.2/113

Simulated COMP Parameters: $E_{\text{peak}} = 300 \text{ keV}$, $\alpha = -1.20$								
BAND Fit Parameters					COMP Fit Parameters			
$\langle S/N \rangle$	Failed ^a	$\langle E_{\text{peak}} \rangle$	$\langle \alpha \rangle$	$\langle \beta \rangle$	$\langle \chi^2 \rangle / \text{dof}$	$\langle E_{\text{peak}} \rangle$	$\langle \alpha \rangle$	$\langle \chi^2 \rangle / \text{dof}$
87.5	11	305 (26)	-1.20 (0.05)	-3.18 (2.02)	112.8/112	322 (25)	-1.23 (0.05)	113.4/113
133.5	4	300 (15)	-1.19 (0.03)	-3.29 (1.55)	111.0/112	310 (12)	-1.21 (0.03)	111.3/113
456.3	8	299 (4)	-1.20 (0.01)	-4.51 (1.79)	109.3/112	301 (3)	-1.20 (0.01)	109.8/113

^a Number of failed fits out of 100 trials, due to poor parameter constraints.

Table 4: Results of BAND and COMP fits to simulated SBPL spectra ($S/N \sim 100$) with various Λ . The simulated Parameters are $A = 0.05$, $E_b = 300$ keV, $\lambda_1 = -1.0$, and $\lambda_2 = -2.5$. “ E_{peak} ” is the calculated νF_ν peak energy in the SBPL spectra. The parameters are median values and the standard deviations are shown in parentheses.

Simulated		BAND Fit Parameters					COMP Fit Parameters			
Λ	“ E_{peak} ” ^a	$\langle A \rangle^b \times 10^3$	$\langle E_{\text{peak}} \rangle^a$	$\langle \alpha \rangle$	$\langle \beta \rangle$	$\langle \chi^2 \rangle / \text{dof}$	$\langle A \rangle^b \times 10^3$	$\langle E_{\text{peak}} \rangle^a$	$\langle \alpha \rangle$	$\langle \chi^2 \rangle / \text{dof}$
0.01	302	70 (0.3)	457 (4)	−0.68 (0.01)	−2.93 (0.06)	962.3/112	68 (0.3)	483 (3)	−0.71 (0.01)	1065.6/113
0.10	325	70 (0.4)	448 (4)	−0.69 (0.01)	−2.85 (0.04)	608.4/112	67 (0.3)	479 (3)	−0.73 (0.01)	733.2/113
0.20	352	69 (0.4)	434 (4)	−0.74 (0.01)	−2.64 (0.04)	295.1/112	66 (0.3)	477 (4)	−0.79 (0.01)	481.6/113
0.30	381	67 (0.5)	419 (5)	−0.80 (0.01)	−2.48 (0.04)	152.4/112	63 (0.3)	479 (4)	−0.87 (0.01)	377.8/113
0.40	413	66 (0.6)	406 (6)	−0.86 (0.01)	−2.33 (0.03)	119.9/112	61 (0.3)	492 (5)	−0.95 (0.01)	426.3/113
0.50	447	65 (0.5)	402 (7)	−0.94 (0.01)	−2.25 (0.02)	120.7/112	59 (0.3)	504 (5)	−1.03 (0.01)	408.4/113
0.60	484	64 (0.7)	396 (8)	−1.00 (0.01)	−2.18 (0.02)	127.8/112	58 (0.2)	519 (6)	−1.10 (0.01)	454.0/113
0.70	524	63 (0.5)	396 (7)	−1.06 (0.01)	−2.13 (0.02)	140.2/112	57 (0.2)	540 (7)	−1.16 (0.01)	432.9/113
0.80	568	62 (0.6)	394 (9)	−1.11 (0.01)	−2.07 (0.02)	141.1/112	56 (0.2)	567 (8)	−1.22 (0.01)	446.3/113
0.90	615	62 (0.7)	397 (12)	−1.15 (0.01)	−2.04 (0.02)	142.1/112	55 (0.2)	591 (9)	−1.27 (0.01)	432.6/113
1.00	666	61 (0.6)	404 (12)	−1.20 (0.01)	−2.02 (0.02)	135.3/112	54 (0.2)	613 (10)	−1.30 (0.01)	400.9/113

^a in keV

^b in $\text{ph s}^{-1} \text{ cm}^{-2} \text{ keV}^{-1}$

Table 5: The percentage of fits resulted in χ^2 with goodness of fit of 3σ (99.7%) or better out of the total number of 350 time-integrated spectra and 8459 time-resolved spectra.

	PWRL	COMP	BAND	SBPL
Time-Integrated	11.1%	68.6%	84.6%	88.6%
Time-Resolved	23.3%	95.7%	92.3%	99.2%

Table 6: Free parameters in each model.

Model	Amplitude	Low-E Index	High-E Index	Peak Energy	Break Energy	Break Scale
PWRL	A	λ	—	—	—	—
COMP	A	α	—	E_{peak}	—	—
BAND	A	α	β	E_{peak}	—	—
SBPL	A	λ_1	λ_2	—	E_b	Λ

Table 7: The median *good* parameter values and the dispersion (quartile) of the distributions determined by fitting all spectra, both time-integrated and time-resolved, separately with four models.

Time-Integrated Parameters						
	Low Index	High Index	E_{peak} (keV)	E_{b} (keV)	ΔS	
PWRL	$-1.64^{+0.11}_{-0.16}$	$-1.64^{+0.11}_{-0.16}$	—	—	—	
COMP	$-1.18^{+0.24}_{-0.19}$	—	321^{+202}_{-105}	—	—	
BAND	$-1.08^{+0.23}_{-0.16}$	$-2.33^{+0.22}_{-0.32}$	262^{+119}_{-80}	195^{+91}_{-64}	$1.44^{+0.36}_{-0.28}$	
SBPL	$-1.20^{+0.27}_{-0.18}$	$-2.43^{+0.30}_{-0.38}$	234^{+101}_{-61}	218^{+109}_{-61}	$1.42^{+0.56}_{-0.37}$	

Time-Resolved Parameters						
	Low Index	High Index	E_{peak} (keV)	E_{b} (keV)	ΔS	
PWRL	$-1.74^{+0.19}_{-0.19}$	$-1.74^{+0.19}_{-0.19}$	—	—	—	
COMP	$-1.04^{+0.24}_{-0.27}$	—	364^{+204}_{-138}	—	—	
BAND	$-0.90^{+0.23}_{-0.26}$	$-2.33^{+0.26}_{-0.32}$	268^{+127}_{-98}	190^{+94}_{-60}	$1.57^{+0.48}_{-0.39}$	
SBPL	$-1.05^{+0.25}_{-0.27}$	$-2.42^{+0.30}_{-0.40}$	235^{+117}_{-79}	225^{+102}_{-69}	$1.51^{+0.48}_{-0.38}$	

Table 8: Model comparison summary. The best-fit models were first determined statistically by χ^2 probabilities (Column 1). In the case that several models resulted in comparable good fits, Column 1 lists these by their initial letters, separated by forward slashes. In a second step, the model with the more constrained parameters was designated as the best-fit (BEST) model. Columns 3 - 6 and 8 - 11 lists the number of spectra for each BEST model.

Best-Fit Model (1)	Time Integrated					Time Resolved				
	Total (2)	PWRL (3)	COMP (4)	BAND (5)	SBPL (6)	Total (7)	PWRL (8)	COMP (9)	BAND (10)	SBPL (11)
PWRL	8	8	–	–	–	171	171	–	–	–
COMP	45	–	45	–	–	1811	–	1811	–	–
BAND	48	–	–	48	–	823	–	–	823	–
SBPL	50	–	–	–	50	101	–	–	–	101
P/B/C/S	2	0	0	0	2	24	2	3	0	19
C/B/S	54	–	2	7	45	1535	–	88	192	1255
P/C/B	4	0	4	0	–	149	37	104	8	–
P/C/S	1	1	0	–	0	19	9	6	–	4
P/B/S	1	1	–	0	0	9	5	–	0	4
P/C	6	5	1	–	–	181	85	96	–	–
P/B	1	1	–	0	–	50	44	–	6	–
P/S	2	1	–	–	1	26	13	–	–	13
C/B	27	–	3	24	–	2288	–	609	1679	–
C/S	25	–	12	–	13	688	–	239	–	449
B/S	76	–	–	45	31	584	–	–	144	440
TOTAL	350	17	67	124	142	8459	366	2956	2852	2285
%		4.9	19.1	35.4	40.6		4.3	34.9	33.7	27.0

Table 9: Summary of time-integrated spectral fit results of 350 GRBs. 1σ uncertainties are shown in parentheses.

GRB Name ^a	BATSE Trig #	BEST Model	Spectral Fit Parameters							
			A (ph s ⁻¹ cm ⁻² keV ⁻¹)	$E_{\text{peak}}^{\text{b}}$ (keV)	α , λ_1^{c}	β , λ_2^{d}	E_{b}^{e} (keV)	Λ	χ^2 ^f	dof
910421	105	BAND	0.0785 (0.0054)	137 (4)	-0.80 (0.06)	-2.71 (0.10)	122 (7)	—	125.5	112
910425	109	COMP	0.0081 (0.0004)	523 (87)	-1.24 (0.06)	—	—	—	10.6	11
910430	130	BAND	0.0110 (0.0015)	180 (23)	-1.23 (0.13)	-2.33 (0.22)	141 (31)	—	6.5	10
910503	143	SBPL	0.0482 (0.0001)	586 (28)	-1.06 (0.01)	-2.22 (0.03)	420 (13)	0.20	190.6	112
910522	219	SBPL	0.0198 (0.0001)	240 (12)	-1.23 (0.02)	-2.28 (0.03)	191 (8)	0.20	7.9	10
910525	226	COMP	0.0037 (0.0003)	404 (63)	-1.05 (0.10)	—	—	—	8.8	11
910601	249	SBPL	0.0355 (0.0001)	446 (22)	-1.06 (0.01)	-3.30 (0.07)	537 (21)	0.50	8.6	9
910602	257	PWRL	0.0064 (0.0001)	—	-1.54 (0.01)	—	—	—	136.8	116
W910609	298	SBPL	0.0131 (0.0003)	389 (67)	-1.24 (0.04)	-2.40 (0.28)	387 (66)	0.01	10.6	9

^a Prefix C – Calibration burst; W – Weak burst with a single spectrum

^b *fitted* E_{peak} for BAND or COMP, and *calculated* E_{peak} for SBPL.

^c λ for PWRL, α for BAND, or COMP and λ_1 for SBPL.

^d β for BAND and λ_2 for SBPL.

^e *fitted* E_{b} for SBPL, and *calculated* E_{b} for BAND.

^f Small χ^2 values are expected for calibration bursts by default.

Note. — The complete version of this table is in the electronic edition of the Journal. The printed edition contains only a sample.

Table 10: The median parameter values and the dispersion (quartile) of the BEST model fits. The BEST model set consists of 17 (366) PWRL, 67 (2956) COMP, 124 (2852) BAND, and 142 (2285) SBPL time-integrated (time-resolved) spectra. The constituent parameter distribution values are also shown.

Time-Integrated Parameters						
	Low Index	High Index	E_{peak} (keV)	E_{b} (keV)	ΔS	
BEST	$-1.14^{+0.20}_{-0.22}$	$-2.33^{+0.24}_{-0.26}$	251^{+122}_{-68}	204^{+76}_{-56}	$1.28^{+0.44}_{-0.28}$	
PWRL	$-1.55^{+0.11}_{-0.34}$	$-1.55^{+0.11}_{-0.34}$	—	—	—	
COMP	$-1.20^{+0.22}_{-0.19}$	—	319^{+186}_{-87}	—	—	
BAND	$-0.97^{+0.23}_{-0.21}$	$-2.36^{+0.17}_{-0.22}$	224^{+114}_{-66}	160^{+77}_{-41}	$1.49^{+0.33}_{-0.31}$	
SBPL	$-1.22^{+0.22}_{-0.14}$	$-2.35^{+0.23}_{-0.25}$	245^{+93}_{-63}	226^{+77}_{-46}	$1.10^{+0.39}_{-0.28}$	
Time-Resolved Parameters						
	Low Index	High Index	E_{peak} (keV)	E_{b} (keV)	ΔS	
BEST	$-1.02^{+0.26}_{-0.28}$	$-2.33^{+0.26}_{-0.31}$	281^{+139}_{-99}	205^{+72}_{-55}	$1.47^{+0.45}_{-0.37}$	
PWRL	$-1.86^{+0.27}_{-0.26}$	$-1.86^{+0.27}_{-0.26}$	—	—	—	
COMP	$-1.15^{+0.28}_{-0.25}$	—	334^{+228}_{-140}	—	—	
BAND	$-0.81^{+0.25}_{-0.21}$	$-2.40^{+0.24}_{-0.29}$	273^{+112}_{-92}	189^{+70}_{-53}	$1.69^{+0.43}_{-0.33}$	
SBPL	$-1.07^{+0.19}_{-0.20}$	$-2.29^{+0.27}_{-0.31}$	241^{+104}_{-68}	223^{+74}_{-54}	$1.17^{+0.36}_{-0.29}$	

Table 11: Comparison of the median values for time-integrated and time-resolved spectral parameters. The dispersion (quartile) of each distribution is shown. K-S probabilities and the corresponding parameters for two distributions are also shown.

Spectrum Type	Low Index	High Index	E_{peak} (keV)	E_{b} (keV)	ΔS
Time Integrated	$-1.14^{+0.20}_{-0.22}$	$-2.33^{+0.24}_{-0.26}$	251^{+122}_{-68}	204^{+76}_{-56}	$1.28^{+0.44}_{-0.28}$
Time Resolved	$-1.02^{+0.26}_{-0.28}$	$-2.33^{+0.26}_{-0.31}$	281^{+139}_{-99}	205^{+72}_{-55}	$1.47^{+0.45}_{-0.37}$
P_{KS}	1.18×10^{-16}	0.47	7.73×10^{-3}	0.88	2.14×10^{-4}
D_{KS}	0.23	0.05	0.10	0.04	0.13

Table 12: Summary of total numbers of events considered for each correlation and percentages of events with high significance.

	$E_{\text{peak}} - \alpha$	$E_{\text{b}} - \alpha$	$E_{\text{peak}} - \beta$	$E_{\text{b}} - \beta$	$\alpha - \beta$
Total Number of Events	196	148	117	147	160
Significant Correlation (%)	25.5	13.5	4.3	15.0	6.3

Table 13. List of all bursts in our sample with strong ($> 3\sigma$) spectral parameter correlations in at least one parameter pair. Spearman rank correlation coefficients (r_s) and associated significance probabilities (P_{rs}) are listed. α and β denote low-energy and high-energy indices.

BATSE Trig #	Number of Spectra	$E_{\text{peak}} - \alpha$		$E_b - \alpha$		$E_{\text{peak}} - \beta$		$E_b - \beta$		$\alpha - \beta$	
		r_s	P_{rs}	r_s	P_{rs}	r_s	P_{rs}	r_s	P_{rs}	r_s	P_{rs}
109	26	0.70	8.85E-4	—	—	—	—	—	—	—	—
143	46	—	—	—	—	—	—	-0.61	7.47E-5	—	—
219	13	0.80	9.69E-4	—	—	—	—	—	—	—	—
249	68	0.50	1.55E-5	—	—	—	—	-0.59	3.60E-6	—	—
1085	60	0.80	1.45E-13	0.73	2.11E-10	0.71	2.32E-9	0.60	1.31E-6	0.47	3.00E-4
1141	42	—	—	—	—	—	—	-0.57	5.92E-4	—	—
1288	28	0.63	4.73E-4	—	—	—	—	—	—	—	—
1385	36	—	—	—	—	—	—	-0.73	9.80E-4	—	—
1541	15	0.87	5.68E-5	—	—	—	—	—	—	—	—
1625	37	—	—	0.63	1.19E-4	—	—	—	—	—	—
1652	18	0.84	2.65E-5	—	—	—	—	—	—	—	—
1663	61	—	—	0.59	5.57E-6	—	—	-0.62	1.29E-6	—	—
1676	30	0.74	2.65E-6	0.84	9.14E-5	—	—	—	—	—	—
1695	142	0.44	9.95E-8	—	—	—	—	-0.40	1.03E-5	—	—
1698	32	0.79	1.54E-7	—	—	—	—	—	—	—	—
1872	110	—	—	0.44	5.35E-5	—	—	—	—	-0.51	1.01E-6
1983	54	—	—	—	—	—	—	-0.70	6.17E-6	—	—
2067	45	0.64	2.08E-6	—	—	—	—	-0.68	1.08E-6	—	—
2083	45	0.91	5.99E-17	0.75	5.18E-6	—	—	—	—	—	—
2138	39	—	—	—	—	—	—	-0.77	5.00E-7	—	—
2156	97	0.45	1.79E-5	0.50	8.69E-6	—	—	—	—	—	—
2329	100	—	—	0.60	2.68E-7	—	—	—	—	—	—
2533	70	—	—	—	—	—	—	-0.56	3.52E-5	—	—
2537	26	0.67	3.21E-4	—	—	—	—	—	—	—	—
2661	29	0.68	5.54E-5	—	—	—	—	—	—	—	—
2676	122	0.43	9.16E-7	0.58	6.56E-10	—	—	-0.47	1.66E-6	-0.41	2.92E-5
2790	19	0.85	9.11E-6	—	—	—	—	—	—	—	—
2798	95	0.62	2.96E-10	0.37	8.90E-4	—	—	—	—	—	—
2831	112	0.51	4.56E-8	—	—	—	—	—	—	—	—
2855	35	—	—	—	—	—	—	-0.56	6.16E-4	—	—
2856	114	—	—	0.42	2.63E-4	—	—	—	—	—	—
3002	19	0.74	3.36E-4	—	—	—	—	—	—	—	—
3035	28	0.60	6.70E-4	—	—	—	—	—	—	—	—
3057	165	0.31	2.20E-4	0.40	1.91E-5	—	—	—	—	—	—
3128	44	—	—	—	—	—	—	-0.68	1.81E-5	—	—
3227	50	0.62	1.25E-6	0.60	8.65E-5	—	—	—	—	—	—
3245	116	0.70	8.02E-17	0.60	9.03E-12	0.40	6.83E-5	—	—	—	—
3253	94	0.73	3.41E-17	0.56	1.14E-5	—	—	—	—	-0.46	4.95E-4
3408	63	—	—	—	—	—	—	-0.49	5.29E-4	—	—
3492	49	0.69	1.88E-7	0.65	1.17E-4	—	—	—	—	—	—
3571	22	0.73	1.03E-4	—	—	—	—	—	—	—	—
3658	30	0.68	8.78E-5	—	—	—	—	—	—	—	—
3765	33	0.69	1.16E-5	—	—	—	—	—	—	—	—
3767	20	0.88	3.57E-7	—	—	—	—	—	—	—	—

Table 13—Continued

BATSE Trig #	Number of Spectra	$E_{\text{peak}} - \alpha$		$E_{\text{b}} - \alpha$		$E_{\text{peak}} - \beta$		$E_{\text{b}} - \beta$		$\alpha - \beta$	
		r_s	P_{rs}	r_s	P_{rs}	r_s	P_{rs}	r_s	P_{rs}	r_s	P_{rs}
3870	17	—	—	—	—	—	—	—	—	0.89	5.15E-6
5304	48	0.81	6.06E-12	0.67	8.77E-7	—	—	—	—	—	—
5486	32	—	—	—	—	—	—	—	—	-0.86	1.78E-5
5567	31	—	—	—	—	—	—	-0.72	5.68E-4	—	—
5649	155	0.42	4.50E-8	—	—	—	—	—	—	—	—
5773	57	0.72	3.29E-10	—	—	—	—	—	—	—	—
5995	61	0.63	7.98E-7	—	—	—	—	—	—	0.53	4.71E-4
6124	60	—	—	—	—	-0.50	5.05E-4	-0.73	1.13E-8	—	—
6266	18	—	—	—	—	-0.88	3.30E-4	—	—	—	—
6329	31	0.59	4.94E-4	—	—	—	—	—	—	—	—
6350	44	0.54	6.94E-4	—	—	—	—	-0.52	8.52E-4	—	—
6353	35	0.79	4.22E-4	—	—	—	—	—	—	—	—
6576	21	0.78	8.50E-5	—	—	—	—	—	—	—	—
6587	60	—	—	—	—	—	—	-0.73	3.43E-9	—	—
6630	17	0.85	5.17E-5	—	—	—	—	—	—	—	—
6665	38	—	—	—	—	—	—	-0.58	2.85E-4	—	—
7113	243	—	—	—	—	—	—	—	—	-0.30	6.06E-4
7170	30	0.75	7.79E-4	—	—	—	—	—	—	—	—
7301	56	0.76	6.12E-9	0.57	1.35E-5	0.67	4.58E-4	—	—	0.47	5.10E-4
7343	134	0.63	8.13E-15	0.56	8.40E-9	—	—	—	—	0.35	6.50E-4
7360	32	0.77	2.19E-7	—	—	—	—	—	—	—	—
7491	132	—	—	—	—	—	—	-0.35	3.22E-4	—	—
7575	21	0.85	1.35E-5	—	—	—	—	—	—	—	—
7678	37	—	—	—	—	—	—	-0.70	3.05E-5	—	—
7695	29	0.66	9.16E-5	—	—	—	—	—	—	—	—
7906	59	0.72	9.26E-10	0.56	5.10E-6	—	—	—	—	—	—
7954	27	0.62	5.85E-4	—	—	—	—	—	—	—	—
7976	17	0.88	5.91E-5	—	—	—	—	—	—	—	—
7994	25	0.68	1.60E-4	—	—	—	—	—	—	—	—
8008	27	0.73	2.51E-5	—	—	—	—	—	—	—	—

Table 14: Summary of time-integrated spectral fit results for 17 short GRBs. 1σ uncertainties are shown in parentheses.

GRB Name	BATSE Trig #	# of Spec	BEST Model	Spectral Fit Parameters								
				A (ph s ⁻¹ cm ⁻² keV ⁻¹)	$E_{\text{peak}}^{\text{a}}$ (keV)	$\alpha, \lambda_1^{\text{b}}$	$\beta, \lambda_2^{\text{c}}$	E_{b}^{d} (keV)	Λ	χ^2	dof	
910609	298	1	SBPL	0.0131 (0.0003)	389 (67)	-1.24 (0.04)	-2.40 (0.28)	387 (66)	0.01	10.6	9	
910626	444	1	BAND	0.5183 (0.5078)	91 (13)	0.18 (0.65)	-2.11 (0.07)	60 (7)	—	124.1	114	
920329	1525	1	SBPL	0.0265 (0.0005)	536 (119)	-0.76 (0.06)	-2.44 (0.20)	375 (59)	0.30	12.7	9	
920414	1553	3	SBPL	0.0371 (0.0005)	—	-0.88 (0.03)	-1.74 (0.04)	225 (16)	0.01	119.0	110	
930905	2514	1	SBPL	0.0853 (0.0017)	208 (22)	-1.34 (0.04)	-2.76 (0.20)	212 (21)	0.10	106.1	111	
931205	2679	1	SBPL	0.0241 (0.0009)	792 (212)	-0.54 (0.05)	-2.13 (0.24)	599 (94)	0.10	127.8	114	
940624	3044	1	PWRL	0.0018 (0.0001)	—	-2.20 (0.14)	—	—	—	125.8	114	
940717	3087	1	BAND	0.2097 (0.0431)	182 (20)	-0.59 (0.19)	-2.22 (0.10)	118 (13)	—	139.3	114	
940902	3152	2	SBPL	0.0089 (0.0002)	—	-0.99 (0.04)	-1.79 (0.16)	490 (110)	0.01	138.7	114	
950210	3410	1	COMP	0.0662 (0.0204)	120 (9)	-0.78 (0.29)	—	—	—	122.4	112	
950211	3412	1	PWRL	0.0155 (0.0005)	—	-2.13 (0.06)	—	—	—	115.5	112	
950805	3736	1	COMP	0.0102 (0.0004)	920 (159)	-0.89 (0.08)	—	—	—	10.3	10	
980228	6617	1	SBPL	0.1325 (0.0013)	259 (32)	-1.13 (0.02)	-3.46 (0.31)	309 (31)	0.30	117.7	114	
970704	6293	3	PWRL	0.1817 (0.0026)	—	-1.25 (0.01)	—	—	—	137.2	115	
980330	6668	1	SBPL	0.0166 (0.0010)	—	-1.22 (0.14)	-1.98 (0.19)	149 (37)	0.01	123.0	112	
981226	7281	2	BAND	0.2143 (0.0345)	140 (6)	-0.23 (0.14)	-2.54 (0.10)	103 (6)	—	125.2	113	
000326	8053	5	BAND	0.4870 (0.0423)	90 (1)	-0.50 (0.07)	-3.68 (0.18)	108 (6)	—	122.0	112	

^a *fitted* E_{peak} for BAND or COMP, and *calculated* E_{peak} for SBPL.

^b λ for PWRL, α for BAND, or COMP and λ_1 for SBPL.

^c β for BAND and λ_2 for SBPL.

^d *fitted* E_{b} for SBPL, and *calculated* E_{b} for BAND.

Table 15: Median and quartile values of the BEST spectral parameters for short and long GRBs. K-S probabilities (P_{KS}) and the corresponding K-S parameters (D_{KS}) for two distributions are also shown.

	Low-Energy Index				High-Energy Index				E_{peak} (keV)		E_{b} (keV)	
	Short	Long	Short	Long	Short	Long	Short	Long	Short	Long	Short	Long
Time Integrated	-0.99	$^{+0.21}_{-0.24}$	-1.15	$^{+0.20}_{-0.22}$	-2.31	$^{+0.20}_{-0.23}$	-2.36	$^{+0.23}_{-0.23}$	208	$^{+327}_{-88}$	254	$^{+110}_{-72}$
											218	$^{+157}_{-101}$
P_{KS}		0.07				0.43				0.43		0.20
D_{KS}		0.31				0.25				0.26		0.31
Time Resolved	-0.87	$^{+0.16}_{-0.39}$	-1.02	$^{+0.26}_{-0.28}$	-2.38	$^{+0.39}_{-0.51}$	-2.35	$^{+0.25}_{-0.30}$	168	$^{+222}_{-47}$	281	$^{+139}_{-99}$
											204	$^{+136}_{-93}$
P_{KS}		0.16				0.53				0.08		0.38
D_{KS}		0.22				0.19				0.28		0.22

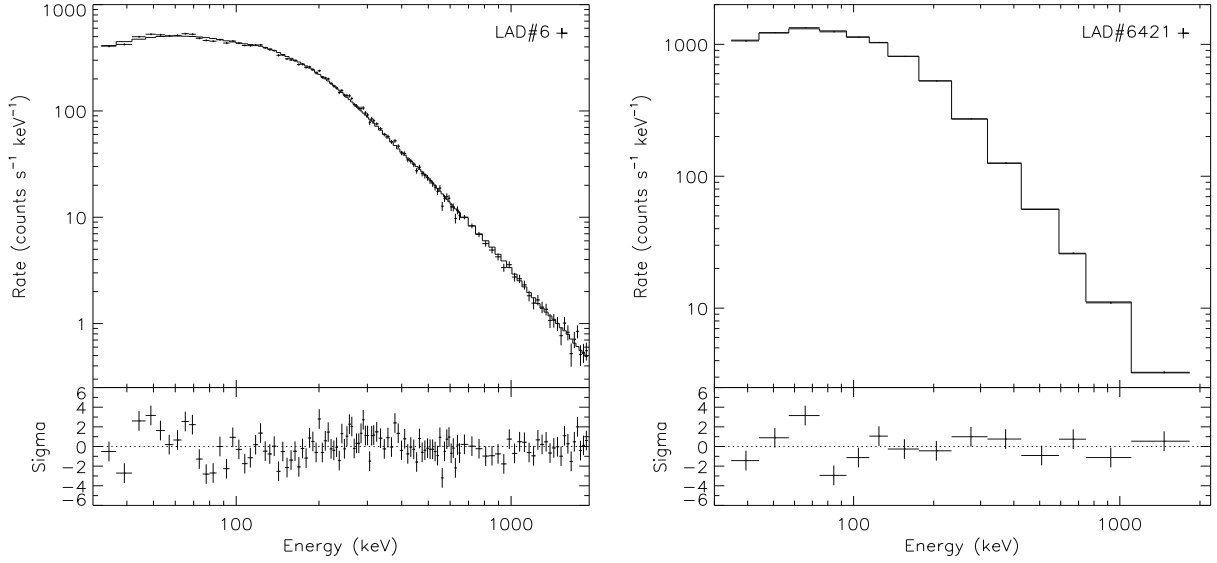


Fig. 1.— Example count spectra of a bright burst that shows the systematic deviations both in the HERB (*left*) and MER (*right*) data. The deviations between the data (crosses) and the model (solid lines) are evident below ~ 100 keV.

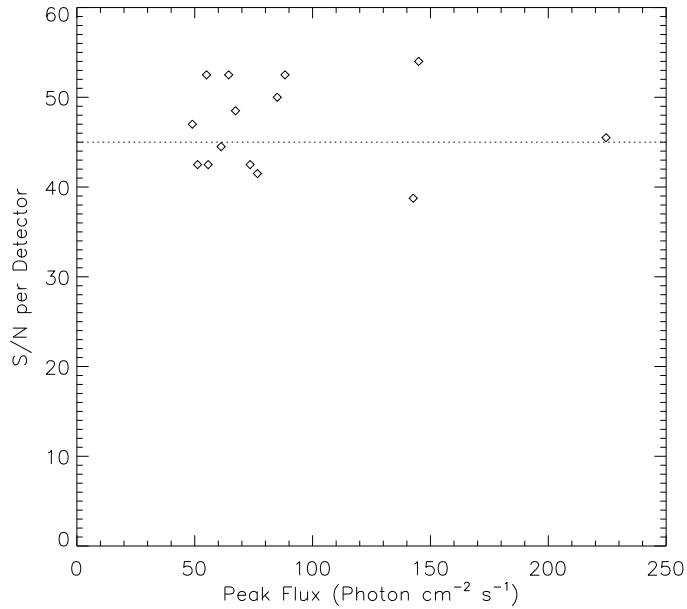


Fig. 2.— S/N per detector for 15 MER bursts that produced the equivalent number of spectra to HERB binned by $S/N \geq 45$ case as a function of the peak photon flux (128 ms, 30 – 2000 keV). The dotted line marks 45σ .

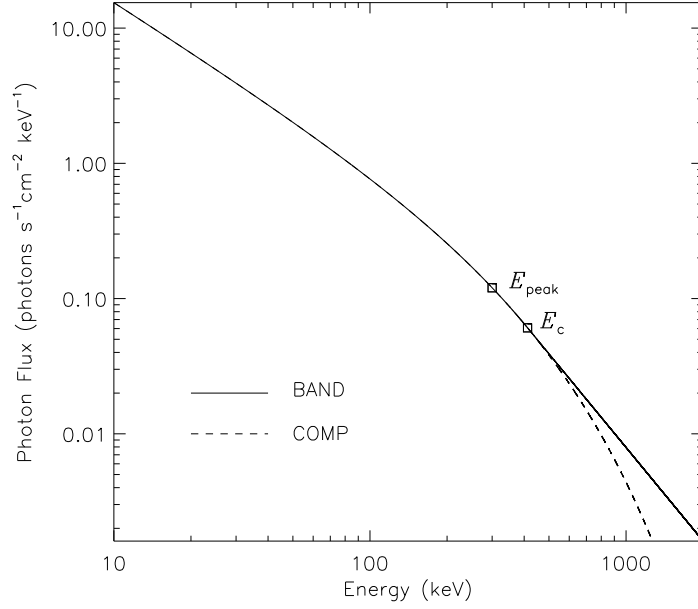


Fig. 3.— Comparison of BAND and COMP models for $A = 0.1$, $\alpha = -1.2$, $E_{\text{peak}} = 300$ keV, and $\beta = -2.3$. E_c is where the high-energy power law of BAND begins.

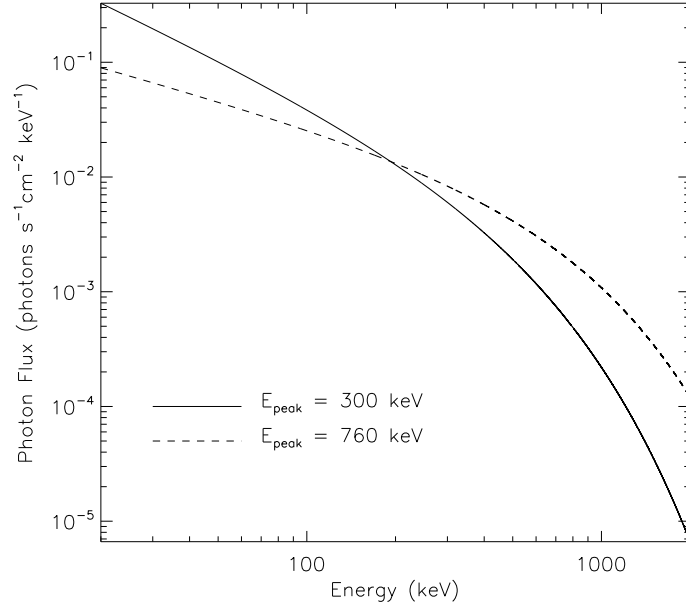


Fig. 4.— Two COMP spectra that produced simulated spectra with $S/N \sim 80$. Low- E_{peak} spectrum (solid curve) can be fitted with the BAND model much more frequently than the high- E_{peak} spectrum (dashed curve).

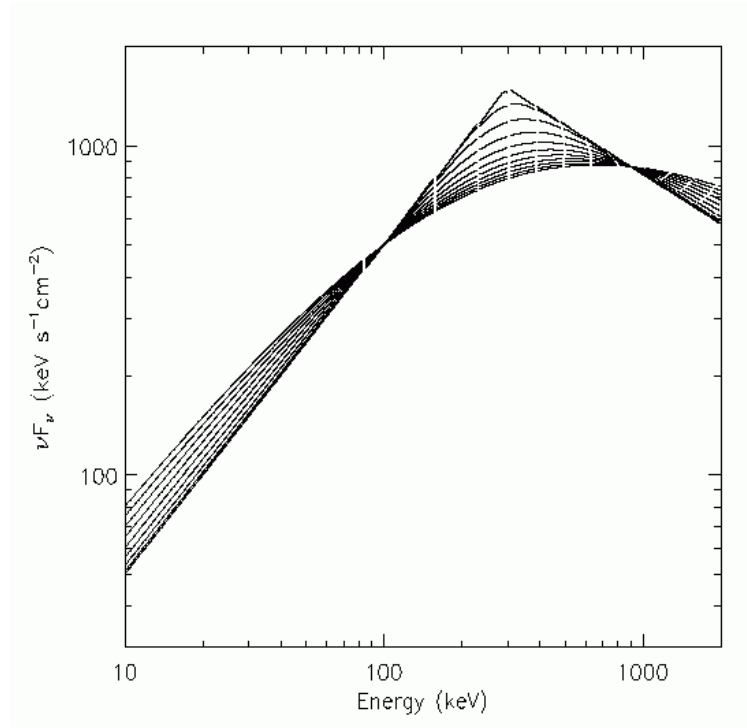


Fig. 5.— The simulated SBPL model spectra with $\Lambda = 0.01, 0.1, 0.2, 0.3, 0.4, 0.5, 0.6, 0.7, 0.8, 0.9$, and 1.0 , from top to bottom at 300 keV. The other parameters are fixed at $A = 0.05$, $E_b = 300$ keV, $\lambda_1 = -1.0$, and $\lambda_2 = -2.5$.

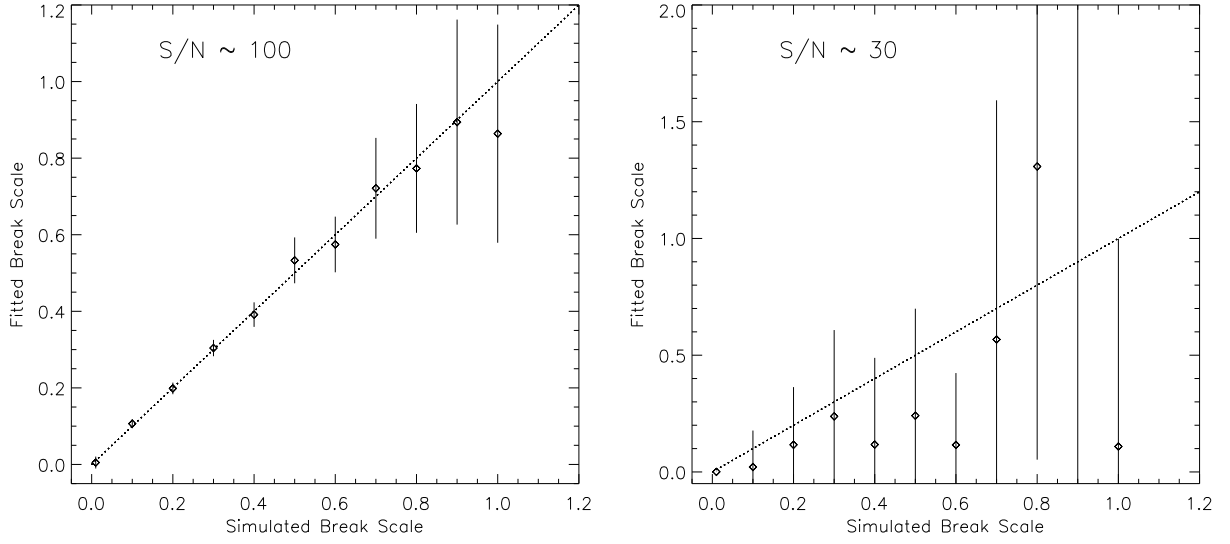


Fig. 6.— The break scale Λ found by 5-parameter SBPL fits to 11 simulated spectra for bright (*left*) and faint (*right*) cases. Horizontal axis shows the simulated Λ values and vertical axis shows the fitted Λ values. The dotted line corresponds to the correct Λ .

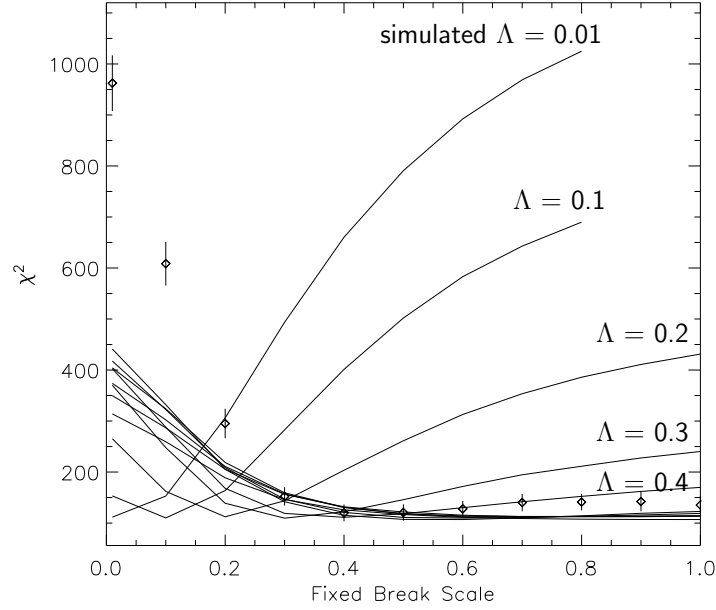


Fig. 7.— Median χ^2 map of 4-parameter SBPL fits to 11 simulated spectra (with $\Lambda = 0.01$ to 1.0, from top to bottom; dof = 113) for the bright case ($S/N \sim 100$). Horizontal axis is the fixed Λ values of the 4-parameter model. The diamonds indicate the median χ^2 from the BAND fits to 11 simulated spectra (dof = 112).

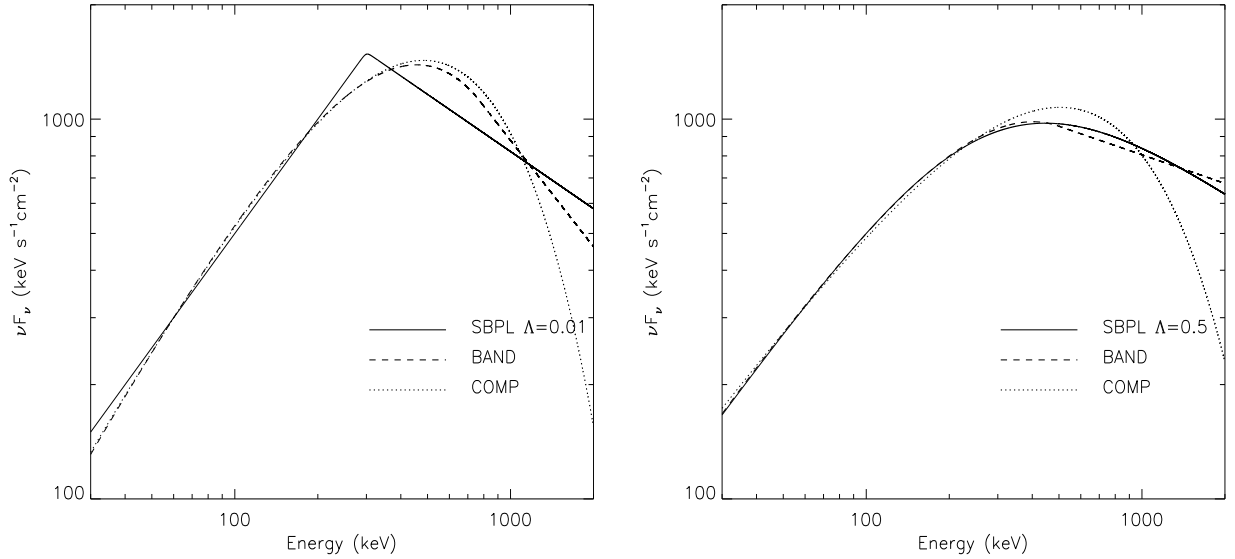


Fig. 8.— Example BAND (dashed lines) and COMP (dotted lines) fits to the simulated SBPL spectra (solid lines) with $\Lambda = 0.01$ (*left*) and with $\Lambda = 0.5$ (*right*).

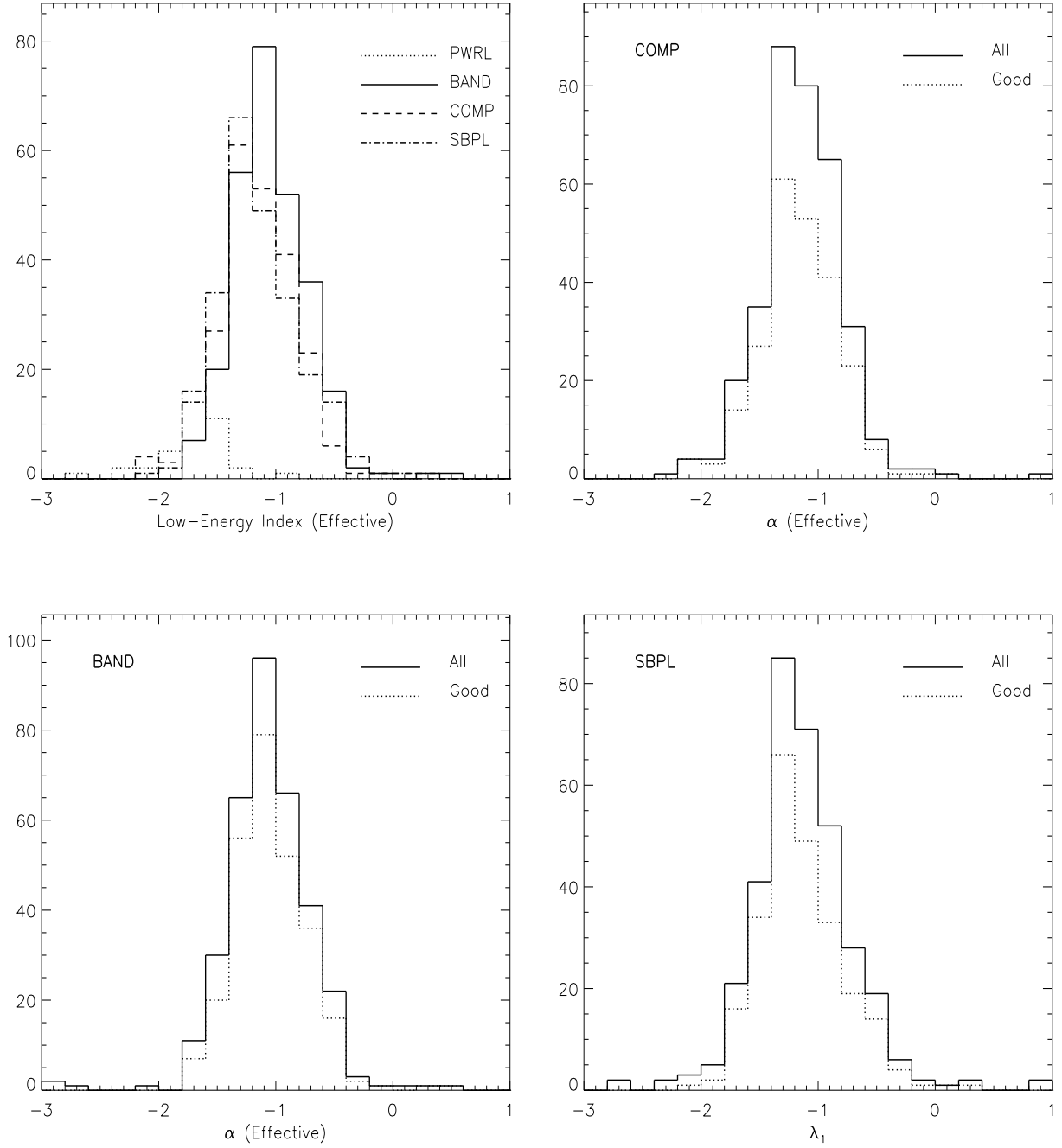


Fig. 9.— Low-energy index distribution of 350 time-integrated spectra. [Top Left] *Good* parameters of all models. Numbers of parameters included are 38 PWRL, 235 COMP, 271 BAND, and 241 SBPL. The other plots show all (solid line) and *good* (dotted line) parameters of COMP, BAND, and SBPL. The lowest (highest) bin includes values lower (higher) than the edge values.

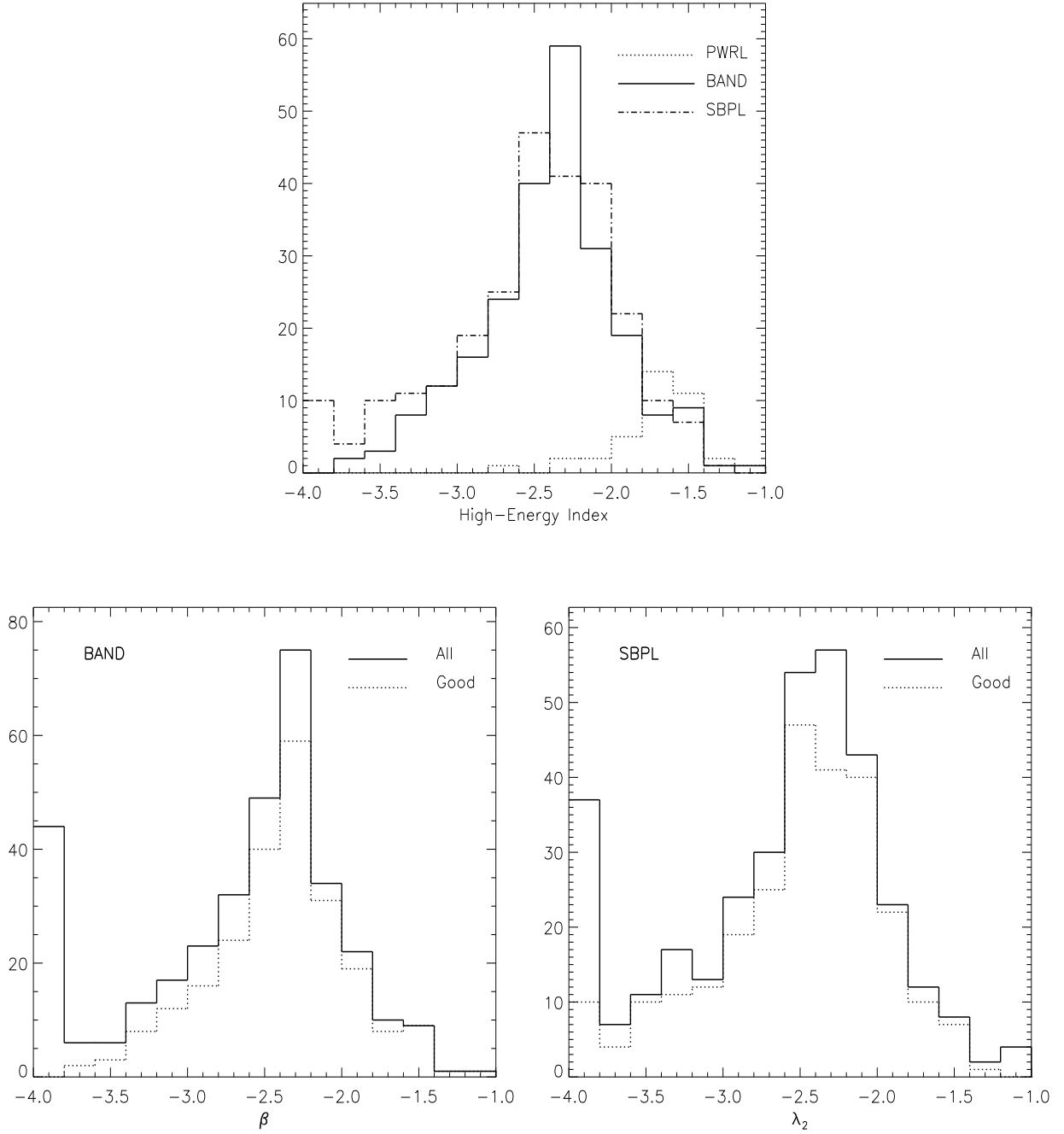


Fig. 10.— High-energy spectral index distribution of 350 time-integrated spectra. [Top] *Good* parameters of all models. Numbers of parameters included are 38 PWRL, 233 BAND, and 259 SBPL. The other plots show all (solid line) and *good* (dotted line) parameters of BAND and SBPL. The lowest (highest) bin includes values lower (higher) than the edge values.

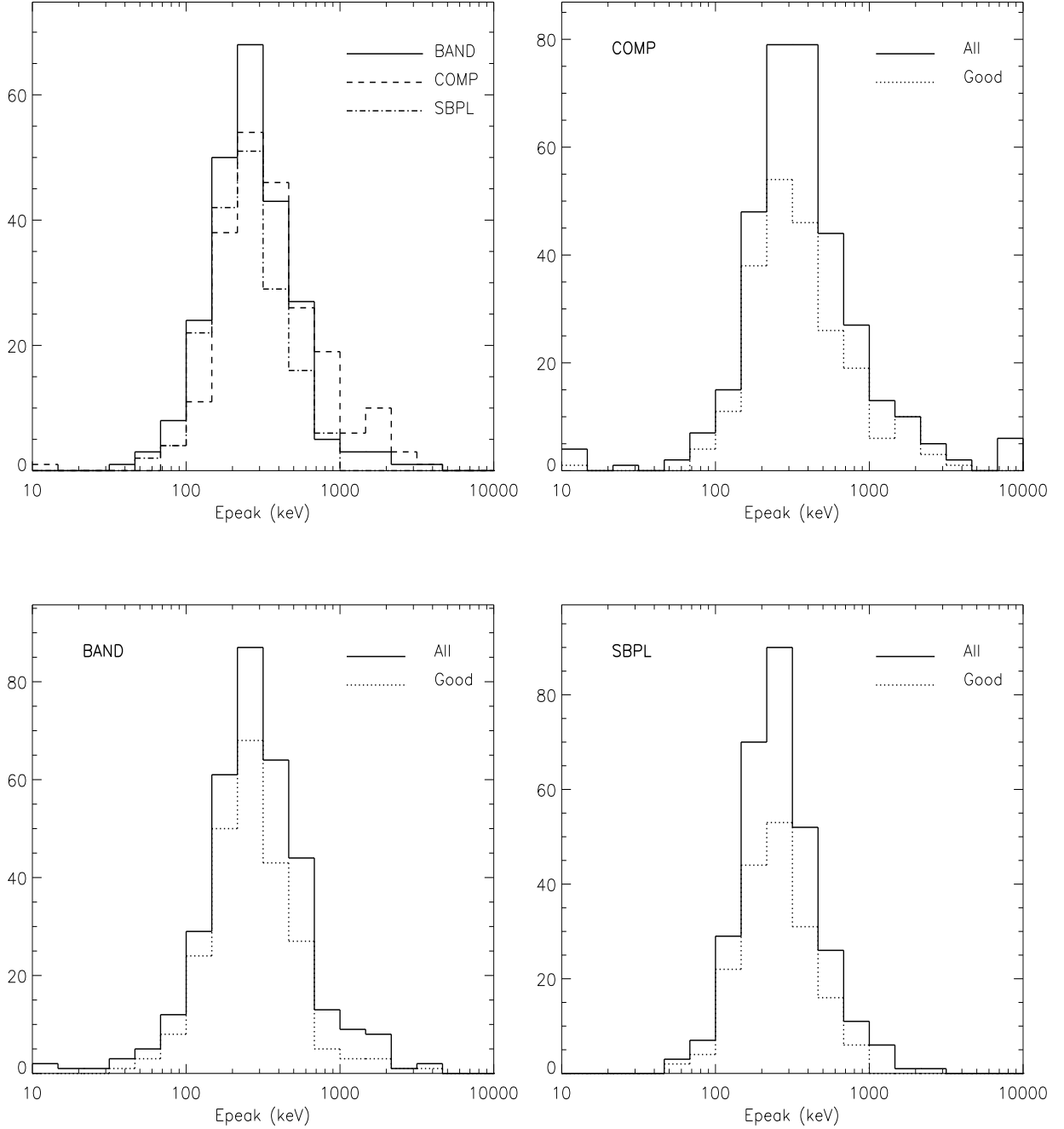


Fig. 11.— E_{peak} distribution of 350 time-integrated spectra. [Top Left] *Good* parameters of all models. Numbers of parameters included are 219 COMP, 237 BAND, and 172 SBPL. The other plots show all (solid line) and *good* (dotted line) parameters of COMP, BAND, and SBPL. The lowest (highest) bin includes values lower (higher) than the edge values.

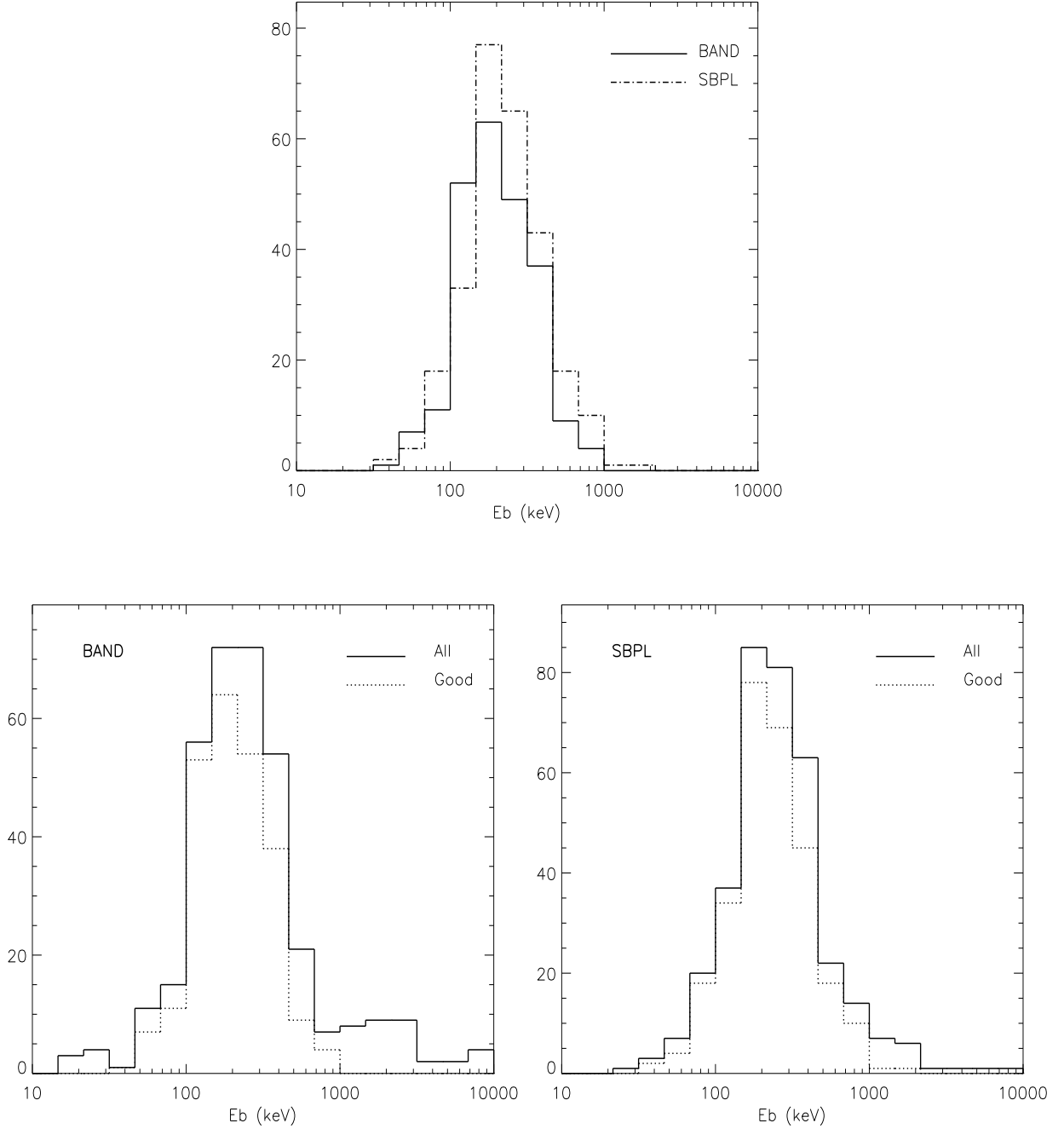


Fig. 12.— Break Energy distribution of 350 time-integrated spectra. [Top] *Good* parameters of all models. Numbers of parameters included are 233 BAND and 272 SBPL. The other plots show all (solid line) and *good* (dotted line) parameters of BAND and SBPL. The lowest (highest) bin includes values lower (higher) than the edge values.

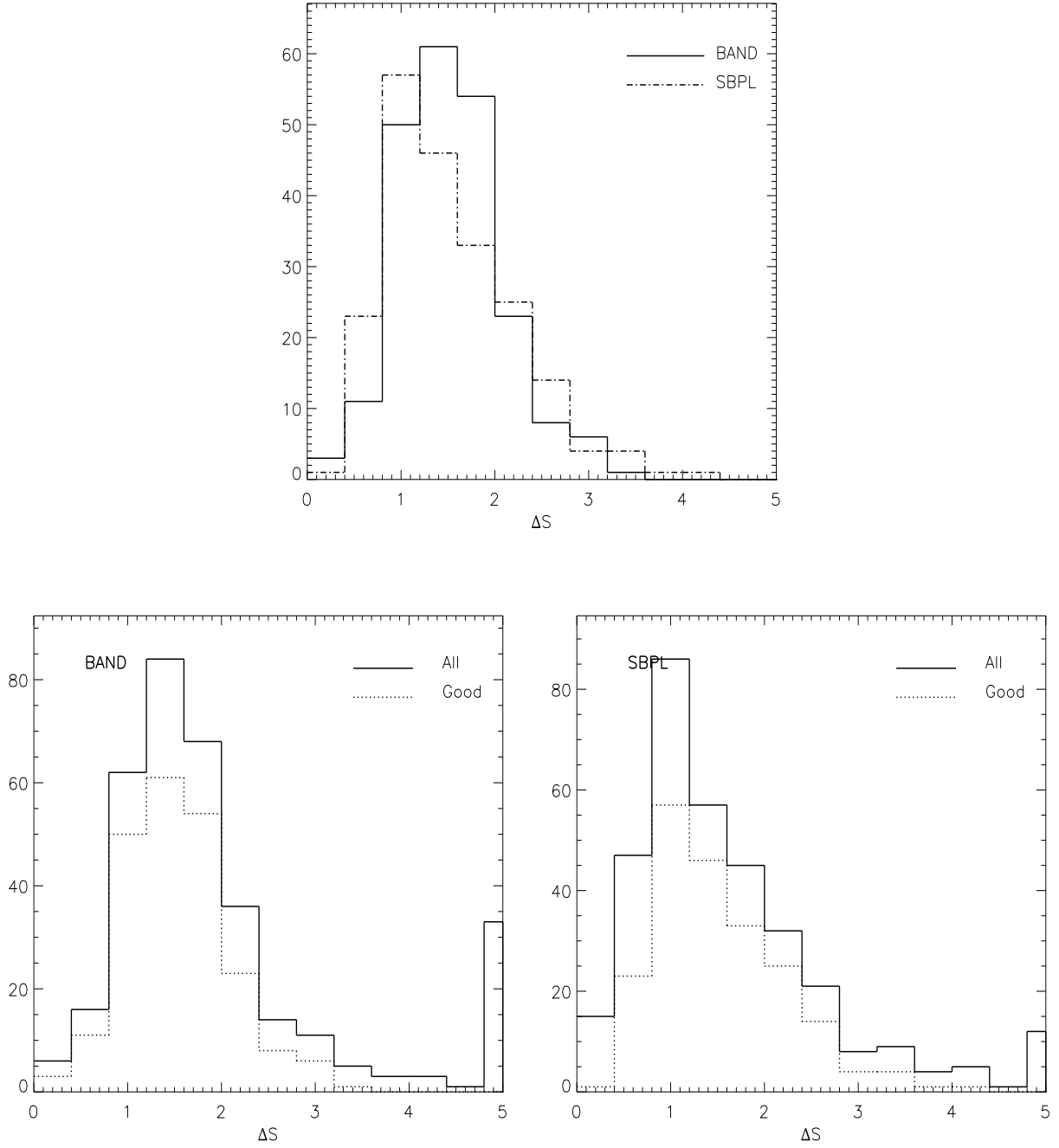


Fig. 13.— ΔS distribution of 350 time-integrated spectra. ΔS is the difference between low-energy and high-energy indices. [Top] *Good* parameters of all models. Numbers of parameters included are 217 BAND and 209 SBPL. The other plots show all (solid line) and *good* (dotted line) parameters of BAND and SBPL. The lowest (highest) bin includes values lower (higher) than the edge values.

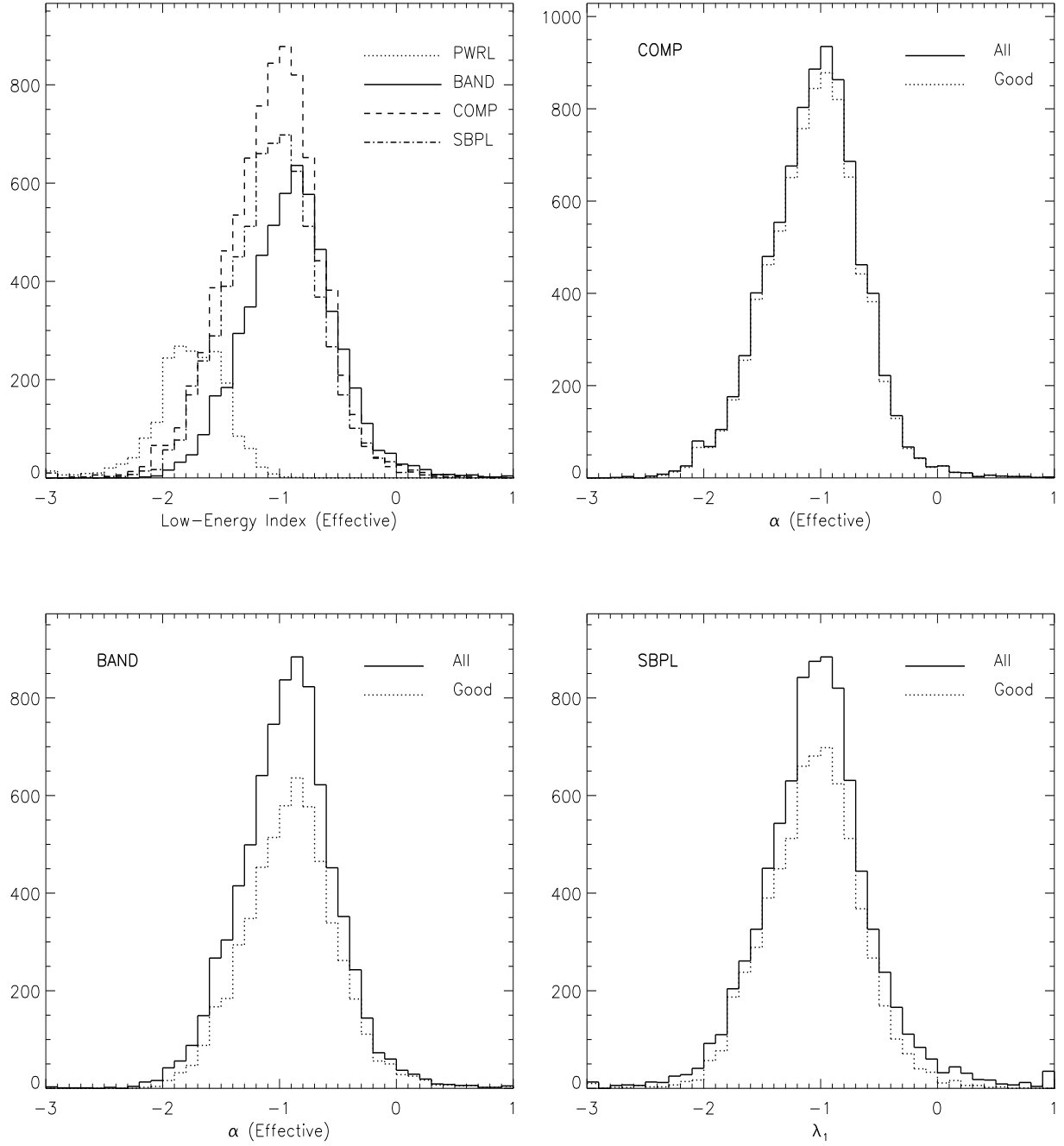


Fig. 14.— Low-energy spectral index distribution of 8459 time-resolved spectra. [Top Left] *Good* parameters of all models. Numbers of parameters included are 1971 PWRL, 8050 COMP, 5510 BAND, and 6533 SBPL. The other plots show all (solid line) and *good* (dotted line) parameters of COMP, BAND, and SBPL. The lowest (highest) bin includes values lower (higher) than the edge values.

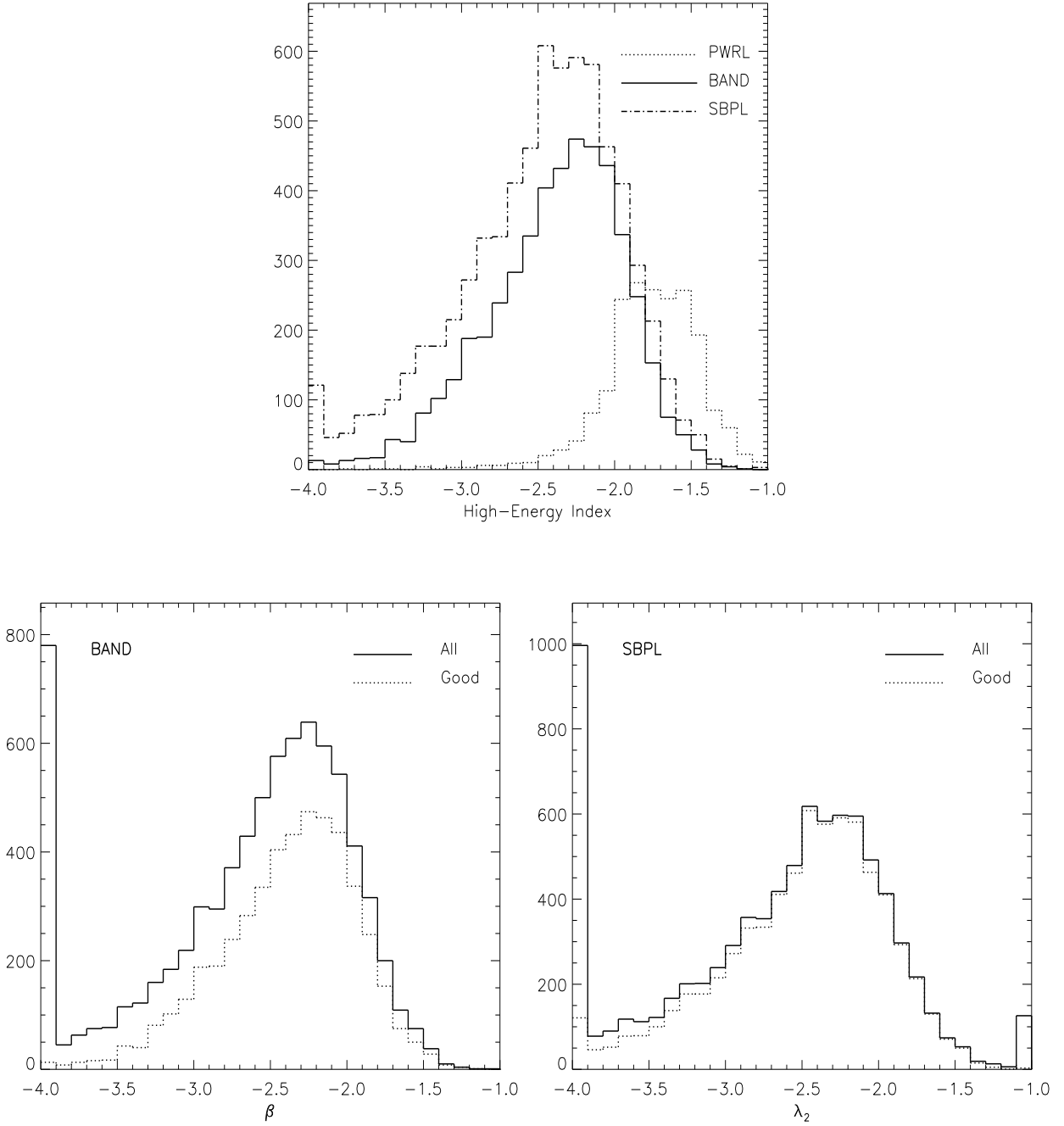


Fig. 15.— High-energy spectral index distribution of 8459 time-resolved spectra. [Top] *Good* parameters of all models. Numbers of parameters included are 1971 PWRL, 4810 BAND, and 7003 SBPL. The other plots show all (solid line) and *good* (dotted line) parameters of BAND and SBPL. The lowest (highest) bin includes values lower (higher) than the edge values.

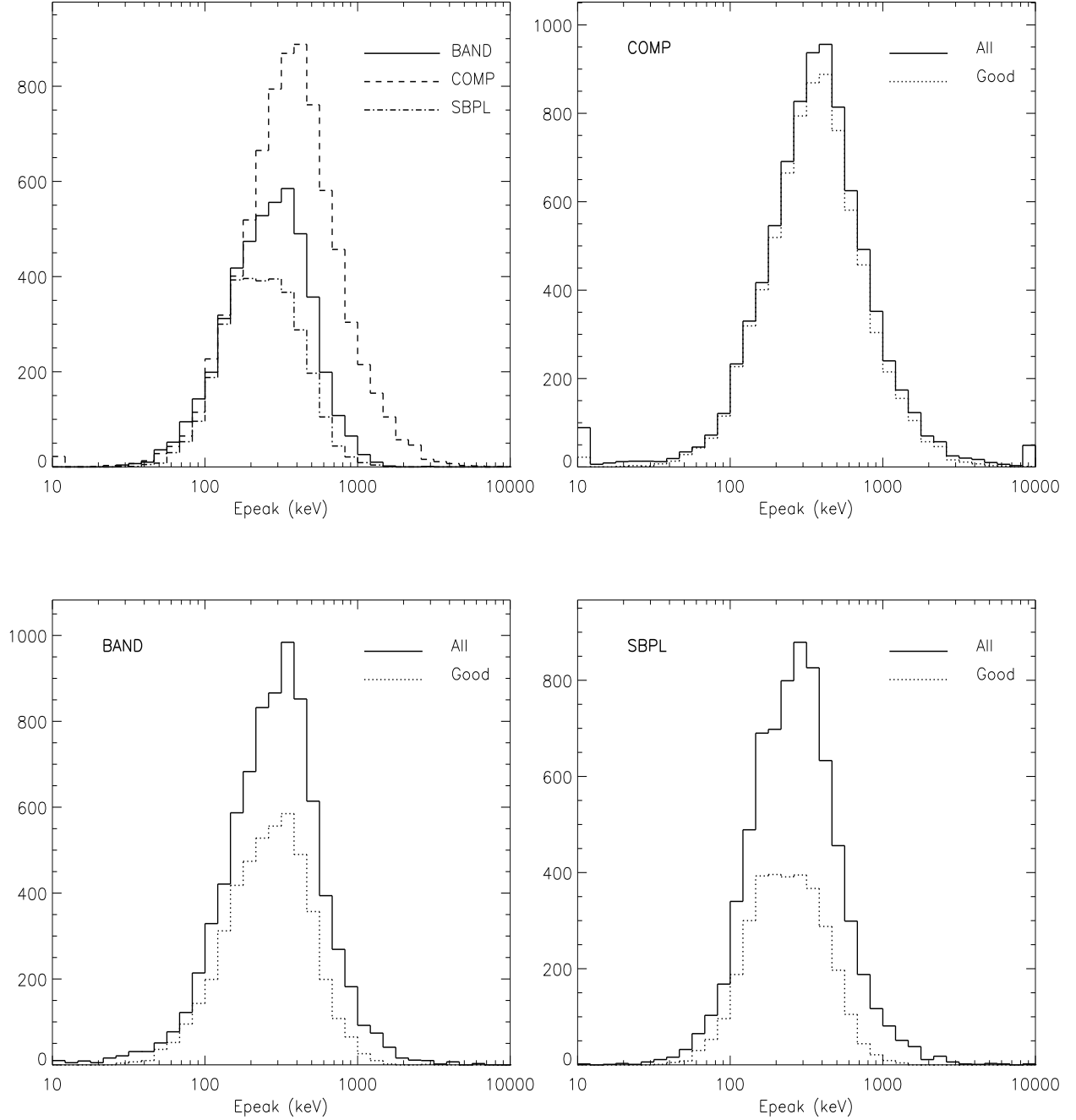


Fig. 16.— E_{peak} distribution of 8459 time-resolved spectra. [Top Left] *Good* parameters of all models. Numbers of parameters included are 7702 COMP, 4677 BAND, and 3291 SBPL. The other plots show all (solid line) and *good* (dotted line) parameters of COMP, BAND, and SBPL. The lowest (highest) bin includes values lower (higher) than the edge values.

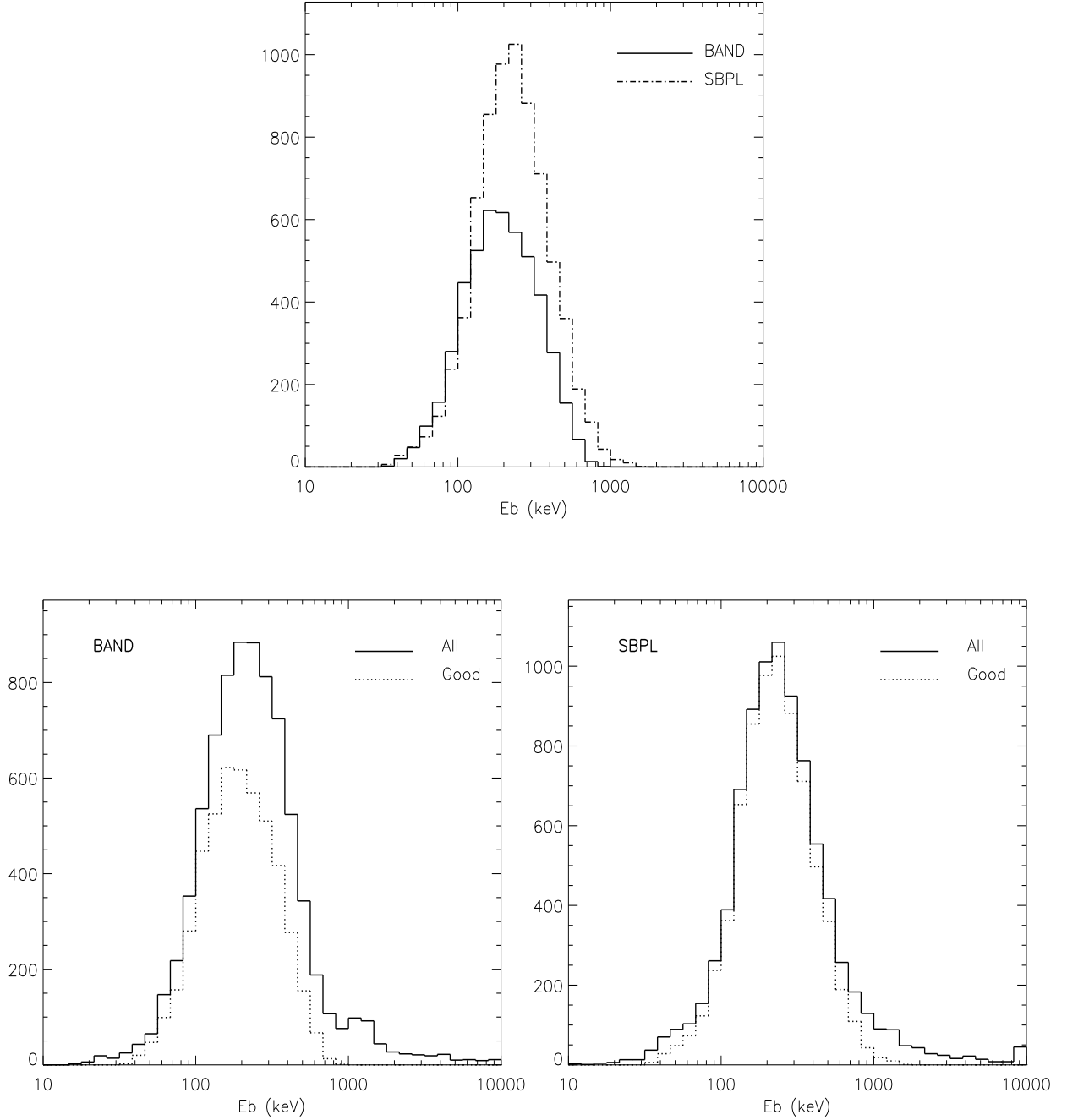


Fig. 17.— Break energy distribution of 8459 time-resolved spectra. [Top] *Good* parameters of all models. Numbers of parameters included are 4825 BAND and 7207 SBPL. The other plots show all (solid line) and *good* (dotted line) parameters of BAND and SBPL. The lowest (highest) bin includes values lower (higher) than the edge values.

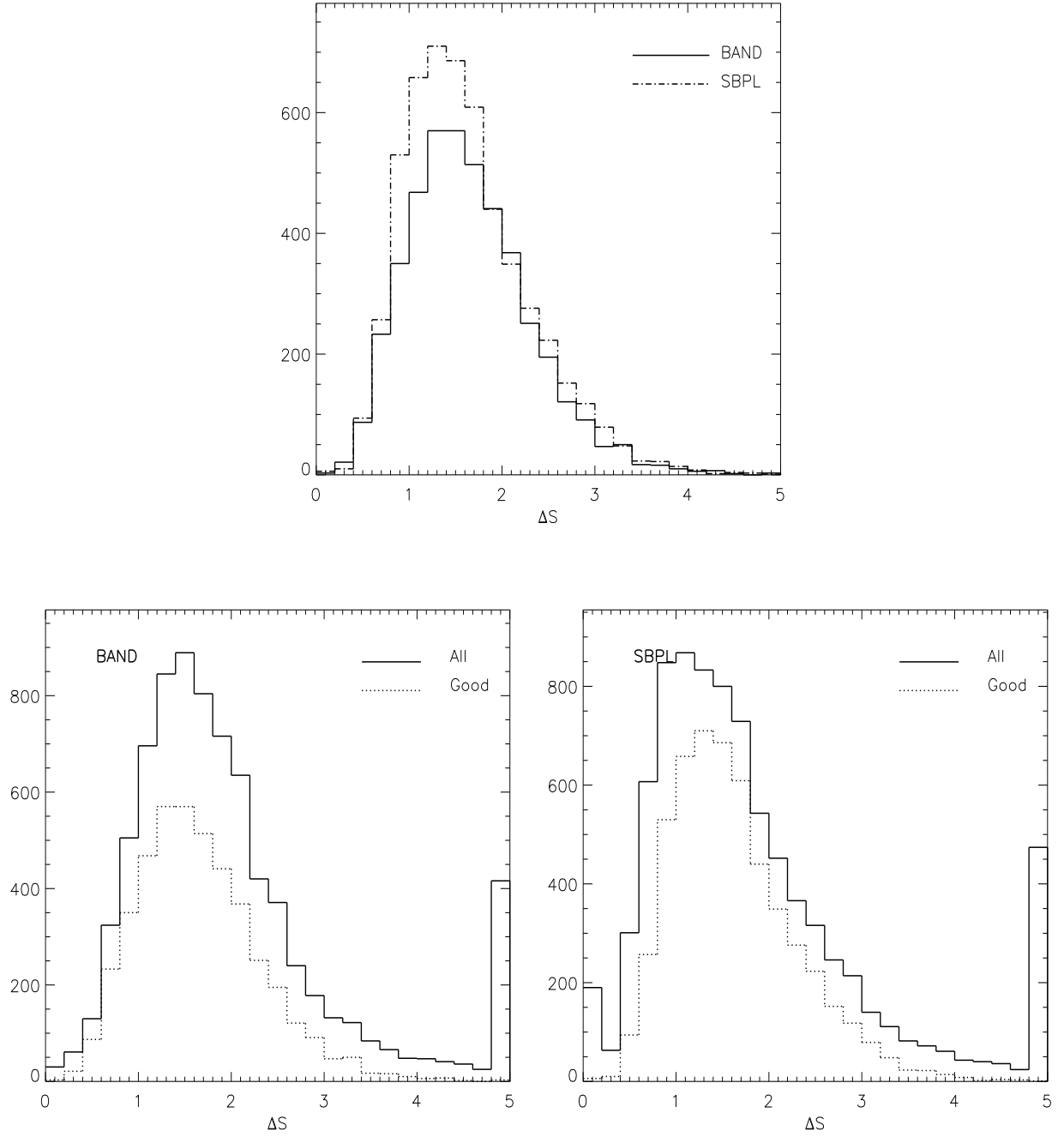


Fig. 18.— ΔS distribution of 8459 time-resolved spectra. ΔS is the difference between low-energy and high-energy indices. [Top] *Good* parameters of all models. Numbers of parameters included are 4441 BAND and 5322 SBPL. The other plots show all (solid line) and *good* (dotted line) parameters of BAND and SBPL. The lowest (highest) bin includes values lower (higher) than the edge values.

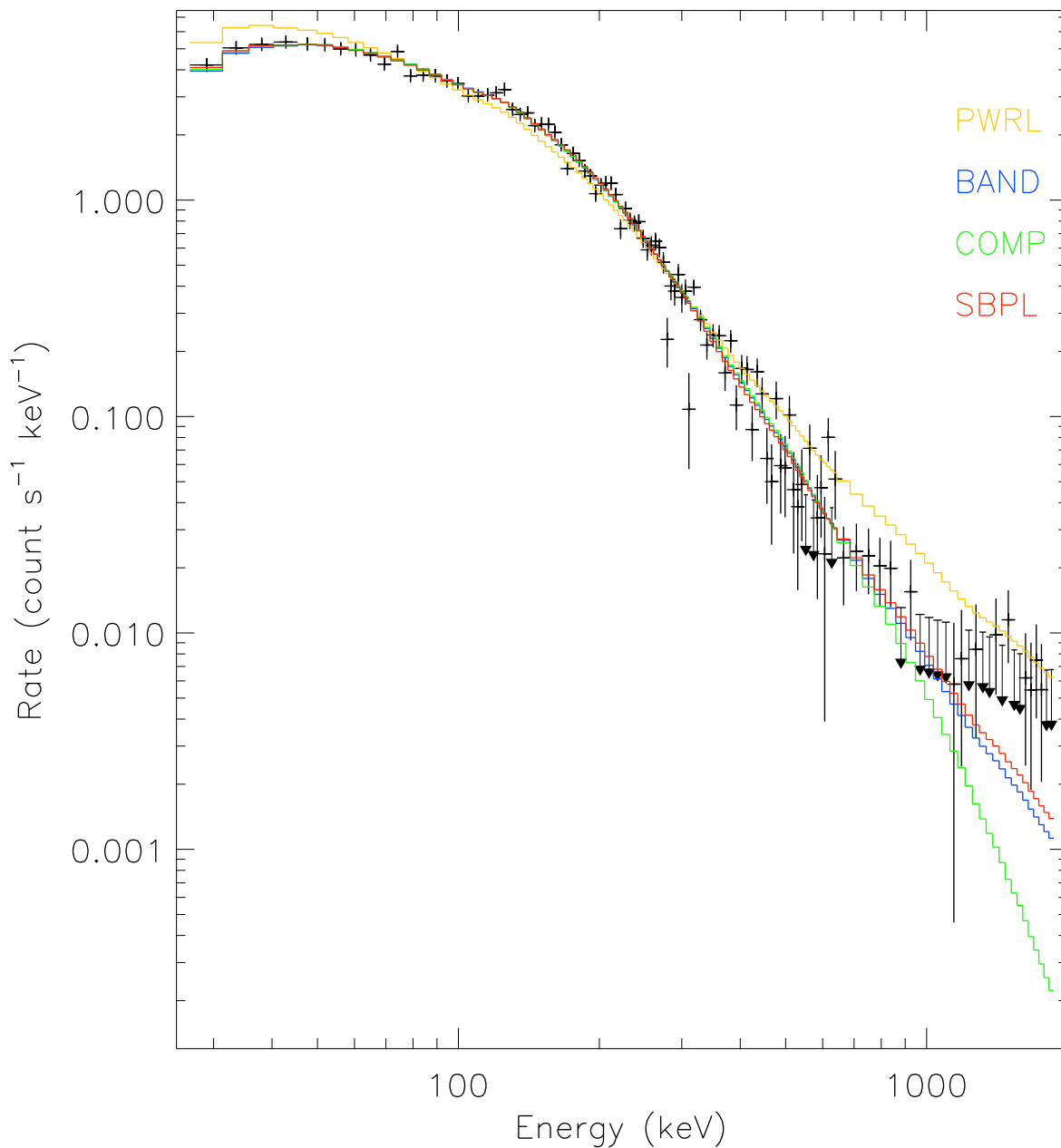


Fig. 19.— Count spectra of GRB 000429 (trigger number 8087). Data points are shown as crosses and the color lines are convolved model counts. COMP, BAND, and SBPL all fit statistically as good as each other. The BEST model determined by parameter constraints in this case is SBPL.

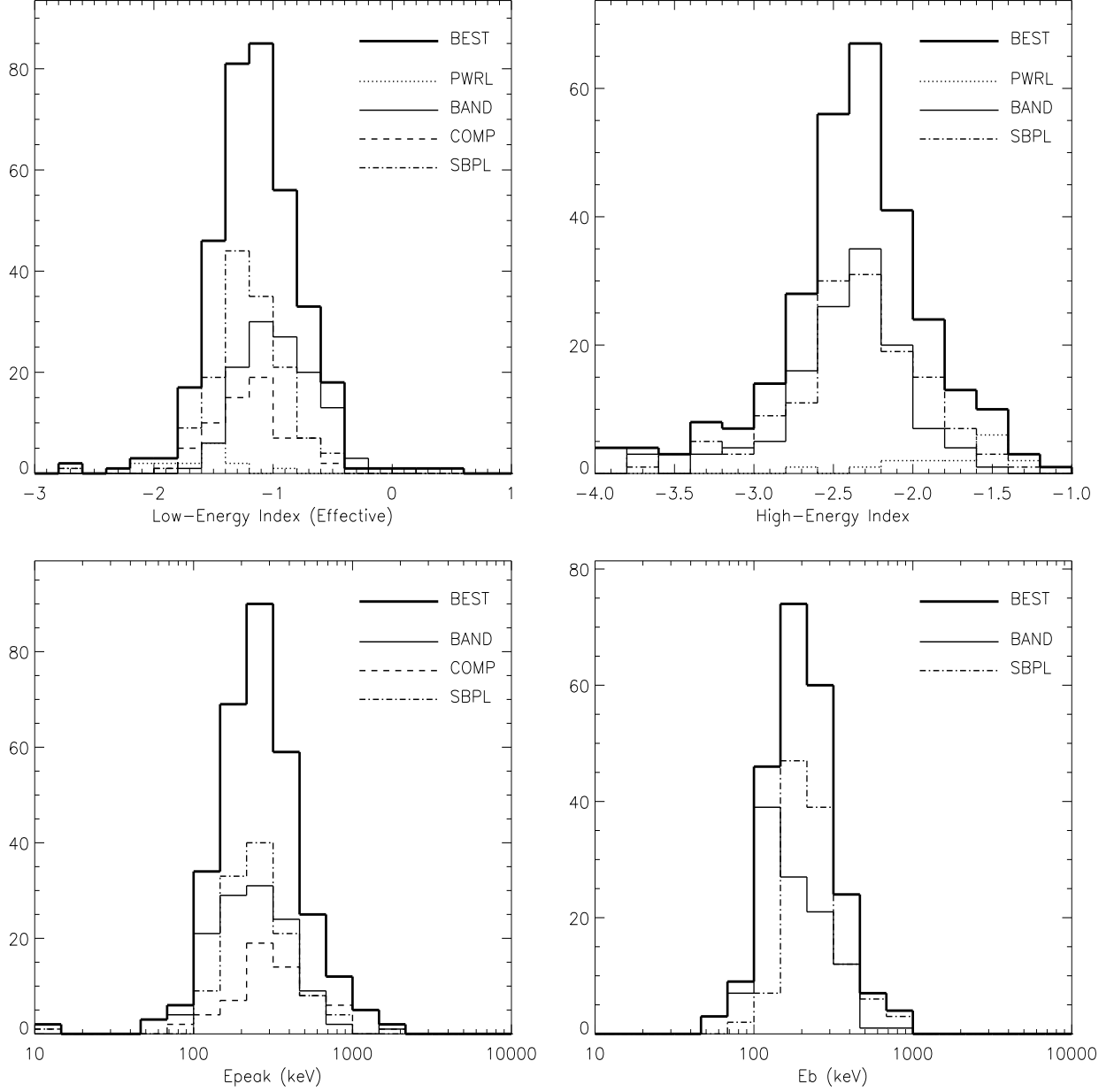


Fig. 20.— BEST model parameter distributions of the time-integrated spectra. The bold black lines show the total distributions, and the constituents are shown in various lines. The lowest (highest) bin includes values lower (higher) than the edge values.

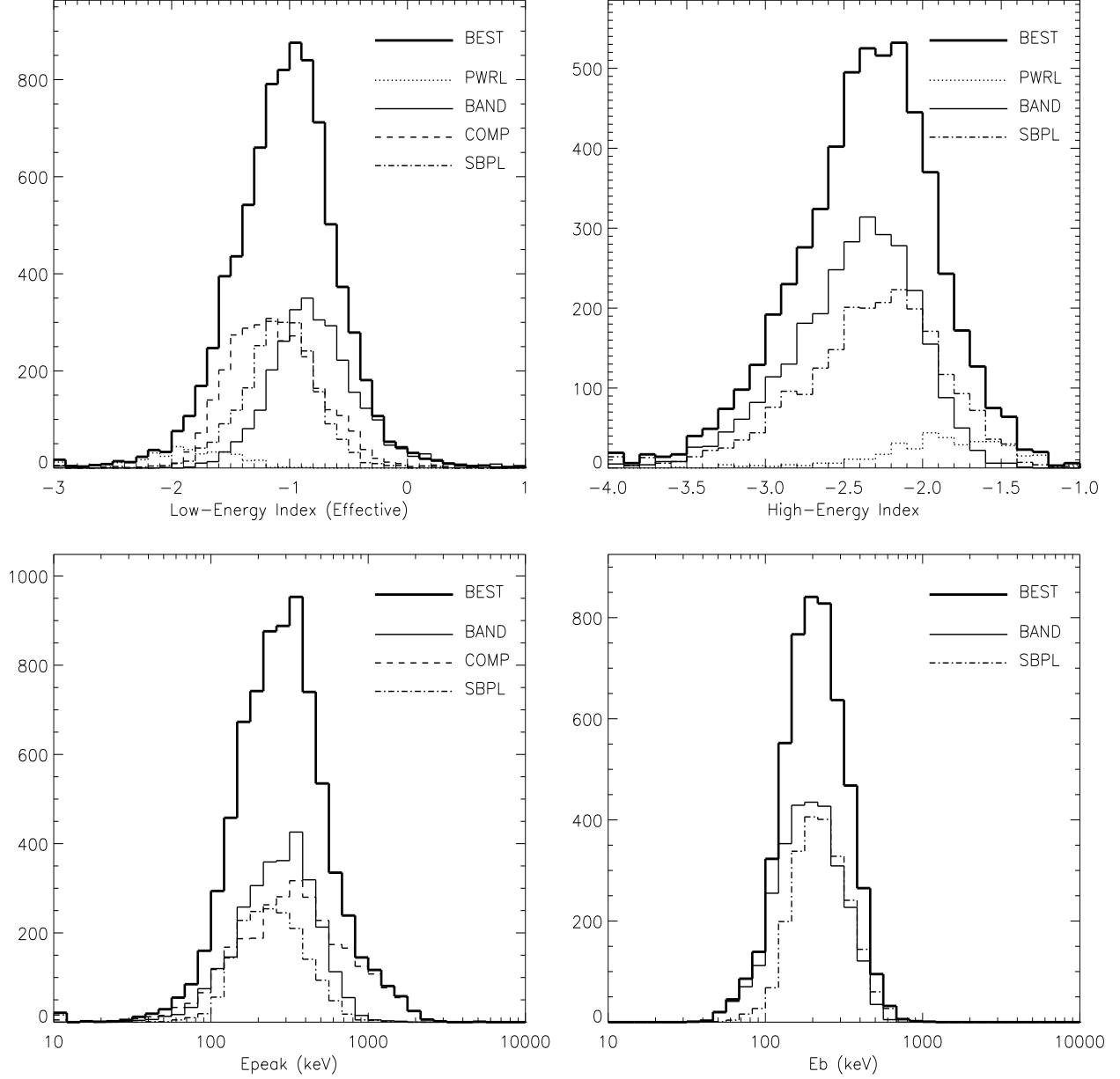


Fig. 21.— BEST model parameter distributions of the time-resolved spectra. The bold solid lines show the total distributions, and the constituents are shown in various lines. The lowest (highest) bin includes values lower (higher) than the edge values.

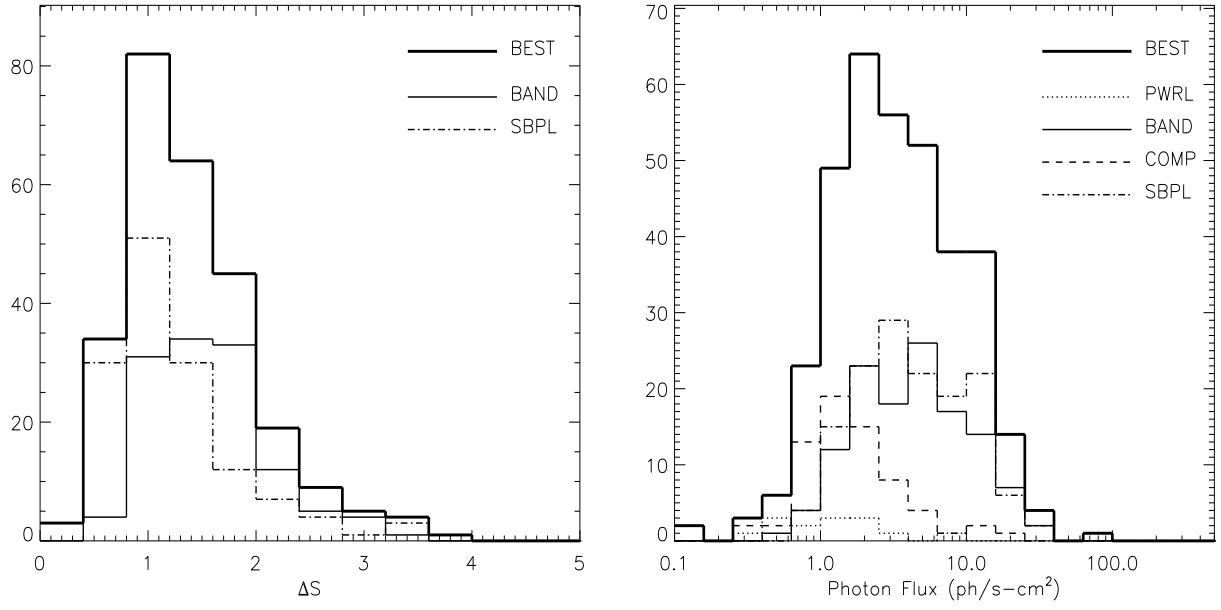


Fig. 22.— BEST model spectral index difference (ΔS) and average photon flux distributions of the time-integrated spectra. The bold black lines show the total distributions, and the constituents are shown in various lines. The lowest (highest) bin includes values lower (higher) than the edge values.

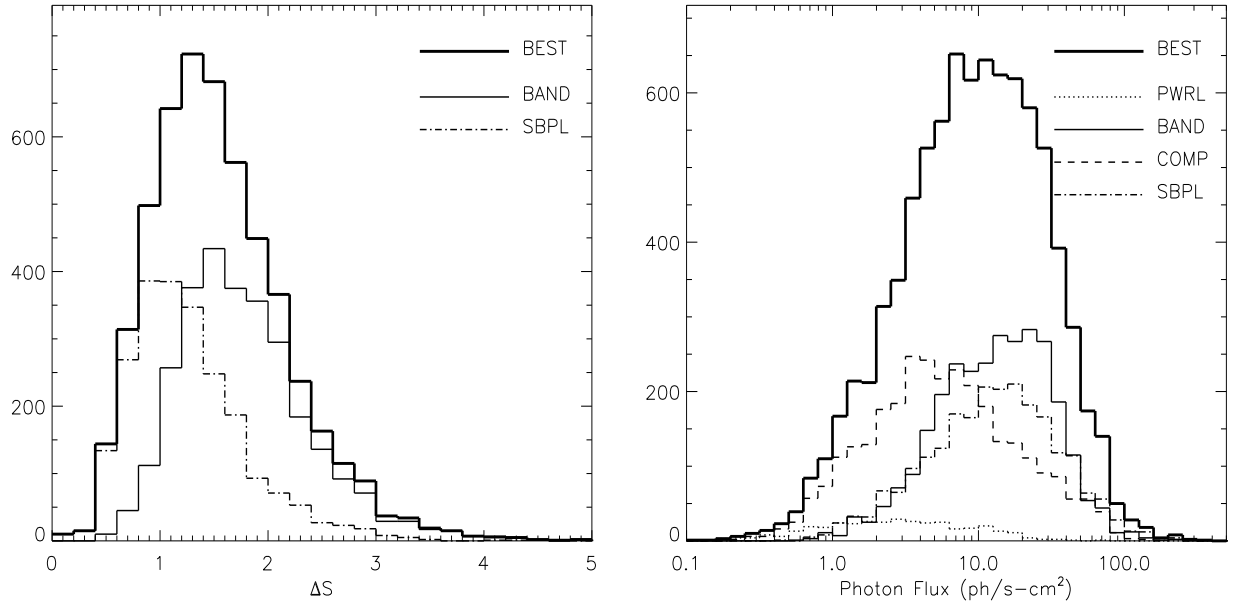


Fig. 23.— BEST model spectral index difference (ΔS) and average photon flux distributions of the time-resolved spectra. The bold solid lines show the total distributions, and the constituents are shown in various lines. The lowest (highest) bin includes values lower (higher) than the edge values.

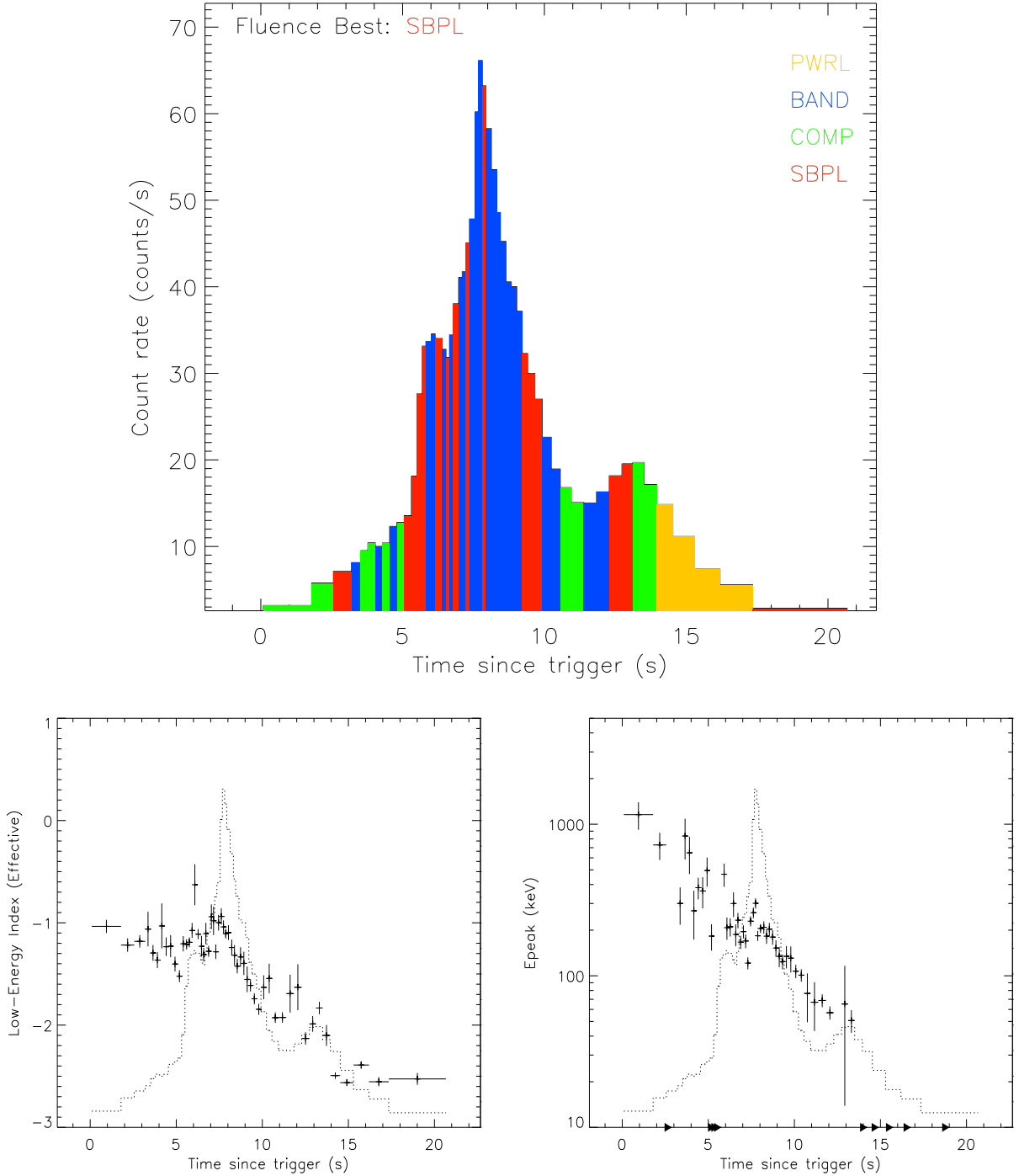


Fig. 24.— [Top] BEST model history of GRB 950403 (BATSE trigger number 3491). The BEST model of the time-integrated spectrum for this burst is SBPL. [Bottom] Evolutions of the low-energy index (effective) and E_{peak} for the same event. The arrowheads in E_{peak} plot indicate where the E_{peak} values cannot be determined.

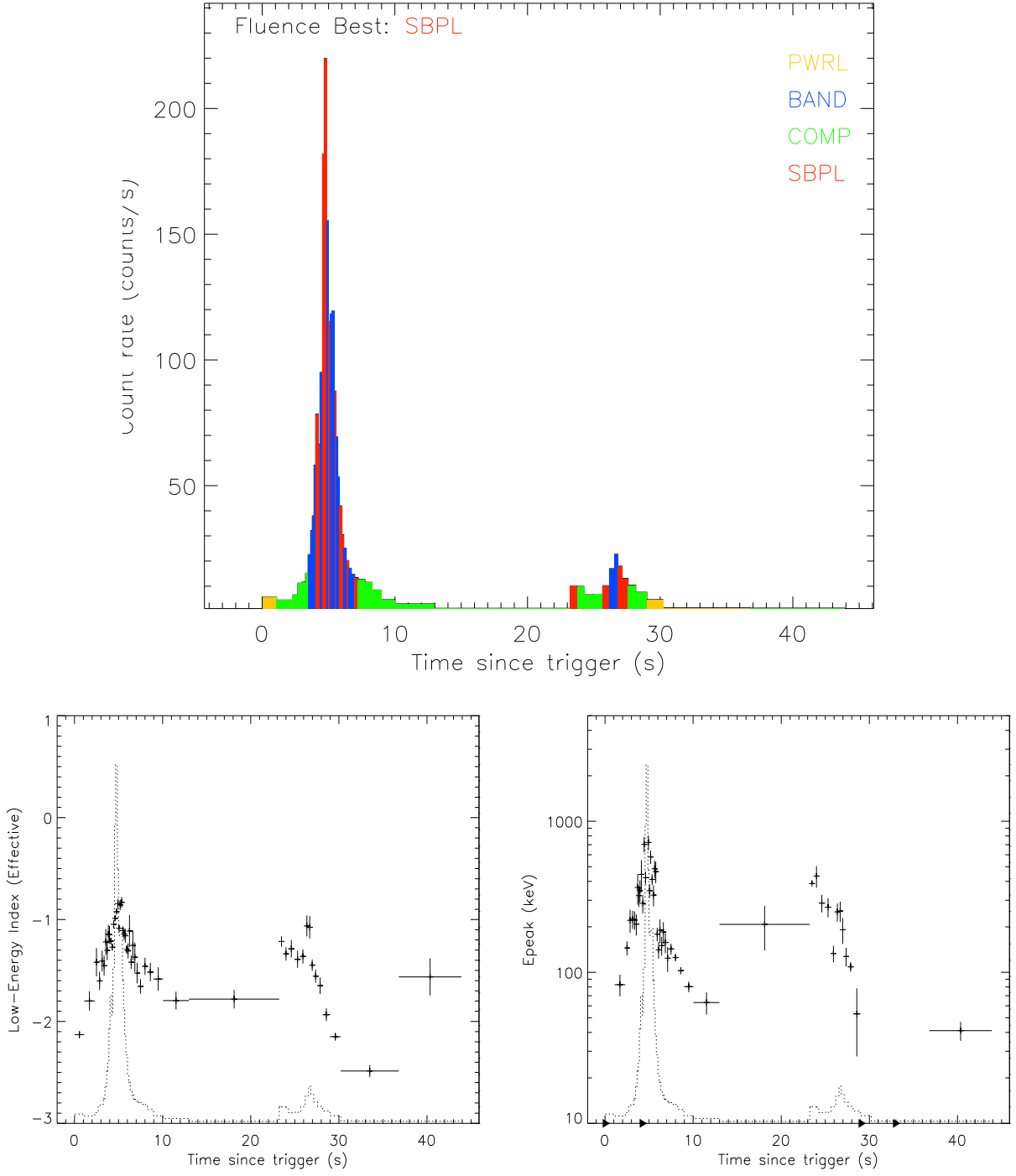


Fig. 25.— [Top] BEST model history of GRB 950403 (BATSE trigger number 3492). The BEST model of the time-integrated spectrum for this burst is SBPL. [Bottom] Evolutions of the low-energy index (effective) and E_{peak} for the same event. The arrowheads in E_{peak} plot indicate where the E_{peak} values cannot be determined.

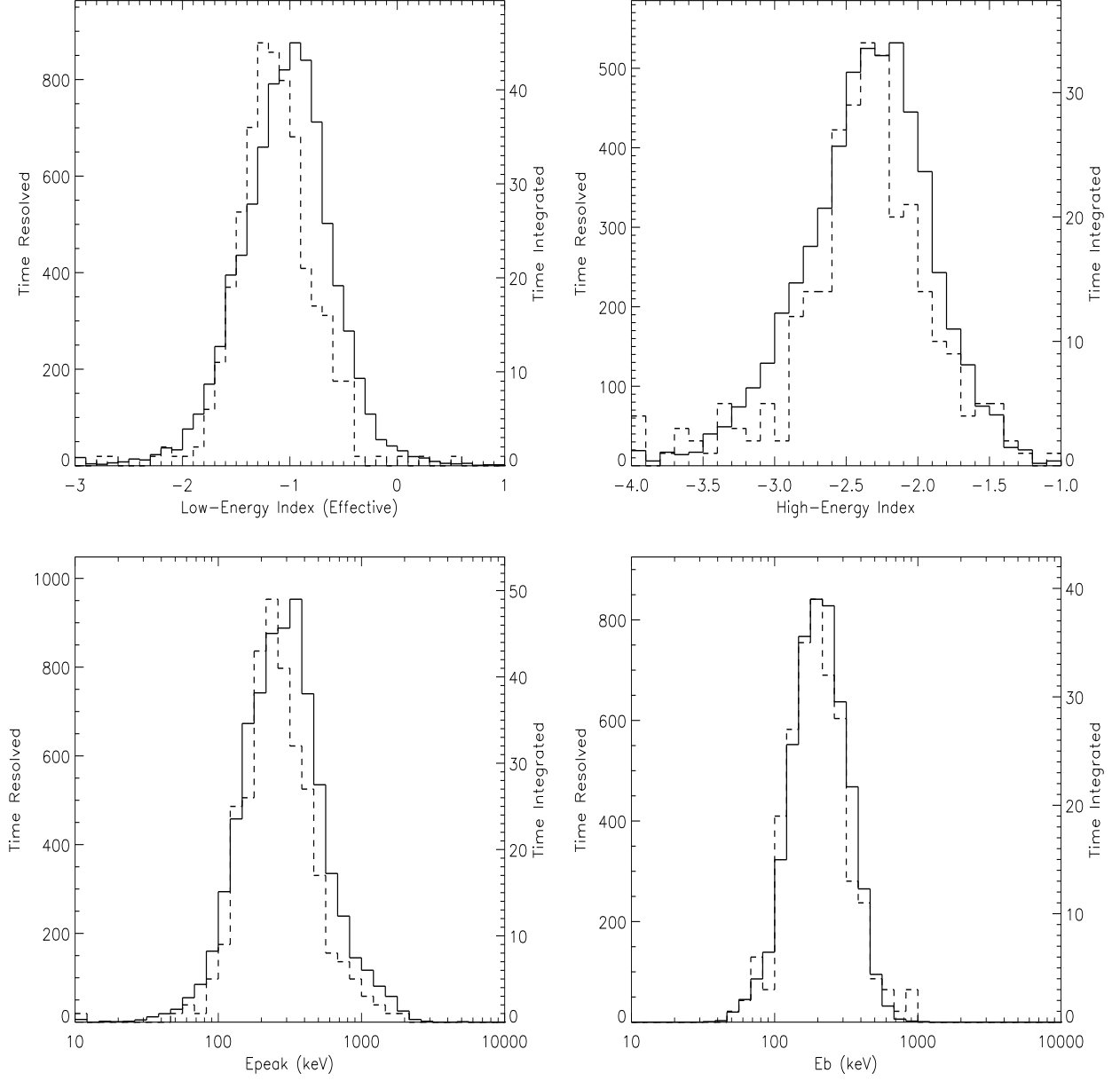


Fig. 26.— Comparisons of the BEST model parameter distributions of time-integrated (dashed; right axis) and time-resolved spectra (solid; left axis). The lowest (highest) bin includes values lower (higher) than the edge values.

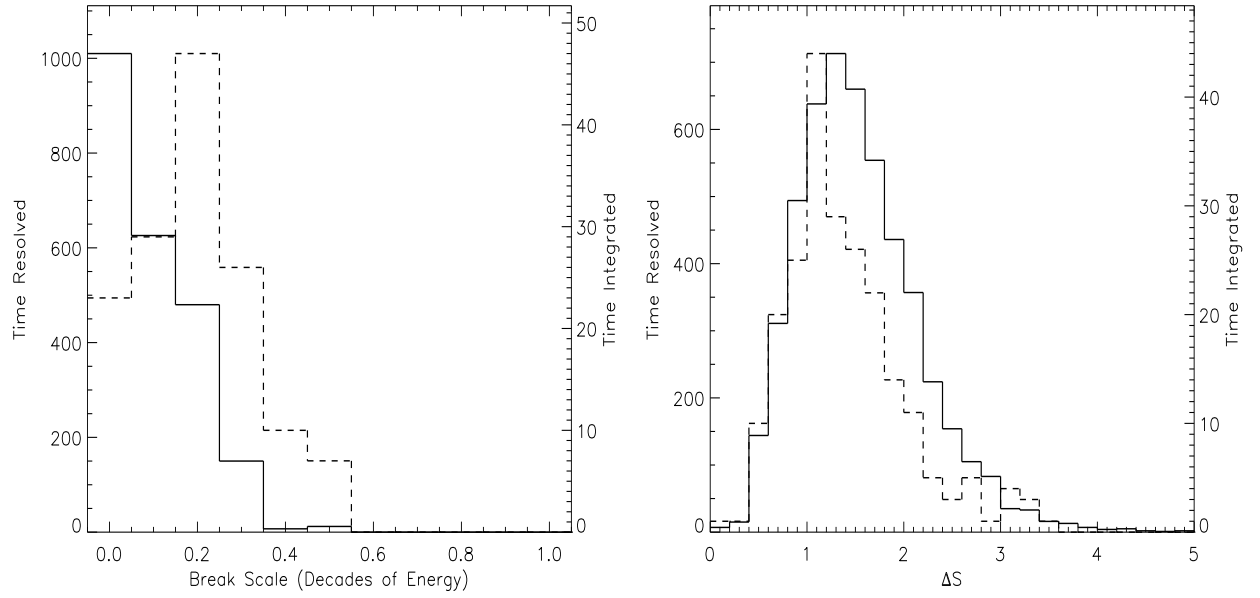


Fig. 27.— Comparisons of the BEST model break scale (Λ) and ΔS distributions of time-integrated (dashed; right axis) and time-resolved spectra (solid; left axis). The break scale values are for spectra fitted with SBPL only, while ΔS values are for those fitted with BAND and SBPL.

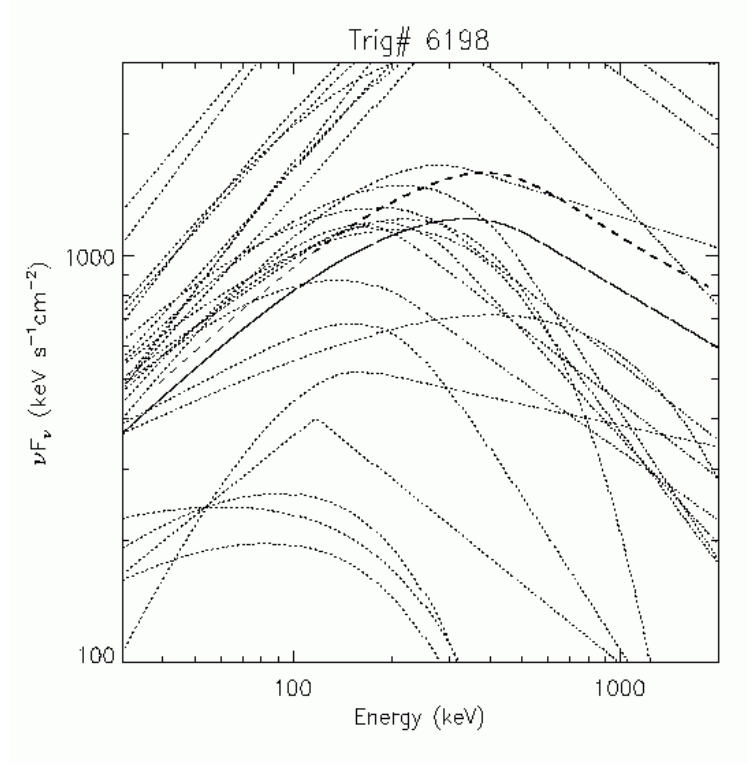


Fig. 28.— Spectra of GRB 970420 (BATSE trigger number 6198). Time-integrated BEST model is plotted as a solid curve. The dashed curve shows the $\bar{\mathcal{F}}_{fluence}$ spectrum, which is different from the BEST model. The time-resolved BEST models are shown in dotted curves.

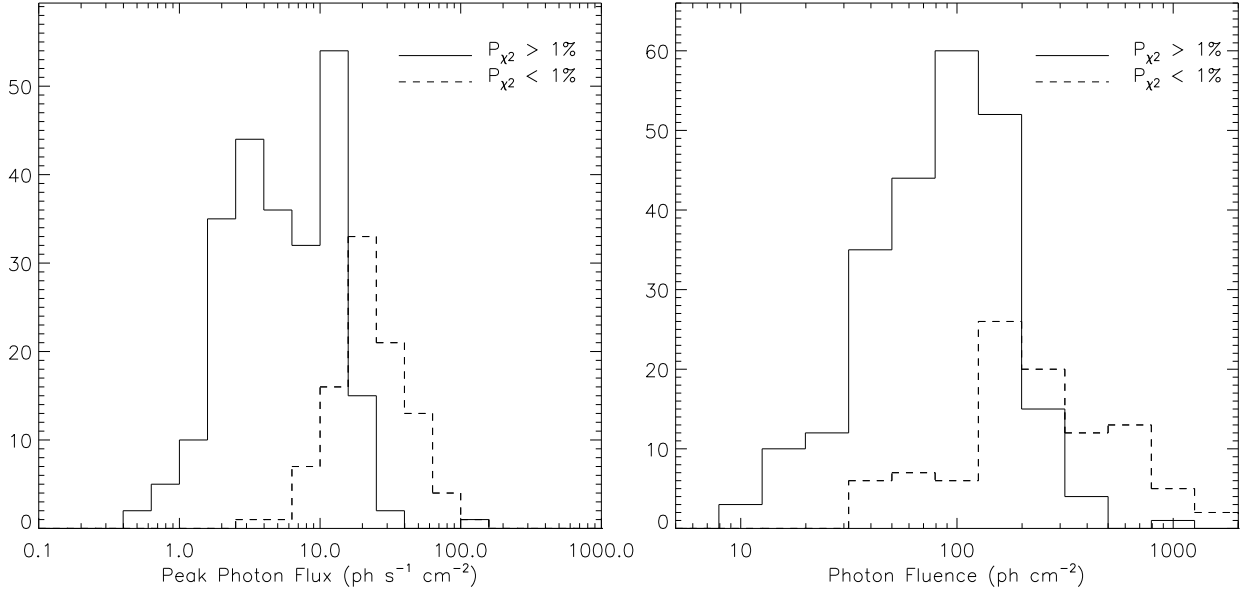


Fig. 29.— Distribution of peak photon flux (256 ms, 30 – 500 keV; *left*) and total photon fluence values (25 – 2000 keV; *right*) of 333 bursts. The bursts with $P_{\chi^2_f} > 1\%$ (solid line) have lower flux and fluence than those with $P_{\chi^2_f} < 1\%$ (dashed line).

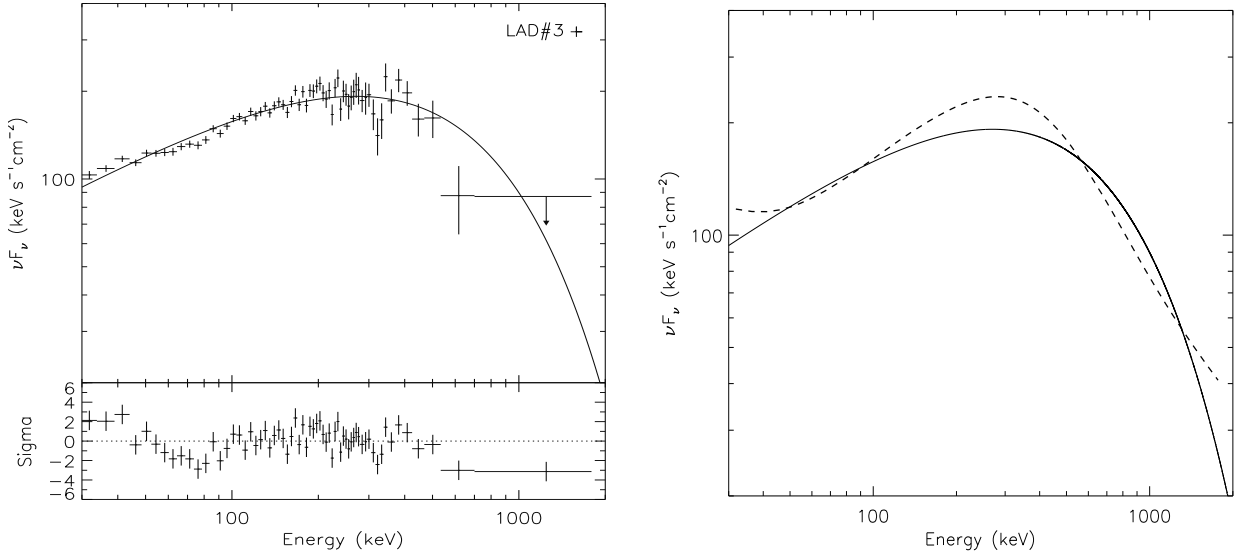


Fig. 30.— [*Left*] The actual deconvolved time-integrated photon data (crosses) and the best-fit model of GRB 980306. [*Right*] The constructed photon flux $\bar{\mathcal{F}}$ of GRB 980306 (dashed curve). In both plots, the time-integrated BEST model (COMP) is plotted as solid curves.

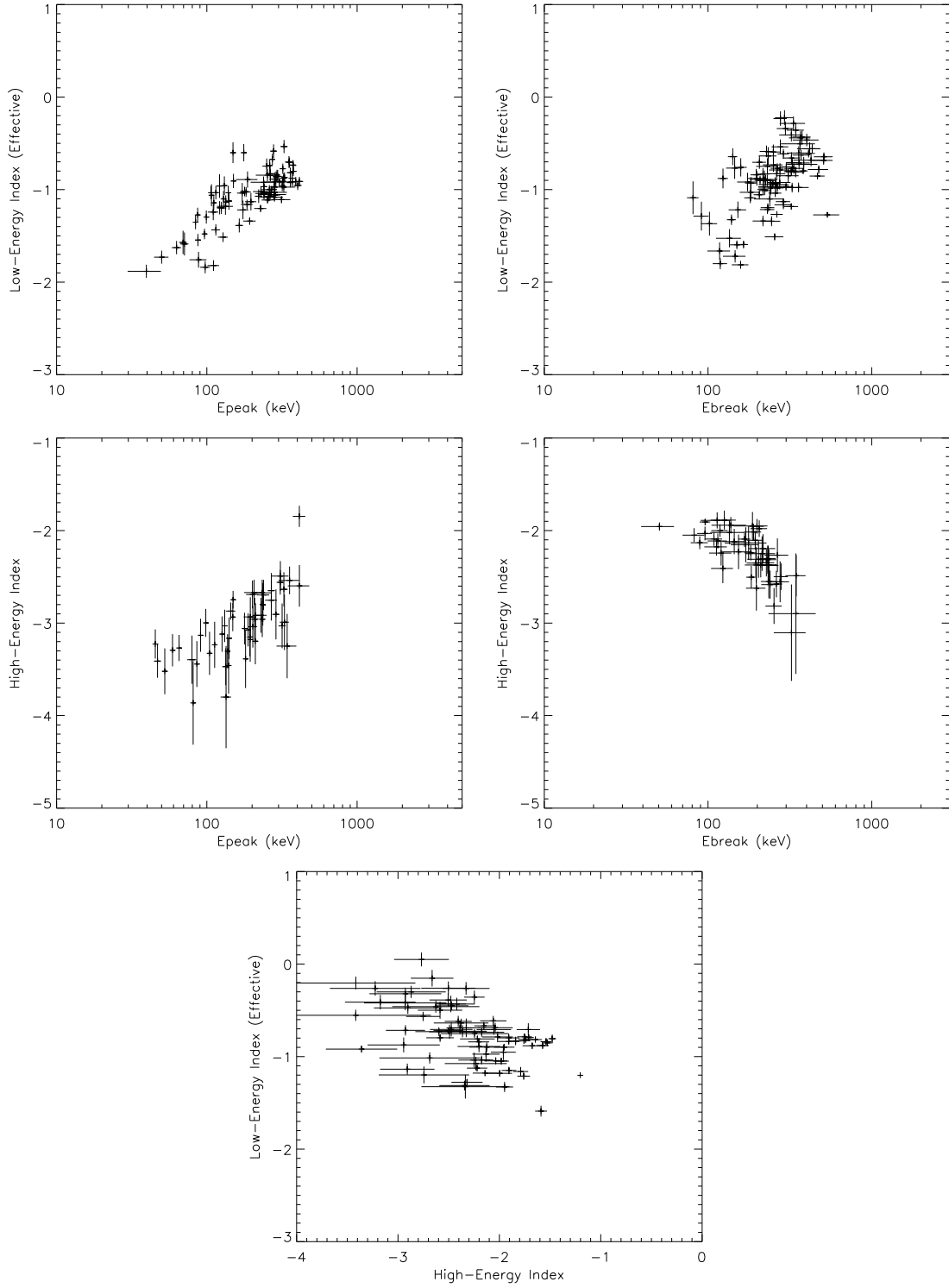


Fig. 31.— Example scatter plots of spectral parameter pairs showing correlations. [*Top*] $E_{\text{peak}} - \alpha$ of GRB 941020 (trigger number 3253; *left*) and $E_{\text{b}} - \alpha$ of GRB 931204 (2676; *right*). Both show strong positive correlations. [*Middle*] $E_{\text{peak}} - \beta$ of GRB 911118 (trigger number 1085; *left*) and $E_{\text{b}} - \beta$ of GRB 980203 (6587; *right*). [*Bottom*] $\alpha - \beta$ of GRB 920824 (trigger number 1872). Negative correlations are evident in $E_{\text{b}} - \beta$ and $\alpha - \beta$.

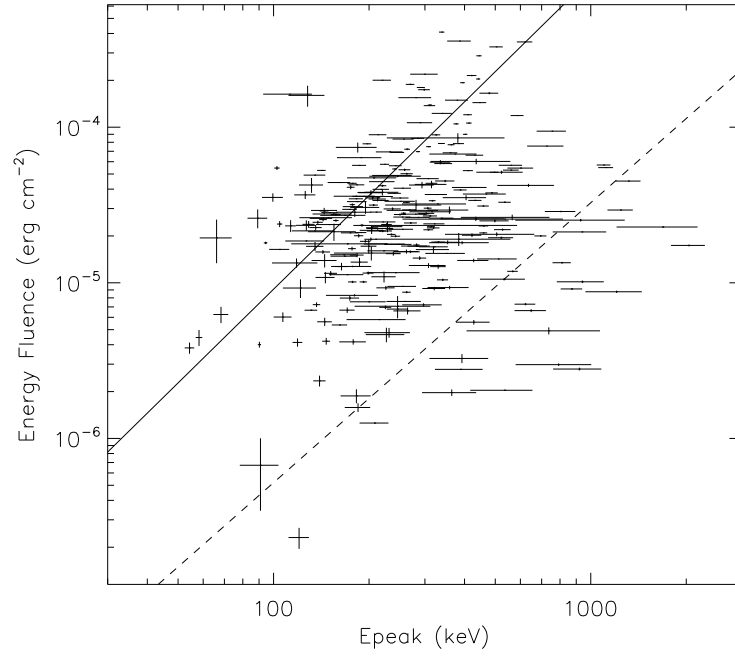


Fig. 32.— Energy fluence in 25 – 2000 keV vs. E_{peak} plot. The Amati relation limit is shown as a solid line and Ghirlanda 3σ limit is shown as a dashed line. Bursts below these lines are inconsistent with the relation. The uncertainties are 1σ .

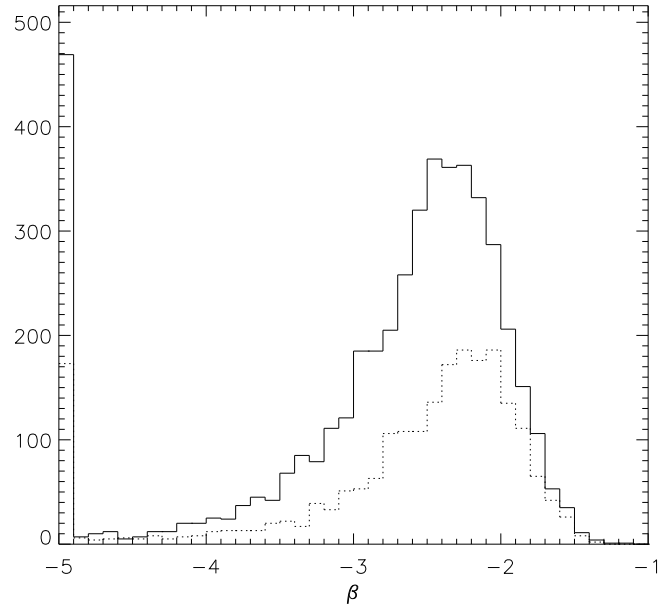


Fig. 33.— The distributions of the BAND fit β values of time-resolved spectra within varying- β (solid line) and constant- β (dotted line) GRBs. The lowest bin includes values lower than -5 .

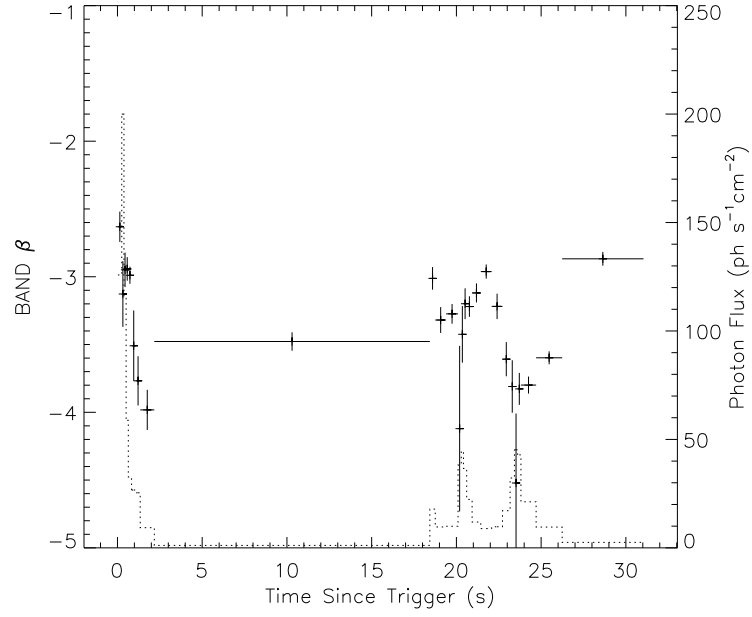


Fig. 34.— Evolution of the BAND fit β values of an example varying- β GRB (GRB 970201, BATSE trigger number 5989). The photon flux history is overplotted with dotted lines (right axis).

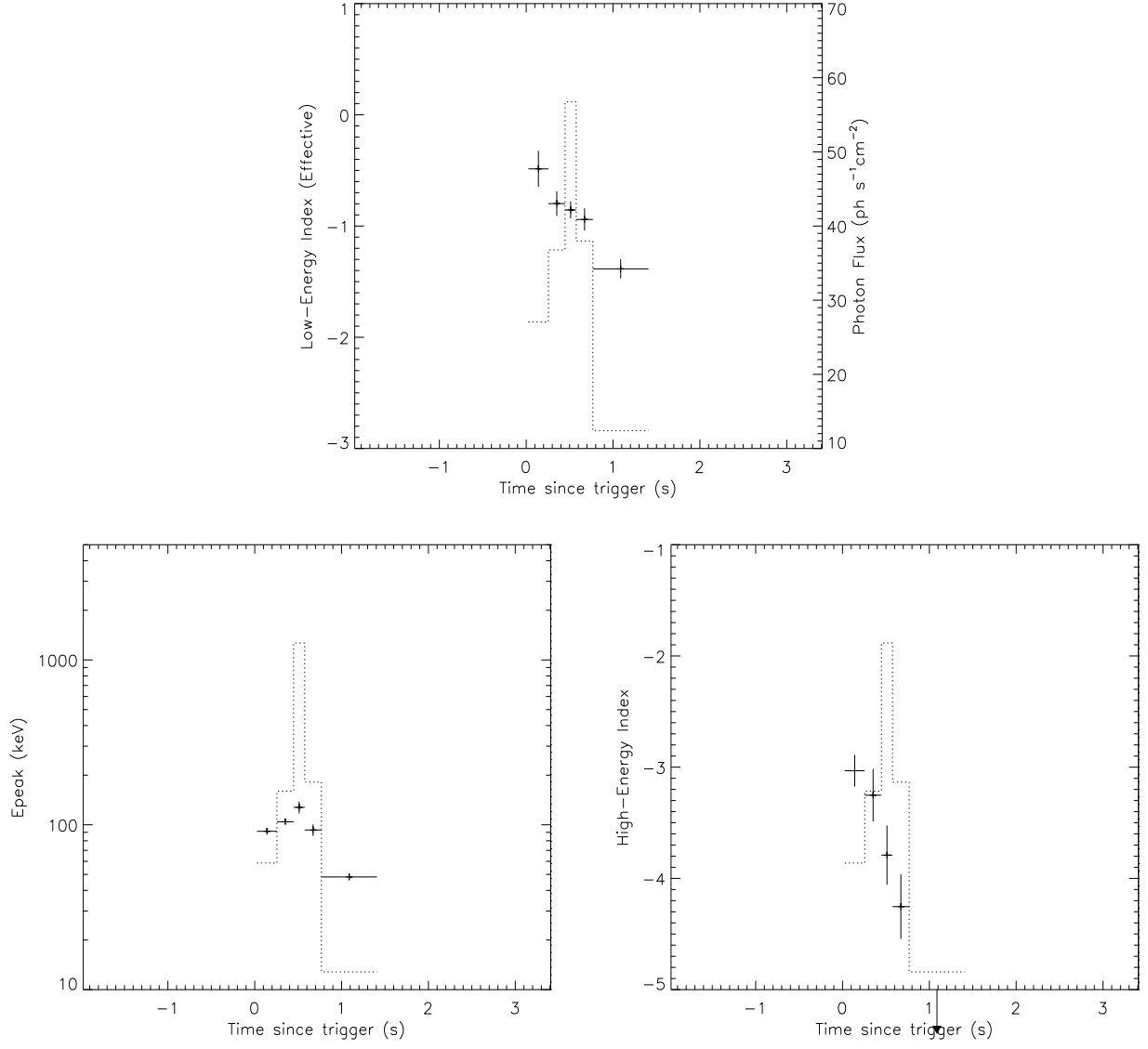


Fig. 35.— Parameter evolution of a short event, GRB 000326 (trigger number 8053). The photon flux histories are over-plotted with dotted lines (top panel, right axis). E_{peak} tracks the photon flux while the indices evolve from hard to soft.

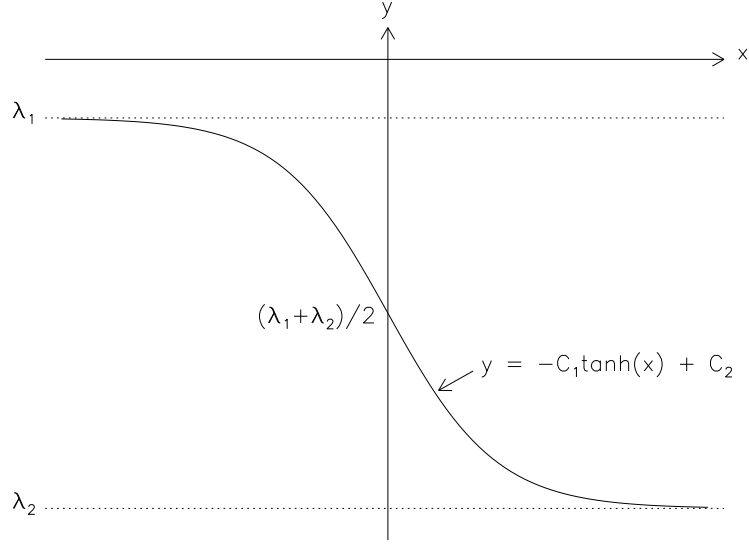


Fig. 36.— Plot of Equation A1. The index changes from λ_1 to λ_2 smoothly.

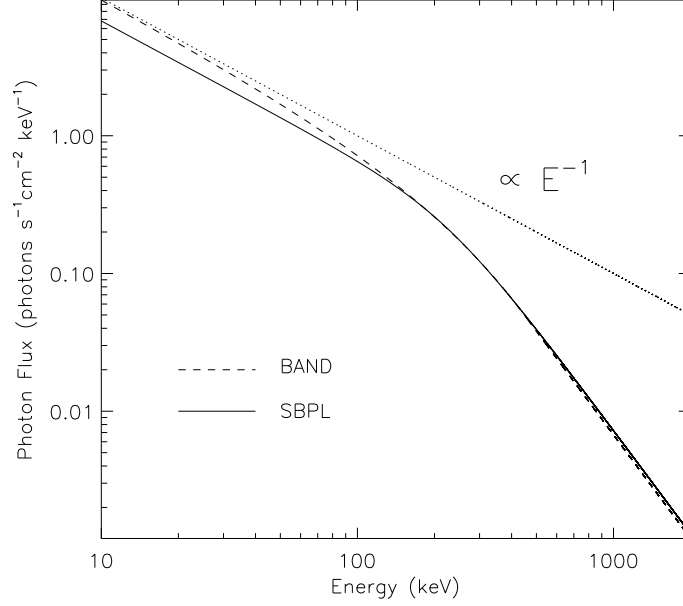


Fig. 37.— The BAND model (dashed curve) and the SBPL model (solid curve) with the same low-energy index values of $\alpha = \lambda_1 = -1$. The other parameters are also kept the same ($E_{\text{peak}} = 300$ keV and $\beta = \lambda_2 = -2.5$). A dotted line is a power law with index of -1 . The difference in the low-energy behavior is evident.

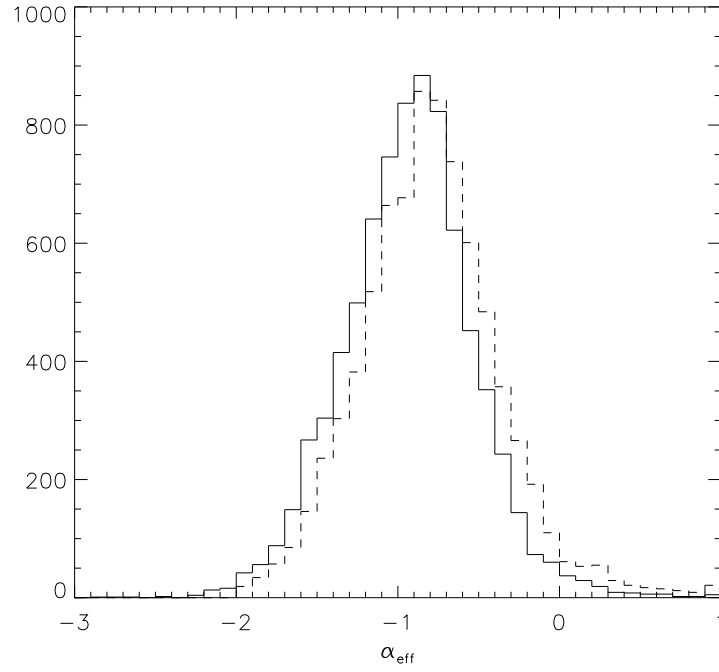


Fig. 38.— The comparison of the effective α distribution (solid line) and the fitted α distribution (dashed line) of the BAND model fits to the 7861 time-resolved spectra.